

Ion flow and fusion reactivity characterization of a spherically convergent ion focus

Thorson, Timothy Arthur

ProQuest Dissertations and Theses; 1996; ProQuest Dissertations & Theses Full Text

pg. n/a

INFORMATION TO USERS

The negative microfilm copy of this dissertation was prepared and inspected by the school granting the degree. We are using this film without further inspection or change. If there are any questions about the content, please write directly to the school. The quality of this reproduction is heavily dependent upon the quality of the original material.

The following explanation of techniques is provided to help clarify notations which may appear on this reproduction.

1. Manuscripts may not always be complete. When it is not possible to obtain missing pages, a note appears to indicate this.
2. When copyrighted materials are removed from the manuscript, a note appears to indicate this.
3. Oversize materials (maps, drawings, and charts) are photographed by sectioning the original, beginning at the upper left hand corner and continuing from left to right in equal sections with small overlaps.
4. Most photographs reproduce acceptably on positive microfilm or microfiche but lack clarity on xerographic copies made from the microfilm. For any illustrations that cannot be reproduced satisfactorily by xerography, photographic prints can be purchased at additional cost and tipped into your xerographic copy. Requests can be made to the Dissertations Customer Services Department.



University Microfilms International
A Bell & Howell Information Company
300 N. Zeeb Road, Ann Arbor, Michigan 48106

UMI Number: 9707921

UMI Microform 9707921
Copyright 1997, by UMI Company. All rights reserved.

**This microform edition is protected against unauthorized
copying under Title 17, United States Code.**

UMI
300 North Zeeb Road
Ann Arbor, MI 48103

A dissertation entitled

Ion Flow and Fusion Reactivity Characterization of a
Spherically Convergent Ion Focus

submitted to the Graduate School of the
University of Wisconsin-Madison
in partial fulfillment of the requirements for the
degree of Doctor of Philosophy

by

Timothy A. Thorson

Degree to be awarded: December 1996 May 19 August 19

Approved by Dissertation Readers:

Raymond J. Tisch
Major Professor

November 25, 1996
Date of Examination

J.J. Kulcinski

Stan C.P.

Virginia Shadley,
Dean, Graduate School

**ION FLOW AND FUSION REACTIVITY
CHARACTERIZATION OF A SPHERICALLY
CONVERGENT ION FOCUS**

by

Timothy A. Thorson

A dissertation submitted in partial fulfillment

of the requirements for the degree of

Doctor of Philosophy
(Nuclear Engineering and Engineering Physics)

at the
UNIVERSITY OF WISCONSIN - MADISON
1996

Acknowledgments

Here I would like to thank the many people who have encouraged and supported me, and those who have made this work and accomplishment possible. I owe a great deal to my thesis advisor, Prof. Ray Fonck, whose tireless efforts continue to impress and inspire me. I have learned many things along the way, from research techniques to teaching approaches to specifics about physics and fusion engineering. I appreciate him (and Prof. Callen) taking a chance on me five years ago and again for enlisting my assistance in the Pegasus Tokamak Project. It has been very enjoyable working with him, and I look forward to my future work on Pegasus.

I also appreciate the efforts of Prof. Kulcinski and Dr. Santarius who helped bring the SCIF-related research to Wisconsin and for their work with the Electric Power Research Institute (EPRI).

I would also like to thank my thesis committee for taking time from their busy schedules to review this research. Many others have also provided much-needed technical assistance (I can be all thumbs at times) and useful discussions throughout this work. Prof. Noah Hershkowitz, Dr. Roger Durst, Bob Ashley, Robert Buckles, Brad Foucher, Paul Nonn, Aaron Sontag, Lou Wainwright, and Greg Winz have all provided either their technical and/or professional insight to this project.

While graduate school was at times difficult, my “brothers-in-arms” often helped along the way to make it very enjoyable as well. I wish many thanks to Greg Garstka, Steve Wukitch, and Ji-Soo Kim for suffering through classes and qualifiers with me and to my main office mates, Hal Evensen, Tom Gianakon, and George McKee for their help since essentially Day 1. Also, I owe thanks to Jim DeKock, Ben Lewicki, Kevin Tritz, and the rest

of the Pegasus/MEDUSA/Phaedrus clan, with special mention to Pat Caliva and Pam Wagner for their wonderful company and assistance.

Last, but certainly not least, I owe a huge debt of gratitude to my parents, family, and the Lord whose encouragement, support, and love have helped me through the difficult stages throughout my education and life. My wife, Gail, has been especially understanding and supportive as I struggled through the tribulations associated with graduate work. I also cannot forget our cats, Muffy and Perry, who have helped remind me what is important in life and to come back down to earth from time-to-time.

Thanks again to you all...

Timothy A. Thorson

November 1996

This work was supported in part by the University of Wisconsin College of Engineering and by EPRI Research Agreement 6424-51010.

TABLE OF CONTENTS

Abstract	v
Chapter 1: Introduction	1
1.1: Motivation of SCIF research	3
1.2: Ion flow characterization	4
1.3: Fusion source measurements	6
1.4: Summary of objectives	8
1.5: References	10
Chapter 2: Zero-order model of the ion flow	12
2.1: Ideal ion convergence limit	16
2.2: Radial density distribution models	17
2.3: Electric potential profile	23
2.4: Total fusion production rate estimates	25
2.5: References	33
Chapter 3: Past theoretical and experimental studies	34
3.1: Fusion reaction rate experiments	35
3.2: Multiple-well hypothesis	37
3.3: Charge-exchange model	44
3.4: Conclusions and WISCIF experimental relevance	45
3.5: References	47
Chapter 4: The WISCIF apparatus	49
4.1: Vacuum system and neutral gas control	51
4.2: Gridded electrode design and cathode mount	52
4.3: Edge plasma source	54
4.4: Power supply systems	56
4.5: Diagnostics	57
4.6: References	73
Chapter 5: Ion flow characterization	74
5.1: General discharge characteristics	75
5.2: Potential distribution measurements	77
5.3: Core flow convergence measurements	83
5.4: Core density measurements	89
5.5: Discussion and conclusions	93
5.6: References	102
Chapter 6: Fusion reactivity characterization	103
6.1: Reactivity measurements	104
6.2: Analysis and discussion	114
6.3: References	124

Chapter 7: Summary	125
7.1: Ion flow characterization	125
7.2: Fusion production rate measurements	126
7.3: Comments and future directions	127
7.4: Conclusions	128
7.5: References	130
Appendix 1: Core reaction rate calculations for beam-beam interactions	131
Appendix 2: Double probe theory for ion-dominated flow	134

Abstract

The Spherically Convergent Ion Focus (SCIF) is an electrostatic confinement scheme where ions of fusion-relevant energies are trapped in a spherically symmetric potential well. These devices have been promoted for near-term applications and as a possible alternative concept for fusion power production. While higher-than-expected neutron rates have been observed, past experiments and theoretical models have been conflicting and inconclusive.

The Wisconsin SCIF experiments focused on directly measuring critical parameters that influence the resulting system reactivity. Unique measurements of the basic plasma-flow characteristics were obtained using high-voltage (≤ 5 kV) emissive and double probes. At low neutral gas pressures (≤ 50 mPa), the radial plasma potential distribution agrees with a collisionless, recirculating, space-charge-limited current model. Flow convergence increases with voltage and neutral pressure and decreases with cathode grid wire spacing and current. Core radii within 4-5 times the ideal geometric limit are measured, and the observed core sizes are consistent with predictions from multi-pass orbit calculations which include asymmetries in the accelerating potential well. A virtual anode is observed in the converged-core region, and measurements of the core ion density ($n_{ic} \sim 10^{15}$ m⁻³) agree with current conservation estimates.

Experiments designed to determine the source of fusion reactivity were conducted at application-relevant energies and densities. Results from neutral pressure scans (50 – 1000

mPa D₂) show that neutral collisions play a strong role in determining the system reactivity, while proton collimation measurements indicate that most of the reactivity originates well outside the central core region. A classical flow model that includes the effects of charge-exchange on the fusion reactivity (due to the resulting fast-neutral population) is consistent with the experimentally observed dependencies and magnitude of the D-D neutron production rate.

Therefore, the resulting core ion density and fusion reaction rate behave as predicted from a simple, classical flow model. No evidence of (or need for) anomalous ion trapping or multiple potential well structures in the core region, as suggested by some theoretical models of these systems, was found.

Chapter 1: Introduction

The Spherically Convergent Ion Focus (SCIF) is an alternative plasma confinement scheme in which ions are electrostatically confined, accelerated, and concentrated at fusion-relevant energies. Ions fall into a spherically symmetric potential well formed by a highly transparent cathode, and a condensed core, consisting of mono-energetic ions, develops in the center of the device (See Fig. 1-1). Individual ions oscillate in the electrostatic well, and a recirculating, non-Maxwellian flow results. Fusion reactions then occur from high-energy collisions with the counter-streaming flow and/or with background neutral particles.

The SCIF concept was originally conceived in the 1950's^{1,2}, and experiments started in the 1960's using biased material grids to provide the accelerating potentials³. Early fusion reaction rate measurements indicated higher-than-expected neutron production, which generated much interest in these devices. Work continued through the early 1970's until power balance estimates showed that these gridded-cathode systems could not extrapolate to a power production facility². Recent theoretical concepts and analyses⁴⁻⁶, potential engineering and medical applications^{2,4,7,8}, plus a renewed interest in alternative concepts for fusion power production rekindled discussion of SCIF devices.

The remainder of this chapter further describes the motivation for SCIF-related research and identifies the particular physics issues that are addressed in this dissertation. A summary of the goals of this thesis research is then described.

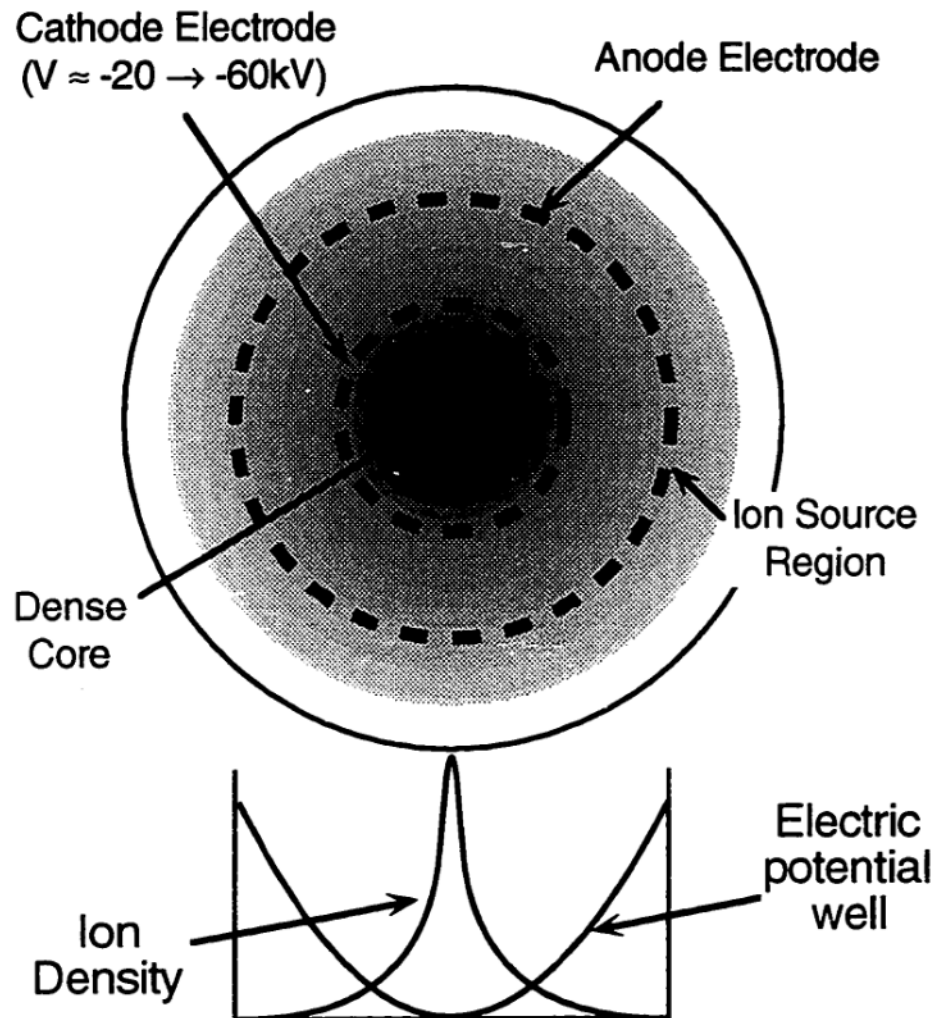


Figure 1-1. Schematic of a typical SCIF device. Ions introduced at the edge are spherically accelerated by a radial electric field generated by transparent concentric electrodes (material or virtual). The recycling, converging flow of ions creates a peak in the ion density at the center.

1.1 MOTIVATION OF SCIF RESEARCH

Advantages of a SCIF system are that energetic ions are easily obtained, the cathode potential may be tuned in energy to the peak cross-section for many different fusion reactions (i.e. D-T, D-³He, p-¹¹B, and p-⁷Li), and the fuel inventory is lower than conventional particle sources. SCIF devices can then produce high-energy neutrons, protons, alphas, etc., and they may make attractive sources (10^6 - 10^{12} particles/s) suitable for neutron activation or scattering analysis, oil well logging, and detection of chemical weapons or explosives^{2,4,7,8}. A gridded-SCIF design also has a small apparatus size and simple construction, making it a potential candidate for remote or portable sources of particles and isotopes. However, the required fusion reaction rates for many applications exceed those achieved in SCIF devices to date (< 10^8 n/s D-D, < 10^{10} n/s D-T)^{3,9-12}.

Some researchers have also suggested SCIF-type devices for space propulsion^{9,13} and power generation^{4,5,10,11,14} based on optimistic performance scalings. In contrast, other theoretical appraisals of such systems, which more extensively account for thermalizing collisional effects and the overall power balance, determined that a power production scheme is not possible without circumventing many formidable physical difficulties^{15,16}. These included the ion source requirements, the electrostatic potential well structure, symmetry, and stability, the effects of collisions (neutral or Coulomb) on the ion flow, and the origin and distribution of the fusion reactivity in these systems. In spite of this, proponents were calling for a change in the direction of the fusion program with an increased emphasis in alternates such as the SCIF concept. However, in the face of a declining fusion research budget (and the resulting increase in competition for the remaining dollars), there was a need for a clearer fundamental understanding of these systems to justify any substantial allocation of resources for such alternates.

This resulted in a modest surge of small-scale experimental activity on SCIF-type devices, and three main approaches in providing the electrostatic trap for the ion flow are currently under study. The oldest and simplest method is to apply high-voltage to a transparent material grid that ions can pass through and focus at the center. The other two systems generate virtual cathodes and avoid many performance-restricting problems associated with the gridded systems (*e.g.* cathode power and stress-loading limitations). One is the Polywell™ concept, wherein a polyhedral magnetic cusp configuration confines high-energy electron beams that form a perfectly transparent virtual cathode^{4,5}. The other approach confines high-energy electrons in a Penning or similar trap, which results in a spherically symmetric potential well for ions¹⁴.

The goal of the Wisconsin Spherically Convergent Ion Focus (WISCIFF) experiments was to investigate the fundamental ion flow physics and its relation to the fusion reaction rate in SCIF-type devices. Many of the issues listed above were investigated, and the experiments were conducted in two major steps: ion flow characterization and fusion source measurements.

1.2 ION FLOW CHARACTERIZATION

Despite the differences in the origin of the confining electrostatic fields, a common figure-of-merit for all proposed SCIF approaches is the attainable degree of focusing of the ion flow at the center. This is known as the flow convergence, and it is a critical parameter for all high-reactivity designs which rely on the counter-streaming ion flows providing the system reactivity. Physical processes that may limit the flow convergence include the structure of the electrostatic well in the presence of the ion flow, the magnitude of asymmetries in the confining potential, and scattering collisions with background neutrals or counter-streaming ions.

The presence of any virtual anode structure, due to excess ion accumulation at $r \approx 0$, can perturb the ion flow and convergence as well as change global collisional effects through changes in the ion energies locally at $r \approx 0$. In addition, this anode would presumably trap electrons, and some investigators, using one-dimensional theoretical models, suggest that a secondary virtual cathode may form inside the virtual anode^{3,17-19}. It is further speculated that an energetic, recirculating population of ions could be trapped in this virtual cathode, which may explain the high fusion reaction rate performance of the early experiments. However, no conclusive evidence of such deep, core potential structures have been observed experimentally, and models that relax the perfectly radial, collisionless assumption do not predict the multiple-well formation^{20,21}.

Potential well asymmetries are usually defocusing and hence would be expected to degrade the spherical ion flow. This, in turn, leads to a more diffuse ion core region with a correspondingly reduced fusion production for SCIF devices that rely on reactions between the counter-streaming ion flows.

The convergence to a high density core near $r = 0$ can also be significantly influenced by collisional perturbations of the recirculating ion orbits in the potential well. Scattering at large radii may give the ions excess angular momentum and defocus the flow, but charge-exchange collisions may improve the observed flow convergence by removing ions before they perform many transits through any asymmetric potentials. Nevins¹⁵ and Ryder¹⁶ also predicted that thermalization of ion flows through core collisions would lead to the collapse of the convergence in an idealized, highly-recycling ion flow.

In spite of these arguments, there is little to no past experimental data on the generic behavior of the ion flow in SCIF devices. The purpose of the work discussed herein was to provide such critical data, which will, in turn, improve the fundamental understanding for all types of these systems. A flexible, gridded-electrode scheme was chosen for these

experiments due to its relatively simple and inexpensive design, and electrostatic probes and visible imaging diagnostics were used to characterize the ion flow.

These experiments concentrated on low density, lower energy ($n \sim 10^{16} \text{ m}^{-3}$, $E_i \approx 5\text{-}20 \text{ keV}$) SCIF operation, where past experiments indicated significant fusion production⁸⁻¹⁰. Lower neutral pressure ($\leq 50 \text{ mPa H}_2$), converged-core ion flows were studied in order to minimize the effects of neutral collisions on the flow dynamics. The resulting discharge characteristics differ from the glow discharge modes studied previously, and unique measurements of the flow convergence, electrostatic potential, and ion density are presented in Chapter 5.

1.3 FUSION SOURCE MEASUREMENTS

Investigations of the fusion production in past SCIF-type experiments have not provided a clear picture of the resulting fusion source. The first experiments of this type were carried out by Hirsch³, using high-energy ion guns as a source of ions. The fusion-produced neutron rates measured in these experiments (approaching 10^{10} n/s in D-T) were much higher than predicted using an ideal, collisionless estimate. Recently, much work has been performed with devices using a transparent grid as the cathode and either a diffuse edge plasma or a spherical glow discharge as the ion source. Neutron production rate measurements performed in these gridded sources used by Miley, *et al.*⁸⁻¹¹, and discussed herein, are below those of Hirsch, presumably due to the use of discrete, directed ion guns in Hirsch's work at energies considerably higher than those used in spherical grid experiments (i.e., 75 keV/amu vs. 25 keV/amu). However, the gridded systems also often show more fusion production (as much as a factor of 5 higher) than the ideal, collisionless expectations. To a large degree, it is this appearance of an unexplained, anomalously high fusion production in these devices which has driven the interest in them.

To explain the enhanced fusion neutron production in his ion gun experiment, Hirsch suggested a “multiple-well” theory, where ions are trapped in a concentric virtual anode/cathode structure near the origin of the device³. However, later theories which include effects of angular momentum in the ion flow do not predict such multiple-well structures, and no direct experimental evidence of such structures has been obtained. An alternative explanation came from Baxter and Stuart²², who investigated the impact of charge-exchange on the ion beam distribution and the resulting system fusion neutron production, but required an increase in the fill gas pressure by 20 or more than reported in the experiments to explain the early experimental findings. In general, the basic sources of fusion reactions observed in low power experiments to date remain experimentally unexplored and hence unexplained. Therefore, it has been difficult to judge the viability of these devices for proposed applications.

The focus of the WISCIF fusion source experiments was on the resolution of these ambiguities by determining the physical origin of the fusion reactions for these devices. The possible sources include ions or fast neutrals reacting with the counterflowing particles (beam-beam reactions), the background neutral gas density (beam-background), or the atoms trapped near the surface of the cathode (beam-cathode). Experiments designed to address these issues were performed using deuterium for cathode voltages up to 60 kV, cathode currents up to 250 mA, and with a steady-state cathode power up to 6 kW. Typical system fusion rates range between 10^6 and 10^7 reactions per second, which is already above the requirements for some near-term applications.

The relative strengths of the various sources of fusion neutrons in these devices were investigated, and the influence of the cathode grid design on the fusion neutron production rate was also determined. A model including the effects of charge-exchange on the highly-

recycling ion flow was developed for the WISCIF experiment, and the results from these experiments are presented in Chapter 6.

1.4 SUMMARY OF OBJECTIVES

Again, the goal of the WISCIF experiments was to study the basic ion flow characteristics and the resulting fusion reaction rate of a SCIF-type device to develop a deeper understanding of these systems. To achieve this goal, the objectives of this thesis research were:

- (1) Construct a facility capable of producing collisionless ion flows (with respect to neutrals) and flows of higher density and power than previously studied.
- (2) Characterize the electrostatic potential, flow convergence, and core ion density of this SCIF-type device.
- (3) Determine the source and systematic dependencies of the resulting D-D fusion reaction rate.
- (4) Compare these results to simple models in order to gain insight into the physical processes that determine the electrostatic potential, flow convergence, core ion density, and fusion reaction rate.

This dissertation is organized with a discussion of a lowest-order physical model of a SCIF device in Chapter 2 and a review of past theoretical and experimental work in Chapter 3. Chapter 4 contains a description of the WISCIF device and diagnostics, and Chapters 5 and 6 include the results and conclusions from the ion flow characterization and the fusion reaction rate measurements. A summary then follows in Chapter 7.

1.5 REFERENCES

- ¹W. C. Elmore, J. L. Tuck, and K. M. Watson, *Phys. Fluids* **2**, 239 (1959).
- ²T. J. Dolan, *Plasma Phys. Controlled Fusion* **36**, 1539 (1994).
- ³R. Hirsch, *J. Appl. Phys.* **38**, 4522 (1967).
- ⁴R. W. Bussard, *Fusion Technol.* **19**, 273 (1991).
- ⁵N. A. Krall, *Fusion Technol.* **22**, 42 (1992).
- ⁶D. C. Barnes, R. A. Nebel, and L. Turner, *Phys. Fluids B* **5**, 3227 (1993).
- ⁷G. H. Miley, J. Javendani, Y. Yamamoto, R. Nebel, J. Nadler, Y. Gu, A. Satsangi, and P. Heck, Third International Conference on Dense Z-Pinches, eds. M. Haines and A. Knight, AIP Conference Proceedings 299, AIP Press, 675 (1994).
- ⁸G. L. Kulcinski, Fusion Technology Institute Report #UWFDM-1025 (1996).
- ⁹J. H. Nadler, G. H. Miley, Y. Gu, and T. Hochberg, *Fusion Technol.* **21**, 1639 (1992).
- ¹⁰G. H. Miley, J. Nadler, T. Hochberg, Y. Gu, O. Barnouin, J. Lovberg, *Fusion Technol.* **19**, 840 (1991).
- ¹¹J. H. Nadler, G. H. Miley, Y. Gu, and T. Hochberg, *Fusion Technol.* **20**, 850 (1991).
- ¹²A. L. Gardner, D. M. Hatch, A. I. Y. Chan, and R. P. Evans, *Ann. NY Acad. Sci.* **251**, 179 (1975).
- ¹³R. W. Bussard, *J. Propulsion and Power* **6**, 567 (1990).
- ¹⁴D. C. Barnes, R. A. Nebel, and L. Turner, *Phys. Fluids B* **5**, 3227 (1993).
- ¹⁵W. M. Nevins, *Phys. Plasmas* **2**, 3804 (1995).
- ¹⁶T. H. Rider, *Phys. Plasmas* **2**, 1853 (1995).
- ¹⁷B. E. Cherrington, J. T. Verdeyen, and D. A. Swanson, *Ann. NY Acad. Sci.* **251**, 139 (1975).
- ¹⁸J. T. Verdeyen, B. E. Cherrington, D. A. Swanson, and D. J. Meeker, *Ann. NY Acad. Sci.* **251**, 126 (1975).
- ¹⁹T. J. Dolan, J. T. Verdeyen, D. J. Meeker, and B. E. Cherrington, *J. Appl. Phys.* **43**, 1590 (1972).
- ²⁰W. M. Black, and J. W. Robinson, *J. Appl. Phys.* **45**, 2497 (1974).

²¹W. M. Black, and E. H. Klevans, *J. Appl. Phys.* **45**, 2502 (1974).

²²D. C. Baxter and G. W. Stuart, *J. Appl. Phys.* **53**, 4597 (1982).

Chapter 2: Low-Order Ion Flow Model

Understanding the behavior of the ion density and velocity distributions is critical for estimating or extrapolating the fusion production of any SCIF system. To lowest order, these distributions can be approximated using an elementary collisionless ion orbit model where only radial dependencies are considered. Any perpendicular velocity of an ion is included in this model only in conserving angular momentum, and hence the radial velocity of the flowing ions is directly related to the local electrostatic potential. The ion density distribution is then determined by conserving the total ion current in the device.

The actual situation is, of course, much more involved. The local ion flow, electron distribution, and the plasma potential distribution all interact and adjust themselves accordingly to achieve a self-consistent equilibrium. This leads to deviations of the plasma potential distribution from the imposed vacuum field. For example, excess ion charge in the core region can lead to a virtual anode there and cause scattering of the incident ions. A full description of the system in dynamic equilibrium awaits solution of the Fokker-Planck equation in the fully three-dimensional environment. However, the simple ballistic model discussed here is traditionally taken to provide a lowest-order description of the system, and it can be employed to indicate the expected scalings of critical parameters with system properties and thus provide a starting point for comparison with experiment.

In general, the ion flow characteristics change throughout the SCIF system, and it is helpful to distinguish them for different regions (See Fig. 2-1):

$r > R_a$	\rightarrow	Edge
$r_{cat} < r \leq R_a$	\rightarrow	Mantle
$r_c < r \leq r_{cat}$	\rightarrow	Plateau
$r \leq r_c$	\rightarrow	Core

where R_a is the anode radius, r_{cat} is the cathode radius, and r_c is the core radius, defined as the radius where the perpendicular velocity of the ion flow becomes significant and the density no longer increases as $1/r^2$.

Figure 2-2 indicates the idealized background ion distributions for the various zones identified above. For the low pressure discharges, a cold plasma is generated at the edge, and any ions moving toward the cathode are accelerated to full energy in the mantle region. The plateau zone ideally contains mono-energetic ions inside the cathode, and the core distribution consists of a thin, spherical shell in velocity space at a radius of the core velocity.

These different distributions then give rise to the resulting fusion reactivity for a SCIF device. The sources of reactivity include beam-beam, beam-background, beam-cathode, and fast-neutral-background collisions. Here, beam indicates the primary fast ions accelerated by the spherical potential well, background indicates the cold neutral fill gas atoms or molecules, cathode indicates the trapped fuel density in the solid cathode, and fast-neutral indicates energetic neutral atoms produced by charge-exchange or other collisions between the beam ions and the background gas. Assuming spherical symmetry, the total system fusion reaction rate (R_{fus}) is given by:

$$R_{fus} = 4\pi \int_0^P r^2 dr n_f(r, v) \left[n_0 \overline{\sigma_f v(r)_0} + \frac{n_f(r, v)}{4} \overline{\sigma_f v(r)_f} \right] + R_{fus, cat} \quad (2.1)$$

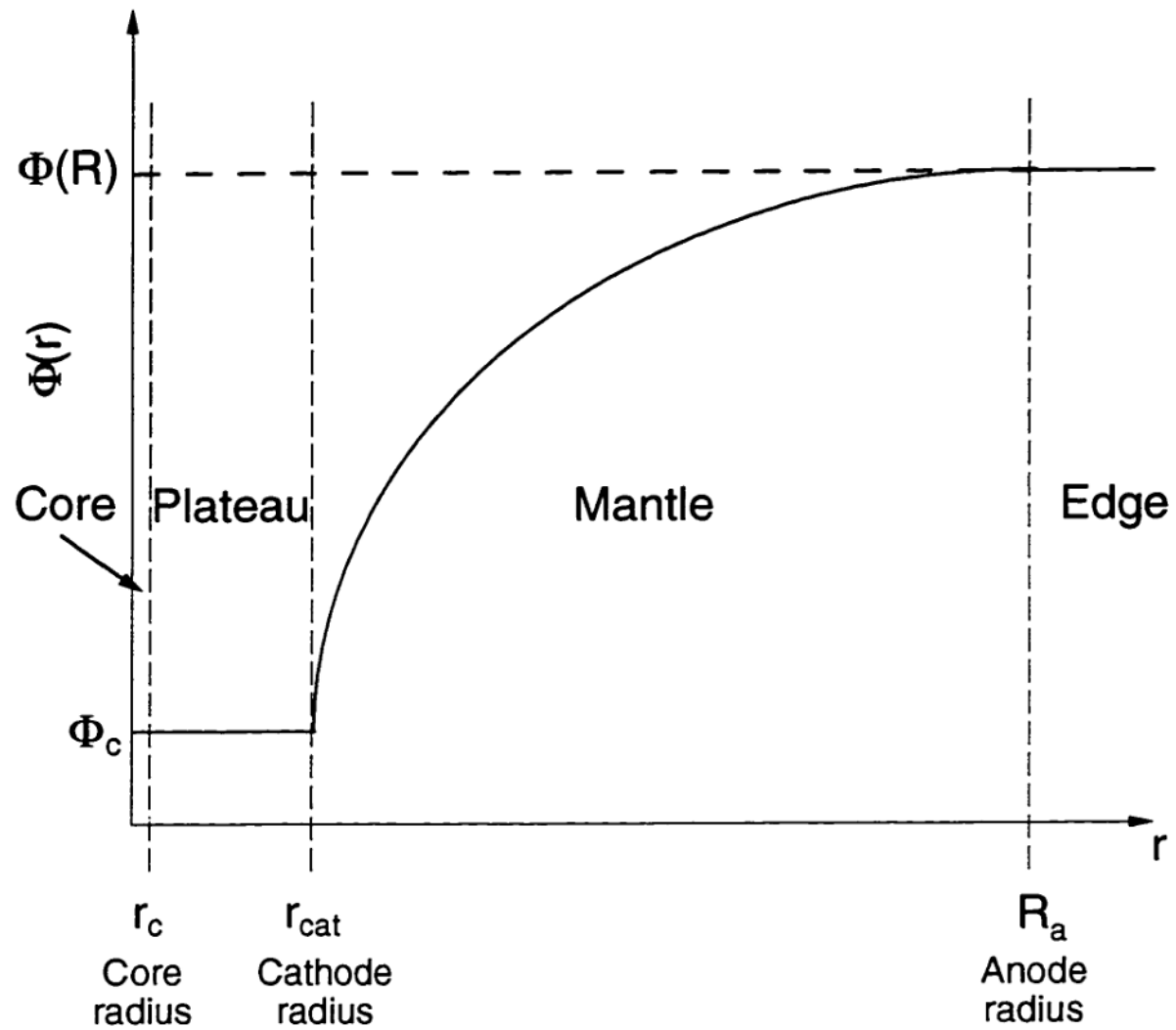


Figure 2-1. Definitions for the four regions of interest in a SCIF device.

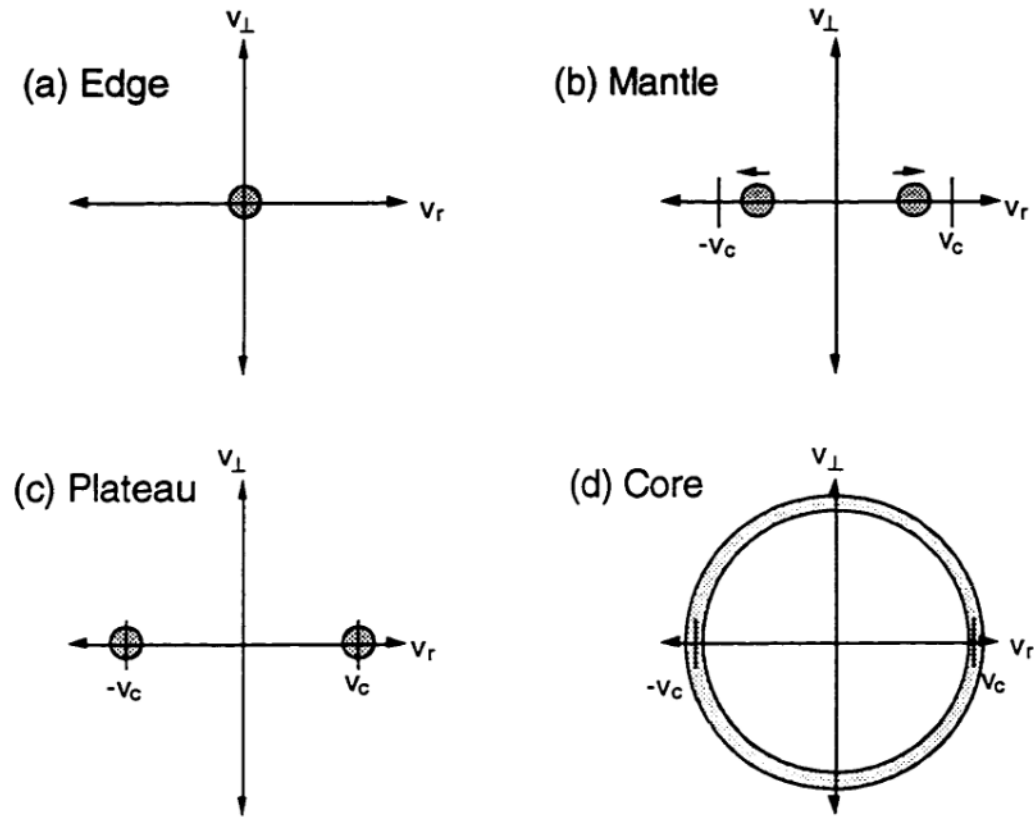


Figure 2-2. Qualitative behavior of the ideal background ion velocity distributions in the lab frame for the different regions of interest (not to scale) — (a) edge: cold, thermal at $\langle v \rangle = 0$, (b) mantle: low T_i , $v_r < v_c$, (c) plateau: $v_r = \pm v_c$, (d) core: isotropic shell $|v_r| = v_c$. In all cases, $T_i \ll \Phi_c$.

where ρ is the radius of the reaction volume, $n_f(r, v)$ is the fast particle density (ions or fast neutrals), n_o is the neutral fuel gas density, $\sigma_f v(r)$ is the fusion reaction rate (which must be averaged over the appropriate relative velocities of the target particles), and $R_{fus,cat}$ is the contribution from the trapped particles in the cathode. The first term in Eq. (2.1) refers to reactions that scale linearly with the injected current ($n_f \propto I$), and the second term describes beam-beam interactions, which scale as the injected current squared.

It is apparent from Eq. (2.1) that knowledge of the ion density and velocity distributions is critical for estimating the fusion performance of a particular system. The rest of this chapter will focus on the description of models that estimate the radial ion density and electrostatic potential (and hence ion energy) distributions. The expected system fusion reaction rate, based on these model distributions, will also be discussed.

2.1 IDEAL ION CONVERGENCE LIMIT

A simple estimate of the expected density profile behavior is given by first assuming a perfectly convergent, non-interacting flow into the core. Angular momentum of the ions at the edge, due to their perpendicular thermal velocity, $v_\perp(R_a)$, will keep the flow from perfectly converging to $r = 0$, but to lowest order, one can assume the flow is converging to a radius r_c , defined as the core radius. All ions are assumed to be non-interacting and flow through the core with a velocity $v_c = \sqrt{2q\Phi_c/M}$, where $-\Phi_c$ is the electric potential in the core [for $\Phi(R_a) = 0$], q is the ion charge, and M is the ion mass. By setting the average angular momentum of the ions at the edge equal to that of the ions passing through the core, $M \langle v_\perp \rangle R_a = (2/3) M v_c r_c$, the core radius is then given by:

$$r_c = \frac{3}{2} R_a \frac{\langle v_\perp \rangle}{v_c} \approx \frac{3}{2} R_a \sqrt{\frac{kT_{edge}}{q\Phi_c}} \quad (2.2)$$

where T_{edge} is the edge ion temperature. Therefore, r_c should scale as the inverse square root of Φ_c .

2.2 RADIAL DENSITY DISTRIBUTION MODELS

Assuming no sources or sinks of particles, total current conservation demands that $n_i(r)v(r)r^2 = \text{constant}$ for all r , where $n_i(r)$ is the local ion density. The expected steady-state radial profile is then:

$$n_i(r) = n_i(R_a) \left(\frac{R_a}{r}\right)^2 \frac{v(R_a)}{v(r)} = n_i(R_a) \left(\frac{R_a}{r}\right)^2 \sqrt{\frac{E_{||}(R_a)}{q\Phi(r)}} \quad (2.3)$$

where $E_{||}(R_a)$ is the radial energy of the ions at the edge. This is adequate to describe purely radial flow, but in the core region ($r \approx 0$) this relation diverges. Angular momentum conservation will prevent this divergence, and some estimates for ion core density distribution that account for angular momentum are discussed below.

2.2.1 Constant core density model

A constant density can be invoked in the core to provide a lowest-order estimate for the core ion density distribution. Since the effective core area is a circle of radius r_c , the core density is then:

$$n_{ic} = 4n_i(R_a) \left(\frac{R_a}{r_c}\right)^2 \frac{v(R_a)}{v_c} = 4n_i(R_a) \left(\frac{R_a}{r_c}\right)^2 \sqrt{\frac{E_{||}(R_a)}{q\Phi_c}} \quad (2.4)$$

By substituting for r_c from Eq. (2.2), an estimate for the convergence factor (ratio of core to edge density) is found from Eq. (2.4):

$$\frac{n_{ic}}{n_i(R_a)} = \frac{16}{9} \frac{\sqrt{E_{||}(R_a)}}{kT_{edge}} \sqrt{q\Phi_c} \quad (2.5)$$

Therefore, the core density should optimally scale as the square root of the core potential for given edge plasma conditions. This model conserves average angular momentum and total particle flux through the core region, but it fails to keep the density continuous at r_c .

2.2.2 Distributed Maxwellian source model

A slightly more complex model, relaxing the perfect convergence assumption inside the cathode and using a Maxwellian distribution of transverse edge velocities, can be applied to better approximate the ion density profile inside the cathode and avoid the discontinuity at $r = r_c$. Purely radial flow is still assumed in the mantle region, and the ions are expected to have a single radial velocity at the cathode (v_c). The normalized ion velocity distribution function at r_{cat} is then:

$$f(v_r, v_\perp) dv^3 = \frac{n_{i,cat}}{\pi v_{T,\perp}^2} \delta(v_r - v_c) \exp\left(-\frac{v_\perp^2}{v_{T,\perp}^2}\right) dv_r v_\perp dv_\perp d\phi \quad (2.6)$$

where v_r and v_\perp are the radial and perpendicular ion velocities and $v_{T,\perp}$ is the perpendicular ion thermal velocity at the cathode. By conserving the angular momentum of the ions from the edge, the expression for $v_{T,\perp}$ becomes:

$$v_{T,\perp}^2 = \frac{2kT_{edge}}{M} \left(\frac{R_a}{r_{cat}}\right)^2 \quad (2.7)$$

Assuming that $E_{||}(R_a)$ is equal to the parallel thermal velocity of the ions [or $E_{||}(R_a) = kT_{edge}/2$], then $n_{i,cat}$ is given by Eq. (2.3) to be:

$$n_{i,cat} = n_i(R_a) \left(\frac{r_{cat}}{R_a}\right)^2 \sqrt{\frac{2kT_{edge}}{q\Phi_c}} \quad (2.8)$$

To determine the radial ion density distribution, Eq. (2.6) will be used to calculate the ion flux from a point P at the cathode radius that passes through an aperture da located at a

height r from the origin. Figure 2-3 shows the geometry for the calculation, where the normal to da points in the y -direction (i.e. da lies in the x - z plane), P is located by the spherical coordinates (r_{cat}, θ, ϕ) , \mathbf{L} is the vector from R_I to da , and \mathbf{R} is the vector from the origin to P . The ion flow is mainly radial (since $q\Phi_c \gg kT_{edge}$) and is only appreciable near the origin. Therefore, only small angle deviations from the radial direction ($\gamma \ll 1$) need to be considered, and $|\mathbf{L}| \approx |\mathbf{R}| = r_{cat}$.

Equation (2.6) can be written in terms of γ ($= v_\perp/v_c$) as:

$$f(v_r, \gamma) dv_r d\Omega = \frac{n_{i,cat}}{\pi} \frac{v_c^2}{v_{T,\perp}^2} \delta(v_r - v_c) \exp\left(-\frac{v_c^2 \gamma^2}{v_{T,\perp}^2}\right) dv_r d\Omega \quad (2.9)$$

where $d\Omega$ is the differential solid angle for the flow relative to the radial direction ($d\Omega = \gamma d\gamma d\phi$). The solid angle subtended by the area da when viewed from the point P is also represented by $d\Omega$.

The number of ions passing through da from the area dA centered on P per unit time (dN/dt) is then expressed as:

$$\frac{dN}{dt} = \int dA \left(\frac{d\Gamma}{d\Omega} \right) \cdot d\Omega \approx 2r_{cat}^2 \int_0^\pi d\phi \int_{-1}^1 d(\cos \theta) f(v_c, \gamma) v_c d\Omega \quad (2.10)$$

By substituting Eq. (2.9) into Eq. (2.10) and using the necessary solid/vector geometry relations [*i.e.* $\gamma = (r/r_{cat})\sin \theta$, $d\Omega = da(\sin \theta)(\sin \phi)/r_{cat}^2$], the expression for the radial ion density distribution is determined by integrating Eq. (2.10):

$$n_i(r) = \frac{dN}{dt da} \frac{1}{v_c} \approx \sqrt{2} n_i(R_a) \left(\frac{R_a}{r_o} \right)^2 \sqrt{\frac{kT_{edge}}{q\Phi_c}} \int_{-1}^1 dx \exp\left[-\frac{r_o^2}{r_o^2}(1-x^2)\right] \quad (2.11)$$

where $x = \cos \theta$ and r_o is defined to be:

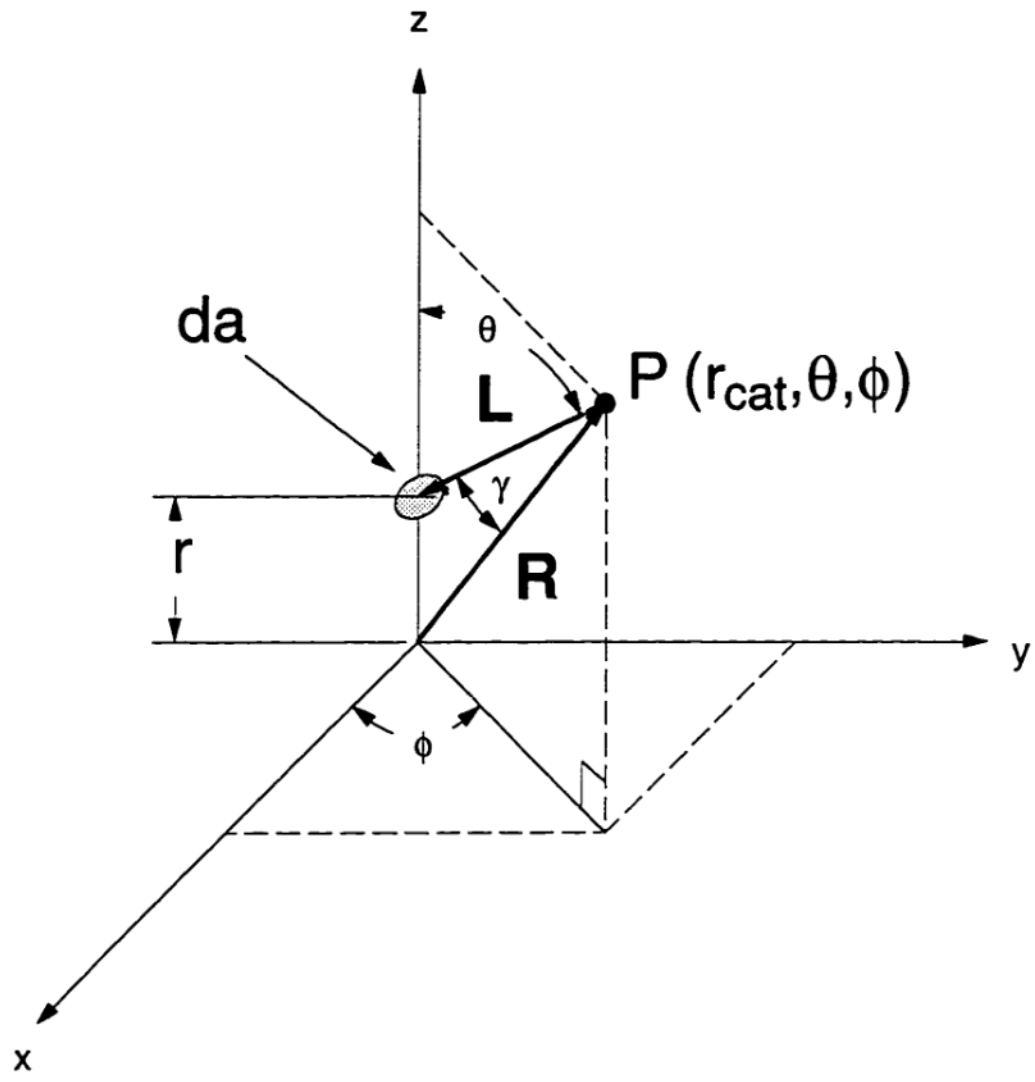


Figure 2-3. Geometry of the ion density distribution calculation for the distributed Maxwellian source model discussed in the text.

$$r_o \equiv R \sqrt{\frac{kT_{\text{edge}}}{q\Phi_c}} = \frac{2}{3} r_c \quad (2.12)$$

Figure 2-4 shows the differences in the radial distributions between this model and the more simplified estimate [Eqs. (2.3) and (2.4)]. The system fusion reaction rate between these two models [from Eq. (2.1)] agree within 5%, and thus the simplest model should provide a reasonable lowest-order estimate.

2.2.3 Cathode current estimate for the core ion density

For a collisionless gridded system, the amount of recirculating current (and hence the resulting core density) is limited by the effective cathode transparency. Assuming that the ions are equally likely to be lost at each pass through the cathode, the recirculation density enhancement factor, ξ , is given by¹:

$$\xi \equiv \frac{I_{\text{man}}}{I_{\text{cat}}} = \frac{1}{(1 - \eta^2)} \quad (2.13)$$

where I_{man} represents the total ion current in the mantle region, I_{cat} is the ion current collected by the cathode and η is the geometric grid transparency [$\eta \equiv (\text{open area})/4\pi r_{\text{cat}}^2$]. If the number of secondary electrons emitted from the grid due to ion impact is given by δ_e , then the measured ion grid current (I_{meas}) is $(1 + \delta_e)I_{\text{cat}}$, and the recirculation factor relates to the measured grid current by:

$$\xi = \frac{I_{\text{man}} (1 + \delta_e)}{I_{\text{meas}}} \quad (2.14)$$

Another approximation of the core density is then given by the measured cathode current. For a gridded system, the effective transparency (η) leads to a fractional loss of the current between the mantle (I_{man}) and core (I_c) regions, and hence, $I_c = \eta I_{\text{man}}$. Using the

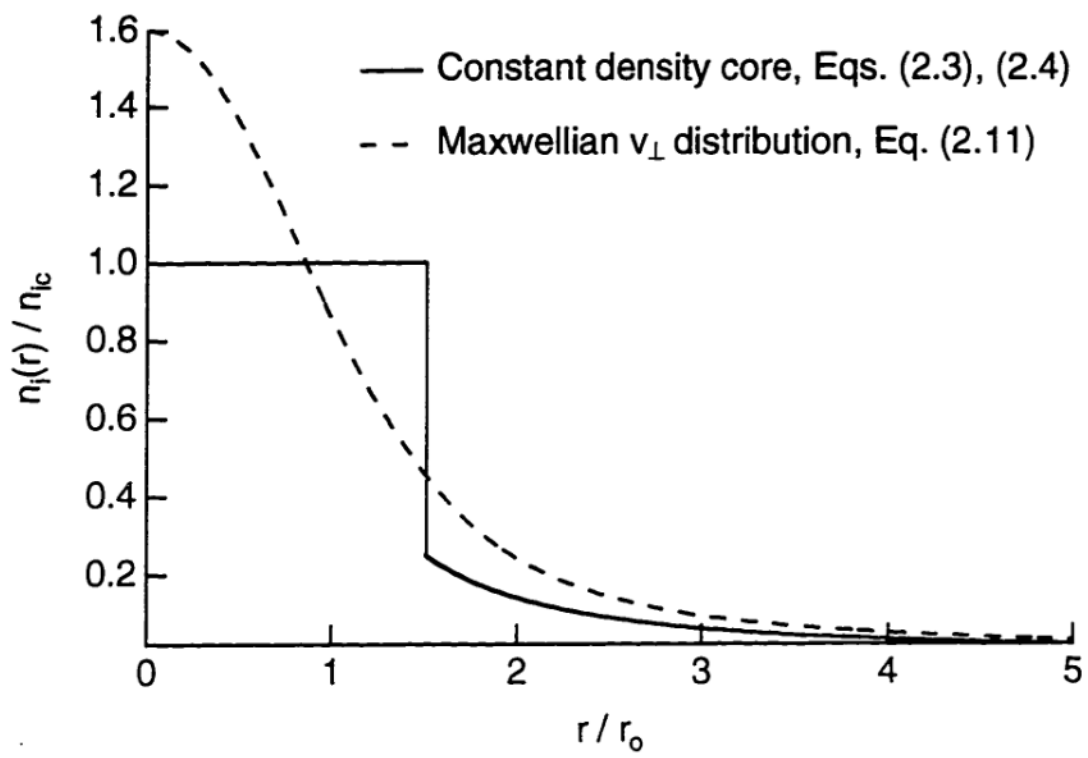


Figure 2-4. Density profile comparison between the two models discussed in the text. Here it is assumed that $E_{||}(R_a)$ used in Eq. (2.4) is equal to $kT_{edge}/2$.

definition of the recirculation factor [Eqs. (2.13) and (2.14)], I_c can be related to the measured grid current (I_{meas}) by:

$$I_c = \eta I_{man} = \frac{\eta \xi I_{meas}}{(1 + \delta_e)} = \frac{\eta I_{meas}}{(1 - \eta^2)(1 + \delta_e)} \quad (2.15)$$

which can also be related to the core density since $I_c = e n_{ic} v_c \pi r_c^2$. Therefore, the expected core density for a particular grid current is:

$$n_{ic} = \frac{\eta I_{meas}}{(1 - \eta^2)(1 + \delta_e)} \left(\frac{1}{e v_c \pi r_c^2} \right) \quad (2.16)$$

which can be used if the core size (r_c) and ion core velocity (v_c , related to the core electrostatic potential) is given. The radial ion density distribution is then given by Eq. (2.3) using the value of n_{ic} given in Eq. (2.16) above.

Hence, the density profile depends critically on the potential profile if current is to be conserved [from Eq. (2.3)], and the next section discusses a model estimate for the potential distribution.

2.3 ELECTRIC POTENTIAL PROFILE

In the past, investigators have tried to derive the potential and density profiles in spherical flows from Poisson's equation and conservation of energy and momentum. Using simplifying assumptions, they were able to develop some understanding of the electrostatic potential distribution, and their findings are discussed in more detail in Chapter 3.

In contrast, a lowest order model, where space-charge-limited flow is assumed between the outer anode and the inner cathode, is discussed here to determine the behavior of an ideal system for different injection currents and cathode voltages. This model will also

prove to be useful in obtaining quantitative results for comparisons with the findings described later in Chapter 5. Problems with obtaining a reasonable potential distribution inside the cathode radius will be discussed, and here it will just be assumed that the potential profile is flat in that region, as shown in Fig. 2-1.

The core density and system reactivity will ultimately depend on how much recirculating ion current can be sustained, and the resulting ion space-charge limits the magnitude of this current for steady-state systems. The ideal space-charge-limited ion current between concentric spheres (mantle region) is²:

$$I_{\text{man}} = \frac{16\pi\epsilon_0}{9} \sqrt{\frac{2q}{M}} \frac{V^{3/2}}{\alpha^2} \quad (2.17)$$

where ϵ_0 is the permittivity of free space, q is the ion charge, V is the voltage difference between the spheres, and α is a geometrical factor that is related to the radii of the spherical electrodes:

$$\alpha = \gamma - 0.3\gamma^2 + 0.075\gamma^3 - 0.0143182\gamma^4 + 0.0021609\gamma^5 + \dots \quad (2.18)$$

with $\gamma = \ln(r/R_a)$. Assuming no sources or sinks of particles between the electrodes (consistent with low pressure and density), Eq. (2.17) can be solved for the voltage:

$$V(r) = \left[\frac{9I_{\text{man}}\alpha^2(r)}{16\pi\epsilon_0} \sqrt{\frac{M}{2q}} \right]^{2/3} \quad (2.19)$$

where α determines the radial dependence ($\alpha \rightarrow 0$ as $r \rightarrow R_a$). This equation, derived originally for solid electrodes, also holds for semi-transparent grids with counterstreaming ion flows if I_{man} represents the total recirculating ion current between the spheres. By comparing the measured radial electrostatic potential distribution, $V(r)$, with Eq. (2.19), the total recirculating current between the spheres, I_{man} , can be determined, and then an estimate for ξ is given by Eq. (2.14) using the measured grid current.

Determining the potential inside the cathode is more complicated. The ion space charge would presumably stagnate the flow at some radius r_{stag} for a purely radial, collisionless flow with single-species injection. This stagnation radius can be determined by solving Eq. (2.17) for α and using Eq. (2.18) to find the appropriate r_{stag}/r_{cat} . Therefore, electron effects would have to be considered in order to flatten the potential profile, but these effects have been ignored up to this point.

If a virtual anode did form, it could then trap electrons in this spherically symmetric well. Hirsch³ postulated that these electrons could form a virtual cathode in the same manner providing a perfectly transparent trap for high recirculating currents of ions. However, the presence of electrons would seriously alter the space-charge and potential distributions and may even prevent the formation of the first virtual anode. This subject is still under considerable debate among different investigators and is discussed in more detail in Chapter 3.

What one does learn from the simple models described above is that the core density should ideally scale as the square-root of the applied cathode potential and linearly as the injected current. Ideal circumstances would also lead to space-charge-limited current to be drawn in the system. Comparisons of these models with results obtained from the WISCIF experiment are described in Chapter 5.

2.4 TOTAL FUSION PRODUCTION RATE ESTIMATES

It has been suggested that $\sigma_f v(r)$ for beam-beam reactions may be higher for a SCIF system, for ideally the ions are monoenergetic with the energy of the applied cathode potential and can be tuned to the peak of the fusion cross section^{4,5}. This may be true in the plateau and mantle regions of the device, but one can show that in the core region (where the

ion densities are highest) the reaction rates are not much different than those given by a Maxwellian distribution if the angles of incidence of the ion beams are taken into account (See Appendix 1 and Fig. 2-5)⁶. However, the reaction rate in the plateau and mantle regions can be a factor of 1.7 higher than that in the core due to the counterstreaming distribution of the target ions (See Fig. 2-6, D-T case shown).

Figure 2-6 also indicates that the beam-beam interaction energy is twice that of the local plasma potential energy (due to the counterflowing beams). The beam-background interactions are represented by the mantle reaction rate, but the interaction energy is equal to the local plasma potential (or half that of the beam-beam collision energy). At lower voltages, this tends to make beam-beam reactions more likely, but only one-half of the ion density can react with the other half, which introduces the factor of 1/4 in the total fusion production rate calculation [See Eq. (2.1)]. Therefore, the relative contributions of beam-beam versus beam-background reactions will depend on the magnitude of the neutral gas density compared to the ion density.

For typical operating parameters from past experiments^{3,7,8} ($P \sim 500$ mPa, $I_{meas} \sim 20$ mA), Eq. (2.16) estimates the core ion density to be $\sim 10^{15}$ m⁻³ (assuming $\delta_e = 1$, $r_c = 5$ mm, $\eta = 0.95$, and a core ion energy of 35 kV), which is much less than the neutral gas density ($\sim 10^{20}$ m⁻³). Hence, the beam-background reactions should be stronger compared to the beam-beam interactions for these past experiments.

This can be further confirmed by estimating the fusion neutron production rate for the WISCF device at these conditions. The model calculation, described below, will also be useful in comparing with the experimentally measured neutron production rates discussed in Chapter 6. The first section outlines the calculation of the fusion reaction rate due to the

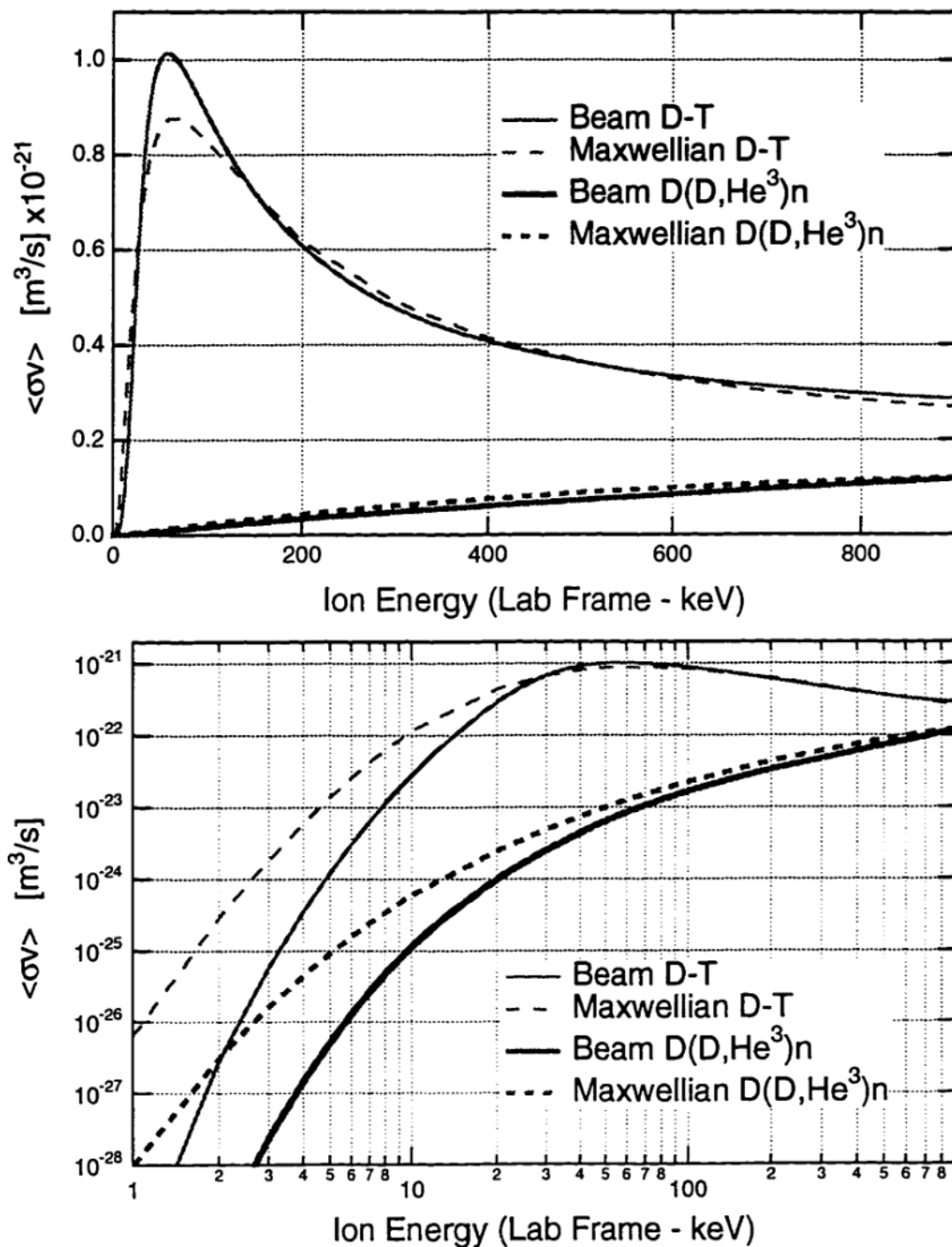


Figure 2-5. Reaction rates comparisons in D-T and D-D for spherical beam and Maxwellian distributions on a linear (top) and logarithmic (bottom) scale. See Appendix 1 for calculation.

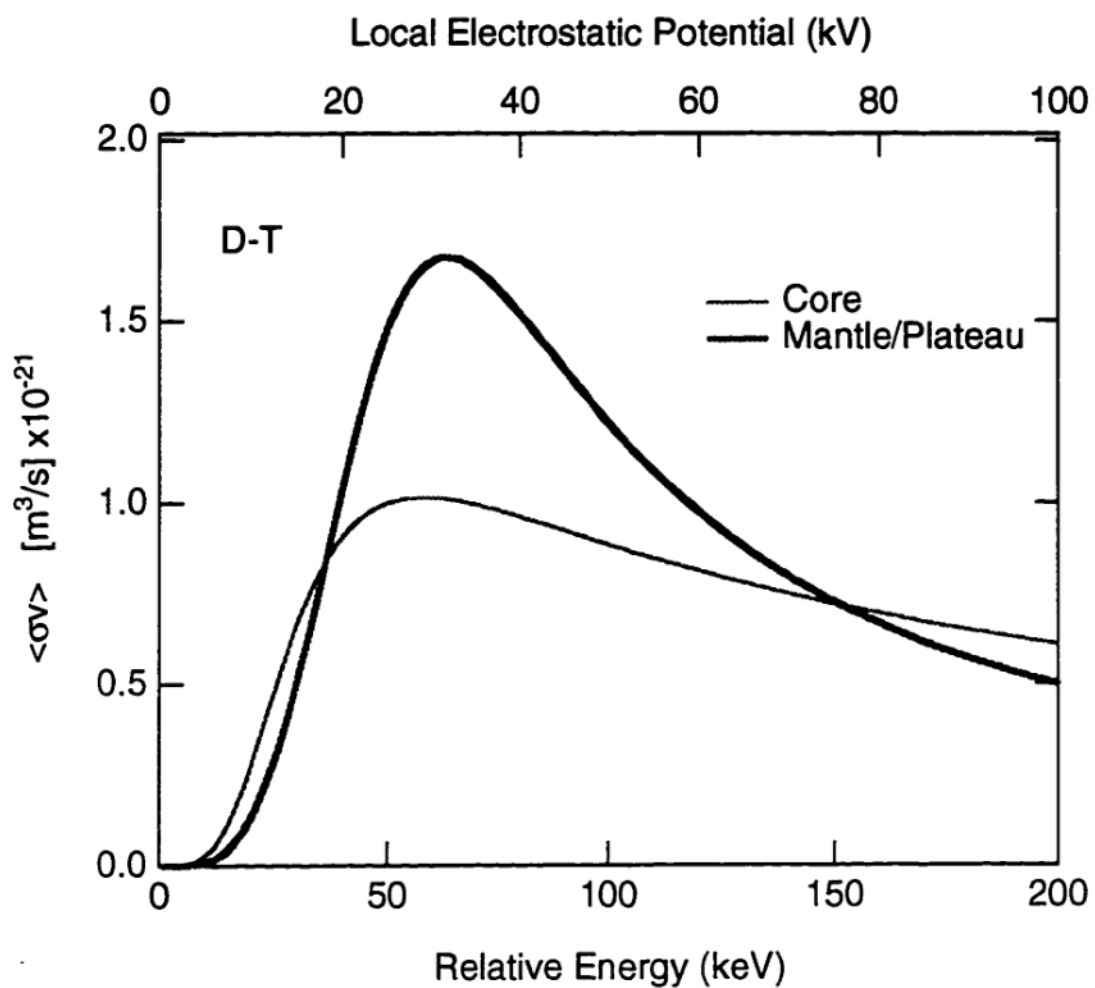


Figure 2-6. Reaction rates comparisons for the core and mantle regions (Refer to Fig. 2-2 for distributions).

flowing ions, and the second describes an estimate for the fusion reactions occurring at the cathode material surface ($R_{fus,cat}$).

2.4.1 Collisionless flow fusion neutron production rate estimate

The total fusion reaction rate is given by Eq. (2.1), where the ion density and velocity distributions are needed to determine R_{fus} . The collisionless flow model described in Section 2.2.1 above is typically used to first estimate these distributions, and therefore collisions are ignored and a mono-energetic ion distribution is assumed [e.g. $E_i = -q\Phi(r)$, hence $v_i(r) = \sqrt{2q\Phi(r)/M}$]. Since collisions would be expected to degrade rather than enhance the fusion rate, this estimate is clearly optimistic and provides an upper limit for expected values of R_{fus} with classical unperturbed ion flow.

A space-charge-limited potential distribution is assumed between the anode and the cathode, and the presence of a virtual anode, formed by the charge build-up in the core due to the convergent ion flow, is ignored to first order. Since any such anode (which has been experimentally observed) will decelerate the beam ions, this assumption also tends to overestimate the expected R_{fus} . The resulting radial potential distribution looks much like the one shown in Fig. 2-1.

The core ion density is first calculated from Eq. (2.16), given V_{cat} , I_{meas} , δ_e , η , and r_c . The remaining radial density distribution is given by the current-conservation model [$n_i(r)v_i(r)r^2 = n_{ic}v_cr_c^2$ for $r > r_c$, $\rho = R_a$]. The fusion reaction rates [$\sigma_f v(r)$] are then calculated as a function of r , [for beam-beam, $E_i = -2q\Phi(r)$, for beam-background, $E_i = -q\Phi(r)$], and the resulting $n_i(r)$ and $\sigma_f v(r)$ distributions are substituted into Eq. (2.1). The integral for the total fusion production rate (R_{fus}) is then determined numerically.

Using this model and applying the typical operating conditions of past experiments (see the calculation just above this section) to the WISCIF experiment ($r_{cat} = 0.05$ m, $R_a = 0.20$ m), Eq. (2.1) then calculates that the beam-background reaction rate is more than four orders of magnitude higher than the beam-beam rate. In addition, about 85% of the beam-background fusion reactions occur inside the cathode radius (10% in the core region, 75% in the plateau). The remaining 15% occurs in the mantle region. This is in contrast to the beam-beam spatial distribution of fusion production, where about 90% is expected inside the core and 10% in the plateau (the mantle region accounts for << 1% of the beam-beam contribution).

Since collisions with the neutral gas dominate R_{fus} and 85% of fusion reactions are expected to occur inside the cathode, a simplified estimate of R_{fus} is given by substituting $4\pi n_i v_i r^2 = I_{man} = I_{meas}/(1 + \delta_e)/(1 - \eta^2)$ into Eq. (2.1) and integrating to the cathode radius (note that σ_f is constant inside the cathode):

$$R_{fus} \approx \int_0^{r_{cat}} \frac{I_{man}}{e} n_o \sigma_f (-q V_{cat}) dr = \frac{I_{meas}}{e(1 + \delta_e)(1 - \eta^2)} n_o \sigma_f (-q V_{cat}) r_{cat} \quad (2.20)$$

where the beam-cathode contribution ($R_{fus,cat}$) in Eq. (2.1) is ignored. Equation (2.20) can be used for quick fusion rate estimates, but the full integral in Eq. (2.1) is evaluated when comparing this model to the experimentally measured neutron rates discussed in Chapter 6.

While this simple model should reflect gross system behavior, it does ignore the effects from any electrostatic potential structure or ion trapping in the core region and the influence of collisions on the total system fusion production rate. This collisionless estimate also predicts a linear dependence of the fusion rate on the neutral gas pressure, but at some point, ion-neutral collisions should effect the system reactivity.

For the energy ranges typically studied in these devices (between 20 and 70 keV), charge-exchange is the dominant ion-neutral collisional process. The confined fast ions are removed from the system and replaced with cold (and much less fusible) particles, which results in a reduced amount of fusion production due to the ions. However, the energetic neutrals can also fuse with the background gas along its orbit from the system, and some contribution to the fusion production rate is due to these fast neutrals. This is discussed in more detail in Chapter 6.

Also ignored to this point is the fusion reactions due to the energetic ions colliding with the density of neutral gas trapped at the surface of the cathode. The section below describes an estimate for this contribution to the total fusion production rate.

2.4.2 Beam-cathode contribution

Another possible source of fusion reactivity in these systems is from the cathode grid itself. For cathodes under energetic ion bombardment, a significant density of particles can become trapped in the material near the surface, and these trapped atoms then can fuse from collisions with the incoming fast ions. This contribution is the main source for beam-target-type neutron or fast particle sources^{9,10}.

For the conditions typically studied in these devices, the rate at which deuterium leaves the cathode surface is mainly limited by recombination. An approximation for the steady-state surface density is given by equating the incident ion rate with the recombination rate at the surface or:

$$\frac{I_f}{eA_{cat}} = K_r n_{cat}^2 \quad (2.21)$$

where I_f is the fast particle current, A_{cat} is the cathode surface area, K_r is the recombination rate constant, and n_{cat} is the trapped fuel density. K_r is a strong function of the material type,

temperature, and surface conditions (roughness, cleanliness, etc.), and for a particular material, the values of K_r are only known within four orders of magnitude¹¹. It appears from Eq. (2.21) that n_{cat} is proportional to the square root of the ion current, but K_r is also a function of ion current (through the temperature dependence of the cathode on ion current). These effects essentially cancel each other, and the resultant source density can be relatively independent of current.

Assuming a uniform fuel density within the effective range for the energetic particles (λ), the fusion reaction rate contribution ($R_{fus,cat}$) is therefore given approximately by:

$$R_{fus,cat} = \frac{I_f}{e} n_{cat} \lambda \sigma_f(-qV_{cat}) \quad (2.22)$$

and since n_{cat} is independent of the cathode current, $R_{fus,cat}$ is expected to scale linearly with injected current.

Comparisons of the collisionless flow model and estimates of the role of collisions on the fusion reactivity are discussed for past experiments in Chapter 3 and for the WISCIF results in Chapter 6. Estimates of the beam-cathode reaction rate from Eq. (2.22) are also compared with experimental measurements in Chapter 6.

2.5 REFERENCES

- ¹R. L. Hirsch, Phys. Fluids **11**, 2486 (1968).
- ²I. Langmuir and K. Blodgett, Phys. Rev. **24**, 49 (1924).
- ³R. Hirsch, J. Appl. Phys. **38**, 4522 (1967).
- ⁴G. H. Miley, J. B. Javedani, Y. B. Gu, A. J. Satsangi, P. F. Heck, I. D. Tzonev, M. J. Williams, S. G. DelMedico, R. A. Nebel, D. C. Barnes, L. Turner, J. H. Nadler, and J. Sved, Fusion Studies Laboratory Report # FSL-483 (1994).
- ⁵R. W. Bussard, *J. Propulsion and Power* **6**, 567 (1990).
- ⁶W. M. Nevins, Phys. Plasmas **2**, 3804 (1995).
- ⁷G. H. Miley, J. Nadler, T. Hochberg, Y. Gu, O. Barnouin, J. Lovberg, Fusion Technol. **19**, 840 (1991).
- ⁸J. H. Nadler, G. H. Miley, Y. Gu, and T. Hochberg, Fusion Technol. **20**, 850 (1991).
- ⁹J. Kim, Nuc. Instrum. and Methods **145**, 9 (1977).
- ¹⁰H. H. Barschall, in *Neutron Sources for Basic Physics and Applications*, edited by S. Cierjacks (Pergamon Press, Oxford, 1983), p. 57.
- ¹¹K.L. Wilson, in Data Compendium for Plasma Surface Interactions, (IAEA publications, 1984), p. 28.

Chapter 3. Past Theory and Experiments

The SCIF concept was first proposed as a means of confining ions of thermonuclear interest in the 1950's, but experiments did not begin until the late 1960's¹⁻³. These experiments reported higher-than-expected neutron production rates (from the collisionless model described in Chapter 2), and a flurry of theoretical and experimental work followed in the early 1970's. Much of the debate had been focused around the electrostatic potential distribution and the resulting ion density in the core and plateau regions; various models predicted conflicting behavior of these profiles, and a consensus has yet to be reached².

Past experimental results have also produced an unclear picture into the behavior of these devices due to the lack of a complete set of data in the literature. Inconsistent conclusions between different theories and experiments have complicated the evaluation of the SCIF approach for the various proposed applications. The rest of this chapter is devoted to summarizing and discussing the findings of the past work.

As an aside, we note that devices which rely on virtual cathodes created by accelerated electrons for the primary ion confinement are called EXL-based. The alternative approach (IXL) utilizes a real cathode for ion acceleration and confinement.

3.1 FUSION REACTION RATE EXPERIMENTS

As mentioned earlier, observations of high neutron production rates and odd scaling behavior that could not be explained by simple models generated much of the early interest in SCIF. The initial experiments of an IXL device were performed by Hirsch³, using six ion guns focused through openings in a spherical cathode shell. He found D-T neutron rates approaching 10^{10} n/s, and the D-D neutron rates versus cathode voltage are indicated in Fig. 3-1 for a variety of pressures. For comparison, the energy scaling of the D-D fusion cross section is also included. The observed neutron rate decreased with increasing pressure, increased with beam energy (faster than the energy dependence of $\sigma_{f,DD}$), and scaled linearly with injected ion current. The chordally integrated neutron rate, measured from neutron collimation studies, indicated a peak in the neutron production at the center of the device, and it was later reported that the neutron rate would drop significantly if the ion beams were not properly aligned toward the center^{3,4}.

Recently, gridded cathode systems using a uniform plasma ion source have also observed a linear scaling of the fusion production rate with current. However, R_{fus} increased with pressure up to ~ 1300 mPa, and the voltage scaling just matched the energy dependence of the fusion cross section⁵. Fusion production rate measurements performed in these systems did not approach the performance of Hirsch's work, but they still often exceeded the ideal, collisionless estimate.

Because the injected current was linearly related to the ion density, one would expect a linear dependence of the neutron rate with current from beam-background interactions [or $v_{fus} \sim n_o n_i$ - from the first term in Eq. (2.1)]. The dependence of the neutron rate with beam alignment, however, suggested that beam-beam interactions, which would scale as I^2 , are

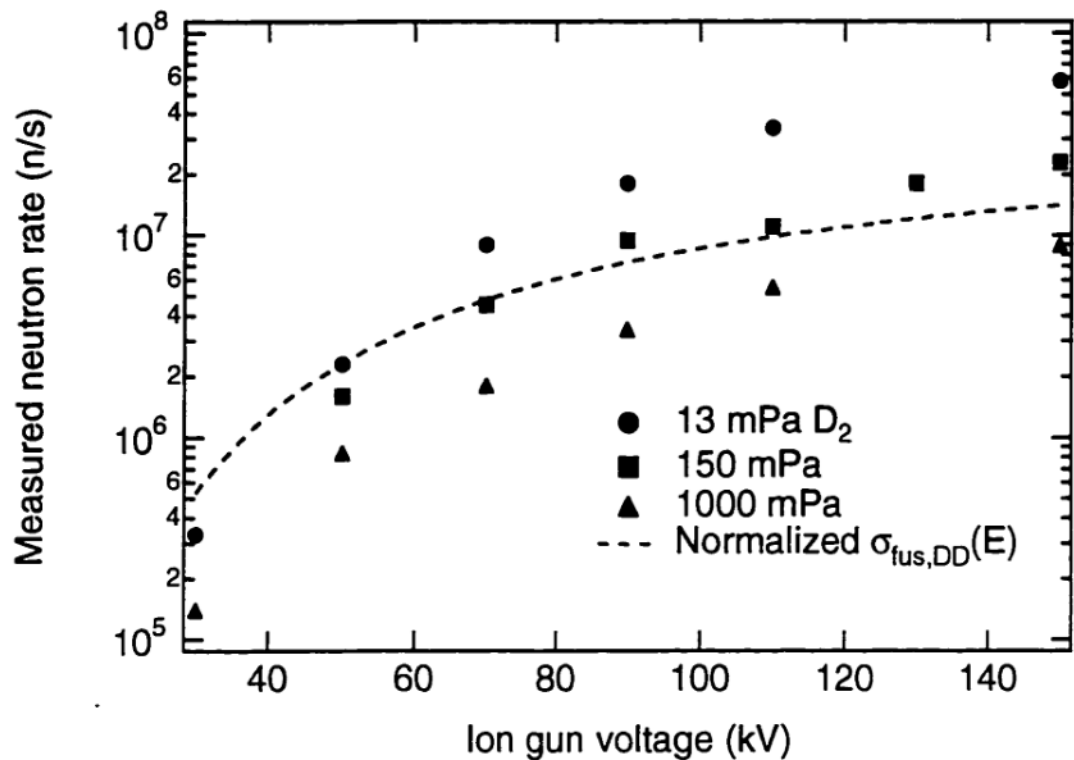


Figure 3-1. Measured neutron rates from Hirsch's ion gun experiment for various pressures of deuterium. Included is the energy scaling of the D-D fusion cross section normalized to the 50 kV data point on the 13 mPa data set³.

dominant. Beam-background neutron rates should also increase with pressure, but that also disagrees with the observed dependence.

The linear current scaling observed is not a surprise, as the beam-background reactivity is greater than the beam-beam (since $n_o \gg n_i$). The cathode voltage scaling observed in Miley's⁵ experiments is also as expected, for the beam-target reactions should scale with the fusion cross section energy dependence [e.g. $R_{fus} \propto \sigma_{fus}(E)$, where $E \approx V_{cat}$].

However, the collisionless flow model underestimates the observed fusion production rate, and it predicts that R_{fus} should increase linearly with the neutral gas density (contrary to Hirsch's observations). Due to these shortcomings of the simple flow model, a variety of hypotheses have been invoked to explain the observed R_{fus} behavior.

3.2 MULTIPLE-WELL HYPOTHESIS

One hypothesis for the enhanced reactivity assumes that the ions are trapped in a virtual cathode structure near the core region. As the ions converge toward the center of the device, their space-charge forms a virtual anode, which is an electrostatic trap for electrons. In the same manner, electrons are thought to converge and form a virtual cathode inside the virtual anode (See Fig. 3-2). It is then suggested that this virtual cathode may trap energetic ions, and since it is perfectly transparent, the ion lifetime in the energetic core region would be longer than expected.

3.2.1 Core density and electrostatic potential distribution models

Models solving Poisson's equation using conservation of energy and angular momentum with various simplifying assumptions have led to many differing conclusions about the form of the SCIF electric potential and ion density distributions.

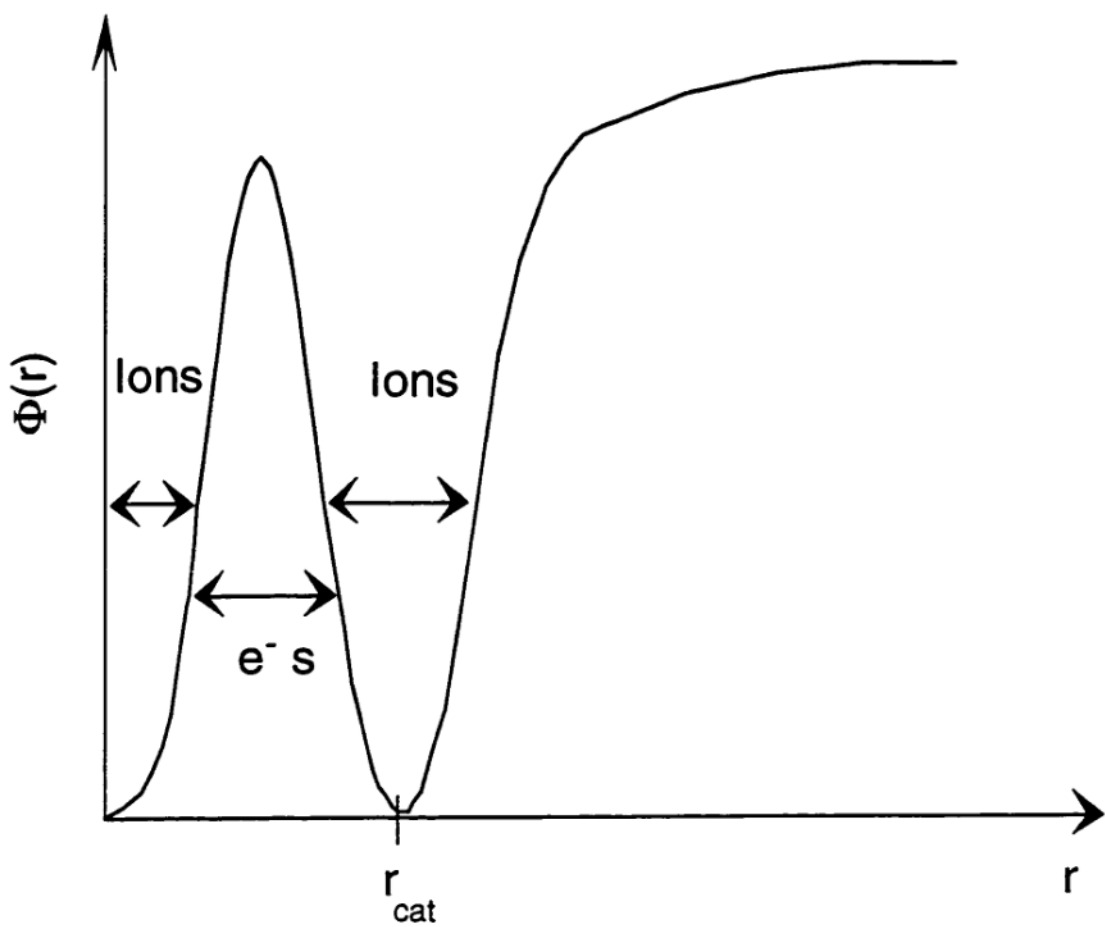


Figure 3-2. Model of a “multiple-well” potential distribution. A virtual anode, formed from the space charge of the converging ions, can trap electrons which can then create a virtual cathode inside the virtual anode in the same manner.

As mentioned in Chapter 2, electrons presumably play an important role in determining the resultant potential and density profiles in the core and plateau regions. In the space-charge-limited flow regime, Langmuir first investigated the effects of bipolar flow in parallel plates. He found the potential profiles depend strongly on the ratio of electron to ion currents ($\Lambda = I_e / I_i \sqrt{m_e / m_i}$), and the ion current limit was also enhanced by a factor of order unity over the single species model shown in Eq. (2.17) (this factor equals 1.865 for $\Lambda = 1$)^{6,7}. A potential profile indicative of a double layer was then expected.

Elmore, Tuck, and Watson¹ later developed the equations for a spherical, bipolar flow in a system where electrons were accelerated inward by a real anode to form a virtual cathode. They found that virtual cathode formation was possible in the center of the inner real anode but questioned the stability of the system at high density.

Hirsch³ solved these equations numerically for an IXL system and found multiple-well solutions, where the potential profile spatially oscillated and formed successive virtual anode and cathode structures (See Fig. 3-2). This also agreed qualitatively with his measured bremsstrahlung emission profiles³. He found multiple-well solutions for varying values of Λ , but the model still assumed purely radial, collisionless flows with a single injection energy³. Note that the potential structures and the enhanced density of core trapped ions were only inferred from the observed bremsstrahlung profiles and not measured directly.

Klevans, *et al.*^{4,8} pointed out that the ion current was assumed to be continuous across the virtual anode in Hirsch's model, but it is the electron current that is continuous there. In fact, most of the ion current would reflect from a virtual anode, and the net effect is that the ion current penetrating the anode is reduced by at least an order of magnitude⁸. A later model added trapped particle effects to Hirsch's equations by first solving Poisson's equation starting from kinetic equations with trapped and flowing particle distribution functions⁴. It

presumed a perfectly symmetric multiple-well structure with a single virtual cathode inside the virtual anode, and the calculations showed that at most 10% of the converging ions would actually leak into the anode region. This is far less than what would be required to generate the neutron production that Hirsch observed. In addition, Klevans, *et al.* argued that the input current of Hirsch's experiments would be too low to support multiple-well structures or a virtual anode formation (Klevans⁴ calculated a 10^{-4} cm anode radius as opposed to the 1.3 cm claimed by Hirsch³).

A single species, cylindrical particle-in-cell (PIC) code, generated by Hockney⁹, also found only about 7% of the ions injected would be inside the virtual anode. He concluded that the ions inside the virtual anode produced enough of a retarding field to reflect the rest of the ion current there. C. W. Barnes¹⁰ later conducted PIC simulations with both electrons and ions in spherical and cylindrical geometries, and he also did not observe enhanced ion densities inside any virtual anode formations.

Up to this point researchers were unsure whether multiple-wells could form, and what effects they may have on the neutron production if they did exist. From the models described above, it appears that virtual electrodes (i.e. an anode for IXL, a cathode for EXL) can be formed in ideal systems with bipolar flow (purely radial flow with a single injection energy), but it remains unclear how to treat the ion density inside a virtual anode.

Dolan and associates^{11,12} first tackled angular momentum and energy spread effects in these models by adding uniform distributions of ion angular momentum and energy at the edge. They found no evidence of multiple-well structures or a complete virtual anode inside the accelerating region for either cylindrical or spherical systems, but a potential hill would form as the combining ion flows converged inside the inner grid as expected. The potential hill height was found to decrease for higher values of Λ because the increased electron current

would presumably neutralize the ions in that region. They also found the plasma density in the core region would decrease for increasing amounts of angular momentum spread due to poorer focusing of the ion flow (which agrees qualitatively with the simple estimates developed in Chapter 2).

However, neutron production rate calculations based on their predicted density and potential distributions were much lower than those which Hirsch observed. They ascribed the discrepancy to the facts that the potential solutions may not be unique, the initial distribution functions (rectangular in their model) may be incorrect, and recirculating currents across a virtual electrode (if one forms) may be discontinuous¹¹.

Dolan's colleagues then continued with this model using Gaussian distribution functions for angular momentum and energy of the injected particles, and they found that small multiple-well structures (but not complete virtual anodes, where $\Phi = 0$) were possible for small variances in the edge distributions functions¹². However, their model of Poisson's equation did not necessarily generate unique solutions; under some circumstances, solutions with and without multiple-wells would be found for identical conditions.

Klevans and Black¹³ later directly studied the effects of collisions on the converging ion flow. Coulomb collisions were neglected because of their small effects on the experiments at that time (too low core plasma density), but charge-exchange and ionization collisions were found to be significant. These neutral collisions would naturally lead to increased angular momentum and a wide spread in ion energies, and hence they modeled the system with a three-group energy distribution (beam, intermediate, and low) and a uniform distribution of angular momentum.

This model varied over a wide range of various parameters including grid transparency and symmetry, grid voltage and current, ratio of electron to ion current (Λ), and neutral

pressure; it did not predict any multiple-well structure or the formation of a complete virtual anode. A potential hill was predicted, and the scaling of the hill height with current, angular momentum (i.e. grid errors and neutral pressure), and Λ agreed qualitatively with the results discussed earlier from Dolan, *et al.*^{11,12}.

In the end, the more complete models (including angular momentum, energy spreads, and collisional effects) of the SCIF system appeared to agree on the formation and behavior of a single potential hill in systems with non-zero angular momentum. However, these models failed to explain the fusion rates and scaling behavior observed by Hirsch.

In the limit that the angular momentum goes to zero, many models predict the formation of a single virtual anode, and in order for the neutron production rate to agree with experimental results, these models need to include some ion density enhancement inside the anode. The multiple-well theory describes a possible mechanism to provide the required density enhancement. Later PIC code simulations and models, however, could not reconstruct this expected density amplification. Hence, it remained uncertain as to how the potential and density distributions manifest themselves inside the mantle region of a SCIF².

3.2.2 Past experimental measurements

Although Hirsch³ was unable to measure the electric potential directly, he inferred the formation of a virtual anode from peaks in the observed bremsstrahlung profile at the radius of 1.3 cm. He then postulated that a virtual cathode could form inside this virtual anode, and that his higher-than-expected neutron performance could be attributed to high recirculating currents of trapped ions between the successive virtual electrodes. Lavrent'ev¹⁴ estimated this current amplification between virtual electrodes to be equal to r_{cat}^2/r^2 , and the neutron production rates predicted from this estimate were within a factor of five of the measured value.

Swanson, *et al.*^{15,16} also deduced the formation of a double-well potential inside their spherical, EXL-based system using lower pressures (1.3 mPa as opposed to 130 mPa) and higher currents (~100 mA as opposed to ~10 mA) from electron beam deflection measurements. However, the observed formations were just small amplitude spatial oscillations in the potential distribution and not deep virtual cathodes and anodes.

In contrast, Black and Robinson found no evidence of potential structures of any kind (not even a potential hill) inside the accelerating region using an electron-beam probe technique^{17,18}. These measurements were conducted for both IXL and EXL based systems at comparable pressures and currents, but the operating voltage used was much lower than what Hirsch utilized (2.5 kV as opposed to 90 kV).

Other experiments inferred the formation of a single potential hill; the anode height increased for higher currents, and its formation depended critically on the amount of current injected¹⁹⁻²². It also appeared that reducing the asymmetries in the accelerating potential, increasing the voltage, and increasing the pressure improved the well depth and core density of the injected particles^{3,11,13,23}.

Electron density measurements from a laser heterodyne system in a pulsed, cylindrical device using neon ions at first did not demonstrate multiple-well formation¹¹. Later experiments performed in deuterium, however, did suggest spatial oscillatory behavior in the electron density, but the amplitude of the electron density variations was roughly 30% and hence insufficient to produce the reactivity enhancement Hirsch invoked^{19,23}. This work was performed for both ion and electron acceleration, and the pulsing of the experiment ($t_{pulse} \approx 20 \mu s$) allowed for much higher input currents (3-8 A for IXL, ~30 A for EXL) at low voltages (2.5 kV typically).

Therefore, some of the above described experiments agreed qualitatively with the theoretical models (i.e. the density increased as the asymmetries or angular momentum of the ions were reduced), but others found conflicting behavior (i.e. Black and Robinson¹⁷ found no evidence of any potential structures inside the accelerating grids while Swanson, *et al.*^{15,16} found many cases of multiple-well structures). Evidence supporting oscillatory behavior in the density and potential distributions appeared to be in conflict with many of the more complete theoretical models described above.

3.3 CHARGE-EXCHANGE MODEL

Hirsch initially proposed that charge-exchange and ionization effects were degrading the injected ion beam at higher pressures, for fast ions are then being replaced by colder ions³. These effects may, in part, explain the dependence of the observed neutron rate on cathode voltage as well, for the cross section for neutral particle interactions decreases at the higher ion energies^{24,25}.

A model of Hirsch's experiment that included the effects of charge-exchange on the ion guns was produced by Baxter and Stuart²⁶. It predicted neutron rates and scalings with voltage, current, and pressure comparable to Hirsch's observations, but to achieve agreement, the pressures used in the model were a factor of 20 or more higher than what Hirsch reported^{3,26,27}. However, the effects of recirculating ion current were ignored in the model, and it was shown experimentally that critical ion beam alignment, presumably to allow such recirculating currents, was necessary to achieve the highest neutron production rates^{3,4}.

One would naively expect the system fusion reaction rate to be reduced because of charge-exchange, for the cold ions left behind are far-less fusible. However for some experiments, the fast-neutral path length is as long or longer than the confined ion orbit

length. Indeed, in the glow discharge regimes studied by Miley, *et al.*^{5,21,22}, the ions do not recirculate but rather charge-exchange on the first pass through the cathode. Therefore, a more complete model, accounting for both charge-exchange and the population of recirculating ions, is necessary to describe the fusion reactivity in a SCIF device.

3.4 CONCLUSIONS AND WISCIF EXPERIMENTAL RELEVANCE

It is not clear if SCIF systems can support multiple-well structures or what kind of density or reactivity enhancement they may provide. There is much evidence and theoretical support for a virtual hill formation, and some experiments have established the qualitative behavior of that potential hill (i.e. hill height increases with increased current and decreased angular momentum). However, some experiments have seen little or no potential structure while others have seen multiple-well formations, and hence it is difficult to evaluate the SCIF concept and predict its scaling for higher fusion reaction rate applications based on these conflicting models and experimental results.

The fusion reaction rate of a gridded system is mainly limited by the power and stress loading on the grids and transparency requirements. Therefore, much of the past work stopped in the mid 1970's presumably due to the understanding that gridded systems could not become useful power amplifying devices (i.e. $Q > 1$, where Q is the ratio of fusion power out to fusion power in) without anomalous ion trapping effects^{2,28}.

To circumvent these losses to the grid, alternative concepts based on the EXL approach have been promoted and have revived recent interest in SCIF-type devices. The Polywell™ utilizes high energy electron beams that are confined with an external polyhedral cusp magnetic field²⁹⁻³¹. The electron Penning trap uses a uniform magnetic field passing through an electric quadrupole field that produces, in the rotating frame of the gyrating

electrons, a spherical potential well³². In both cases, the electrons are focused toward the center to form a virtual cathode to accelerate and confine the fuel ions.

These devices avoid the grid problems, but concerns over high- β confinement and equilibrium ($\beta \approx 1$), symmetry of the electron and potential distributions, electron losses, and Coulomb collisional effects are additional difficulties^{33,34}. Some suggest that these gridless systems could possibly become a low-Q fusion-power amplifier, but only if the high edge ion density required could be provided and the above-listed problems are not catastrophic^{28-30,32}.

To resolve some of the ambiguities which have arisen from these past experiments and models, the WISCIF experiments are designed to evaluate physics issues that are common to all SCIF devices (IXL or EXL-based). These issues include the ion flow convergence dynamics and current and voltage scaling, asymmetry constraints in the accelerating potentials, and the electrostatic potential profile structure in the presence of the convergent flow. These issues can all be addressed in an inexpensive, gridded IXL device with appropriate diagnostic support.

Whether or not SCIF-type devices can be developed into application-relevant sources also requires more insight into the origin of the fusion reactivity. Experiments were thus designed to identify the reactivity source and understand the systematic behavior of these systems at higher densities and cathode powers than previously studied. The results from these experiments are included in Chapter 6, where comparisons with a charge-exchange model that accounts for the recirculating ion contribution is included.

3.5 REFERENCES

- ¹W. C. Elmore, J. L. Tuck, and K. M. Watson, Phys. Fluids **2**, 239 (1959).
- ²T. J. Dolan, Plasma Phys. Controlled Fusion **36**, 1539 (1994).
- ³R. Hirsch, J. Appl. Phys. **38**, 4522 (1967).
- ⁴K. M. Hu and E. H. Klevans, Phys. Fluids **17**, 227 (1974).
- ⁵G. H. Miley, J. Nadler, T. Hochberg, Y. Gu, O. Barnouin, J. Lovberg, Fusion Technol. **19**, 840 (1991).
- ⁶I. Langmuir, Phys. Rev. **33**, 976 (1929).
- ⁷T. A. Forrester, *Large Ion Beams*, John Wiley & Sons, New York (1988).
- ⁸G. D. Porter and E. H. Klevans, Phys. Fluids **14**, 428 (1971).
- ⁹R. W. Hockney, J. Appl. Phys. **39**, 4166 (1968).
- ¹⁰C. W. Barnes, Ann. NY Acad. Sci. **251**, 370 (1975).
- ¹¹T. J. Dolan, J. T. Verheyen, D. J. Meeker, and B. E. Cherrington, Jour. Appl. Phys. **43**, 1590 (1972).
- ¹²B. E. Cherrington, J. T. Verheyen, and D. A. Swanson, Ann. NY Acad. Sci. **251**, 139 (1975).
- ¹³W. M. Black and E. H. Klevans, J. Appl. Phys. **45**, 2502 (1974).
- ¹⁴O. A. Lavrent'ev, Ann. NY Acad. Sci. **251**, 152 (1975).
- ¹⁵D. A. Swanson, B. E. Cherrington, and J. T. Verheyen, App. Phys. Lett., **23**, 125 (1971).
- ¹⁶D. A. Swanson, B. E. Cherrington, and J. T. Verheyen, Phys. Fluids **16**, 1939 (1973).
- ¹⁷W. M. Black and J. W. Robinson, J. Appl. Phys. **45**, 2497 (1974).
- ¹⁸C. H. Stallings, J. Appl. Phys. **42**, 2831 (1971).
- ¹⁹Verheyen, J. T., B. E. Cherrington, D. A. Swanson, and D. J. Meeker, Ann. NY Acad. Sci. **251**, 126 (1975).
- ²⁰R. L. Hirsch, Phys. Fluids **11**, 2486 (1968).
- ²¹J. H. Nadler, , G. H. Miley, Y. Gu, and T. Hochberg, Fus. Tech. **21**, 4140 (1992).

- ²²J. H. Nadler, Y. Gu, and G. H. Miley, Rev. Sci. Instrum. **63**, 4810 (1992).
- ²³D. J. Meeker, J. T. Verheyen, and B. E. Cherrington, J. Appl. Phys. **44**, 5347 (1973).
- ²⁴R. L. Freeman and E. M. Jones, Culham Laboratory Report #CLM-R137 (1974).
- ²⁵R. K. Janev, W. D. Langer, K. Evans, Jr., and D. E. Post, Jr., *Elementary processes in Hydrogen - Helium Plasmas*. (Springer-Verlag, Berlin, 1987).
- ²⁶D. C. Baxter and G. W. Stuart, J. Appl. Phys. **53**, 4597 (1982).
- ²⁷R. L. Hirsch and G. A. Meeks, Rev. Sci. Instrum. **38**, 621 (1967).
- ²⁸T. Rider, M.S. Thesis, Massachusetts Institute of Technology, 1994.
- ²⁹R. W. Bussard, Fusion Technol. **19**, 273 (1991).
- ³⁰N. A. Krall, Fusion Technol. **22**, 42 (1992).
- ³¹R. W. Bussard, U. S. Patent # 4826646 (1989).
- ³²D.C. Barnes, R. A. Nebel, and L. Turner, Phys. Fluids B **5**, 3227 (1993).
- ³³W. M. Nevins, Phys. Plasmas **2**, 3804 (1995).
- ³⁴T. H. Rider, Phys. Plasmas **2**, 1853 (1995).

Chapter 4. The WISCIF Apparatus

To experimentally explore the basic physics and provide critical tests of theoretical models of SCIF systems, a simple, inexpensive device for production of a convergent flow of ions was constructed. Components of the apparatus were provided mainly from surplus equipment from experiments here at the UW, capitalized equipment provided by the College of Engineering, or from instrumentation given to the University by Directed Technologies Incorporated (DTI) from their decommissioned Polywell™ device. The experimental facility is based on the gridded IXL approach, and although the Polywell™ and the gridded systems were quite different in operation, the vacuum equipment and power supplies were quickly utilized for the present apparatus.

The WISCIF facility uses a 0.45 m radius, 0.7 m tall aluminum vacuum vessel to house three concentric, spherical globes (See Fig. 4-1). The outer two grids are used to produce a mild electron trap, in which a low-temperature plasma is created for a source of ions. These ions are then accelerated by the innermost, high-voltage cathode globe, and the result is a spherically converging flow of ions.

The remainder of this chapter describes the details and construction of various components of the WISCIF experiment. These include the vacuum system, the gridded electrodes, the edge plasma source, the assorted power supplies, and the diagnostics used in this investigation.

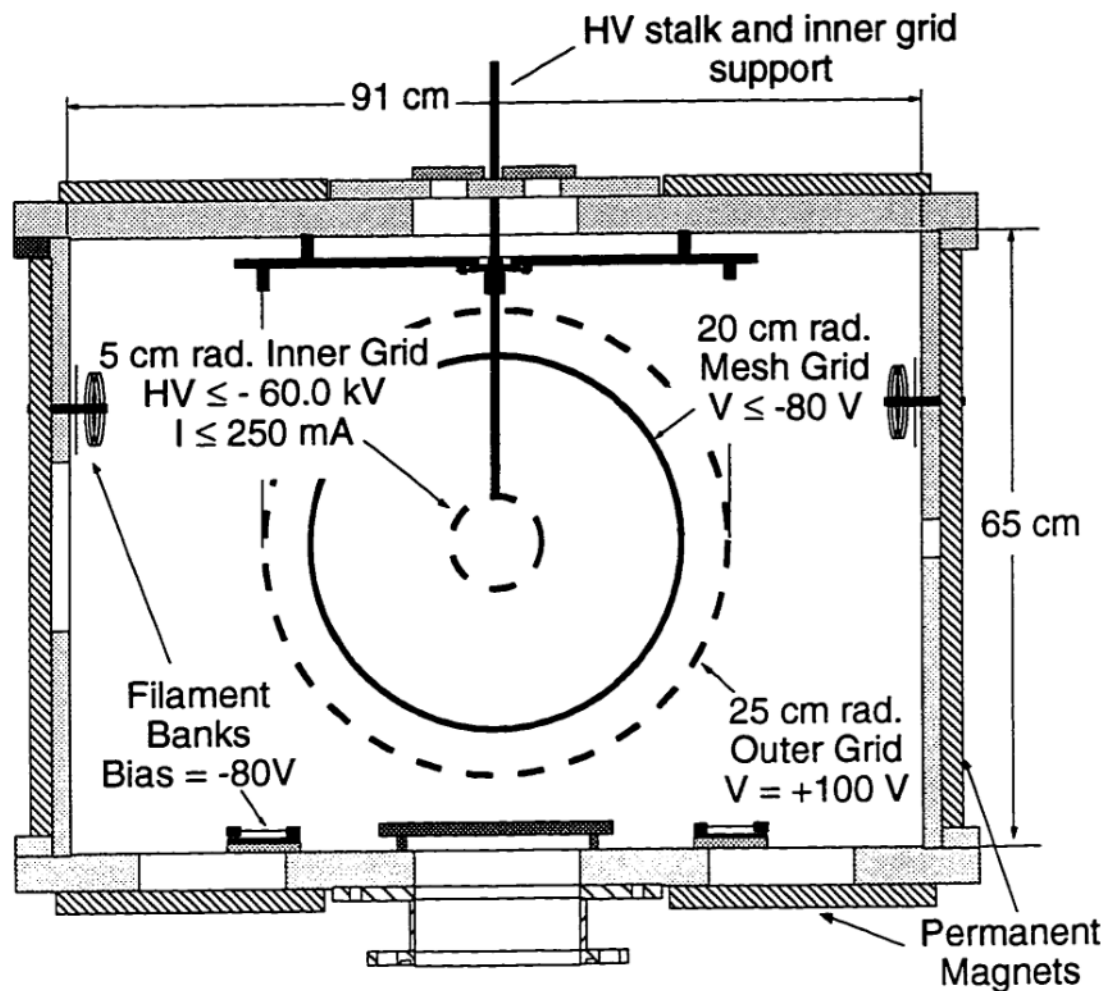


Figure 4-1. Schematic (side view) of the WISCIIF device including typical operating voltages

4.1 VACUUM SYSTEM AND NEUTRAL GAS CONTROL

As in other plasma experiments, impurities were a concern, and therefore, a clean vacuum environment is desired. A 450 l/s Leybold-Heraeus Turbotronik NT 450 turbomolecular pumping system produces base pressures of less than 0.04 mPa to be readily achieved inside the viton O-ring sealed chamber. This system includes a 83 l/s Welch model 1397 mechanical pump to bring the chamber down from atmosphere to less than 13 Pa, where it then acts as the forepump for the turbomolecular pump.

Pressure (P) measurements are made with a variety of devices, including an ionization gauge for $P < 130$ mPa, thermocouple and convectron gauges for $130 \text{ mPa} < P < 130 \text{ Pa}$, and a capacitive manometer for chamber pressures greater than 130 Pa. The gauges were calibrated against a high-sensitivity capacitive manometer for pressures below 1.3 Pa. For protection of the pumping systems, the various gauge measurements were interlocked with air-powered valves using gauge monitors and controllers. The switching, control, and pumping components of the vacuum system are physically located underneath the chamber.

Careful control of the fill gas pressure is crucial for consistent results. Gas cylinders are connected with poly-flow tubing directly to a needle valve assembly for fill-gas feed and pressure control. A butterfly valve located just above the gate valve is also utilized to limit the gas flow through the system and to provide further fine pressure control.

Windows are installed in various places for visual observations during operation. Radiological measurements of X-rays showed dose rates of 1 to 2 mrem/hr for cathode voltages greater than 21 kV through the regular glass windows. In order to attenuate this radiation, the windows are replaced with thick leaded glass or aluminum plates for the higher-voltage operation.

4.2 GRIDDED ELECTRODE DESIGN AND CATHODE MOUNT

The cylindrical vessel is arranged with the ends placed horizontally, which facilitates diagnostic access to the device midplane. The grids are mounted to the top of the device, and this top is readily opened with a hydraulic lift after the machine has been vented to atmosphere. The outer grids are attached by four threaded rods, which are electrically isolated with ceramic stand-offs on each rod. The grids are biased via kapton-coated wire connections to an electrical feedthrough mounted in the lid.

The inner sphere hangs from a special ceramic stalk structure, which is held in place by a 1/2" Cajon fitting atop a 100 kV isolation feedthrough (See Fig. 4-2). This independent attachment allows the inner globe to be raised, lowered, and rotated with respect to the fixed outer grids and chamber walls. This provides external alignment of the cathode and further experimental flexibility (even under vacuum).

Special attention is required for the construction of the inner globe stalk support, for not only is structural integrity important, but also the electrostatic stresses that are imparted to the stalk must be minimized. Concentric tubes of alumina and quartz were selected for the bulk stalk materials for their rigidity and high voltage insulation properties. These ceramics are cut to size from stock using a diamond-bladed saw, and they are sealed together using ceramic cement and Torr-seal vacuum epoxy. The vacuum end of the stalk is also rounded using diamond files in order to minimize the electric stresses in that region. The inner grids are tack-welded to rounded screws which then thread into the end of the stainless-steel center tube.

The globes are assembled from wire rings, which form the latitudes and longitudes that make up the sphere. The longitudes and the equator are all rings of the same diameter, and the diameters of the latitudes are chosen so that each open region between grid wires has approximately the same area. The rings are constructed by placing pieces of wire in an

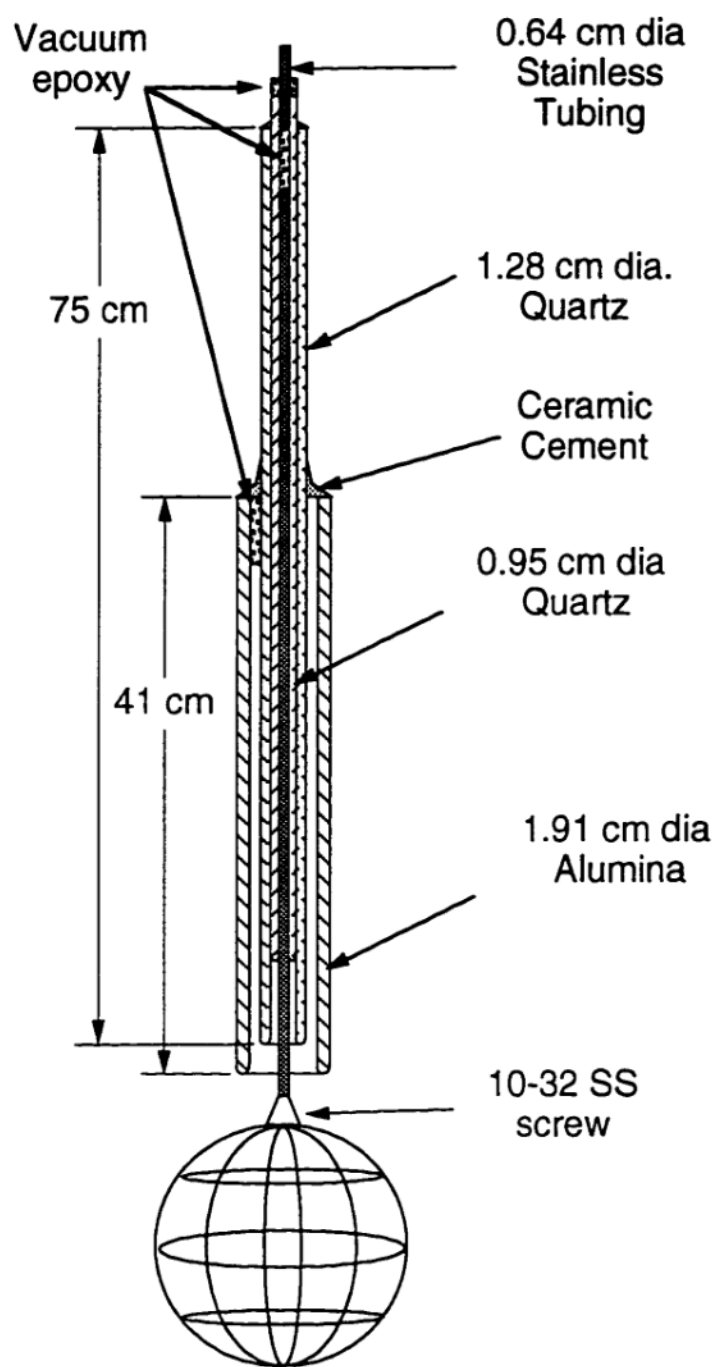


Figure 4-2. Side view of the high-voltage cathode support assembly (not to scale).

aluminum circular form and spot-welding the ends together. These hoops are then placed together in the spherical shape and tack-welded together at the intersections of the latitudes and longitudes. Forms for spheres of 0.1, 0.25, 0.2, 0.4, and 0.5 m diameters are available, and the number of rings used in the sphere basically determine the cathode's symmetry and transparency. These grids are generally constructed from stainless steel, but other materials that were used include titanium and tungsten. Titanium spot-welds readily, but thin nickel film (0.1 mm) is needed between the welds for the tungsten cathodes.

The outer globe diameter of 0.5 m was chosen so that the available volume inside the chamber could be used effectively, and the initial inner grid size of 0.1 m diameter was selected because of its similar size to those used in previous experiments¹⁻⁴. Cathodes as little as 0.05 m diameter can be constructed using the above described method. However, limitations due to the spring tension of the wires start to seriously compromise the strength of the tack-welds and the symmetry of the sphere at smaller sizes.

4.3 EDGE PLASMA SOURCE

An extended plasma, formed about the outer grids, provides an ion source localized at large radii (See Fig. 4-3). Hot tungsten filaments (0.01 cm diameter, 5 cm long, biased at -80 V) generate the primary electrons which accelerate towards the positively biased outer grid (+100 V) to collisionally ionize the background gas (H_2 or D_2). The negatively biased middle grid (-80 V) shield these primary electrons away from the flow region and localize the edge plasma to radii greater than 20 cm. A fine mesh with a spacing (0.04 cm) less than the local electron Debye length (~ 0.1 cm) is placed on this grid to provide an electrostatic barrier for the electrons, and permanent magnets are arranged around the outer wall to enhance the primary electron lifetime. The innermost cathode grid ($r_{cat} = 2.5 - 10$ cm) provides the deep, accelerating potential well (5 - 65 kV) for the ion flow. The

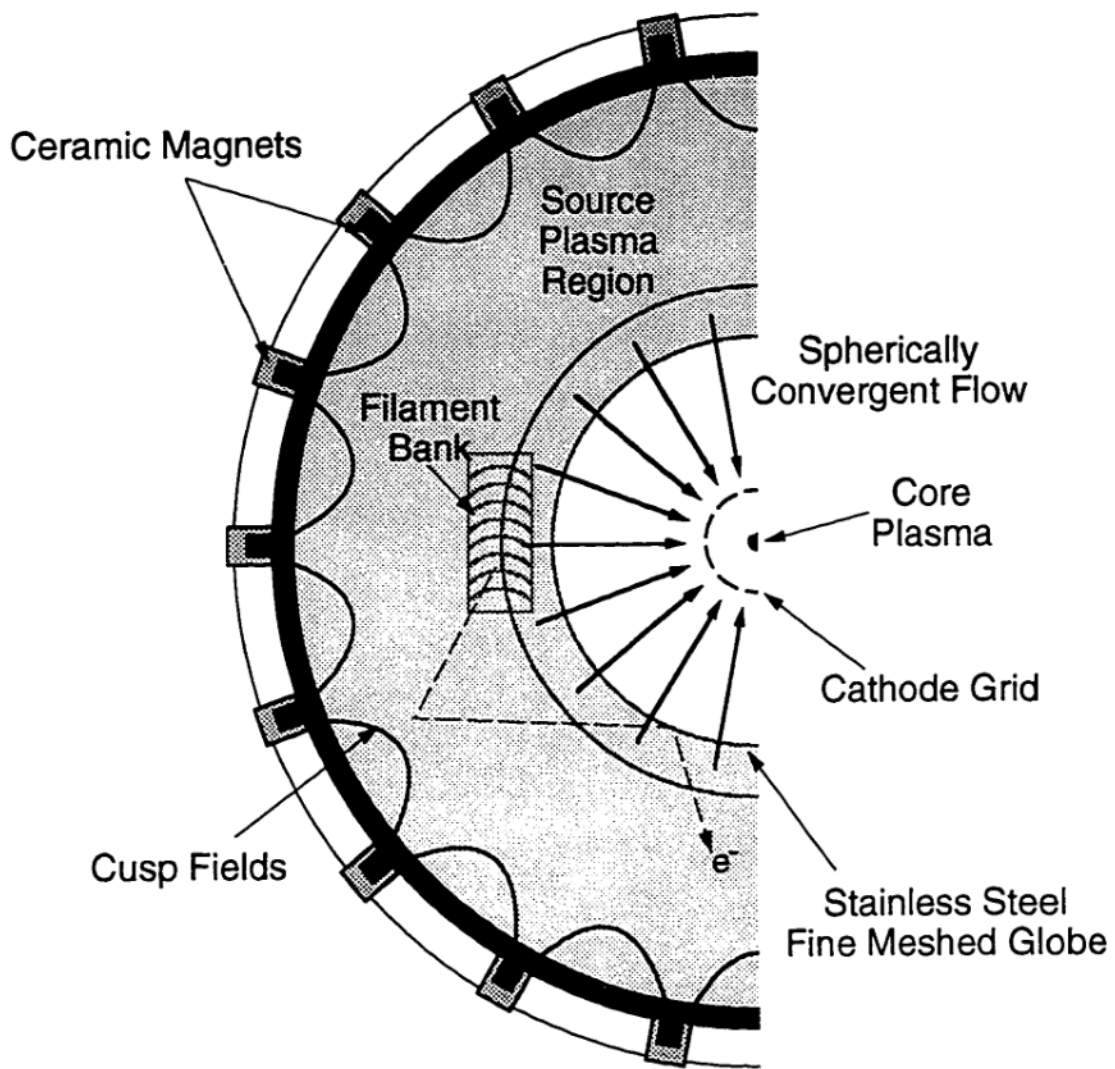


Figure 4-3. Schematic of the edge ion source, depicted by the shaded region.

collected cathode current is controlled by varying the edge plasma density with the primary electron source. Ion flows were generated and sustained in this manner for pressures as low as 2.7 mPa in hydrogen.

4.4 POWER SUPPLY SYSTEMS

Various power systems are necessary for plasma generation and ion acceleration for this device (See Figs. 4-1 and 4-3), and typical voltages and currents supplied during operation are listed in Table 4-1. Two Sorensen DCR80-5.0A 200 watt power supplies provide the outer grid (V_{og}) and the filament bank (V_{bank}) biases, and Kepco model JQE supplies and a Sorensen 40-115 are used to supply the filament current. Initially, the inner grid voltage (V_{cat}) was supplied by a 2.5 kW Hipotronics 25-100 ($V_{max} = 25$ kV, $I_{max} = 100$ mA), but it was later upgraded with a 25 kW ORAM Model UW-75-330 ($V_{max} = 75$ kV, $I_{max} = 330$ mA) for the fusion reactivity experiments.

Inner Grid Bias (kV)	Inner Grid Current (mA)	Outer Grid Bias (V)	Filament/Mantle Grid Bias (V)	Filament Current (A / filament)
(-) 5.0 - 60.0	10 - 300	(+) 70 - 100	(-) 40 - 80	1.9 - 2.2

Table 4-1. Typical voltage and current settings for the WISCIF device. Biases are listed with respect to the vacuum vessel wall (ground).

Operating conditions are monitored mainly with the various power supply indicators and a calibrated ionization gauge or convectron gauge controller for chamber pressure.

4.5 DIAGNOSTICS

Figure 4-4 includes the layout of the plasma and nuclear counting diagnostics that characterized the SCIF device. These include Langmuir, double, and emissive probes, a spectrally filtered CCD (charge-coupled device) television camera, a long neutron detector, and a collimated surface-barrier diode. The use and analysis of these various diagnostics are discussed below.

4.5.1 *Electrostatic probes*

Measurements of the edge plasma density and electron temperature are provided by a standard 1/4" Langmuir disk-probe⁵. It is mounted on a mid-plane port with a Cajon-assembly which allow the probe to be fully retracted from the vessel. Measurements of the current-voltage (I-V) characteristics of the edge plasma are made using a transistor curve tracer or by manually adjusting the bias and recording the results on a X-Y plotter.

For characterization of the energetic ion flow, high-voltage probes, designed to stand off the large electrostatic potentials and withstand the energetic ion bombardment in this region, are employed. Construction of these probes is similar to the inner grid stalk, and details can be found in the double-probe schematic shown in Fig. 4-5. Instead of a stainless steel conductor, the probe tips are made from tungsten, and these tips are then silver-soldered to kapton-coated copper wire. These copper wires are fed through the alumina and Pyrex, where they connect to 40 kV insulated leads. The alumina-Pyrex structure is sealed to a stainless steel sheath via a 1/2" Cajon fitting, and this sheath can be moved radially through a 7/8" Cajon seal.

The double probe floats and hence collects no net current from the plasma, but by applying a bias across the probe tips, a current can flow between the tips⁵. This is achieved

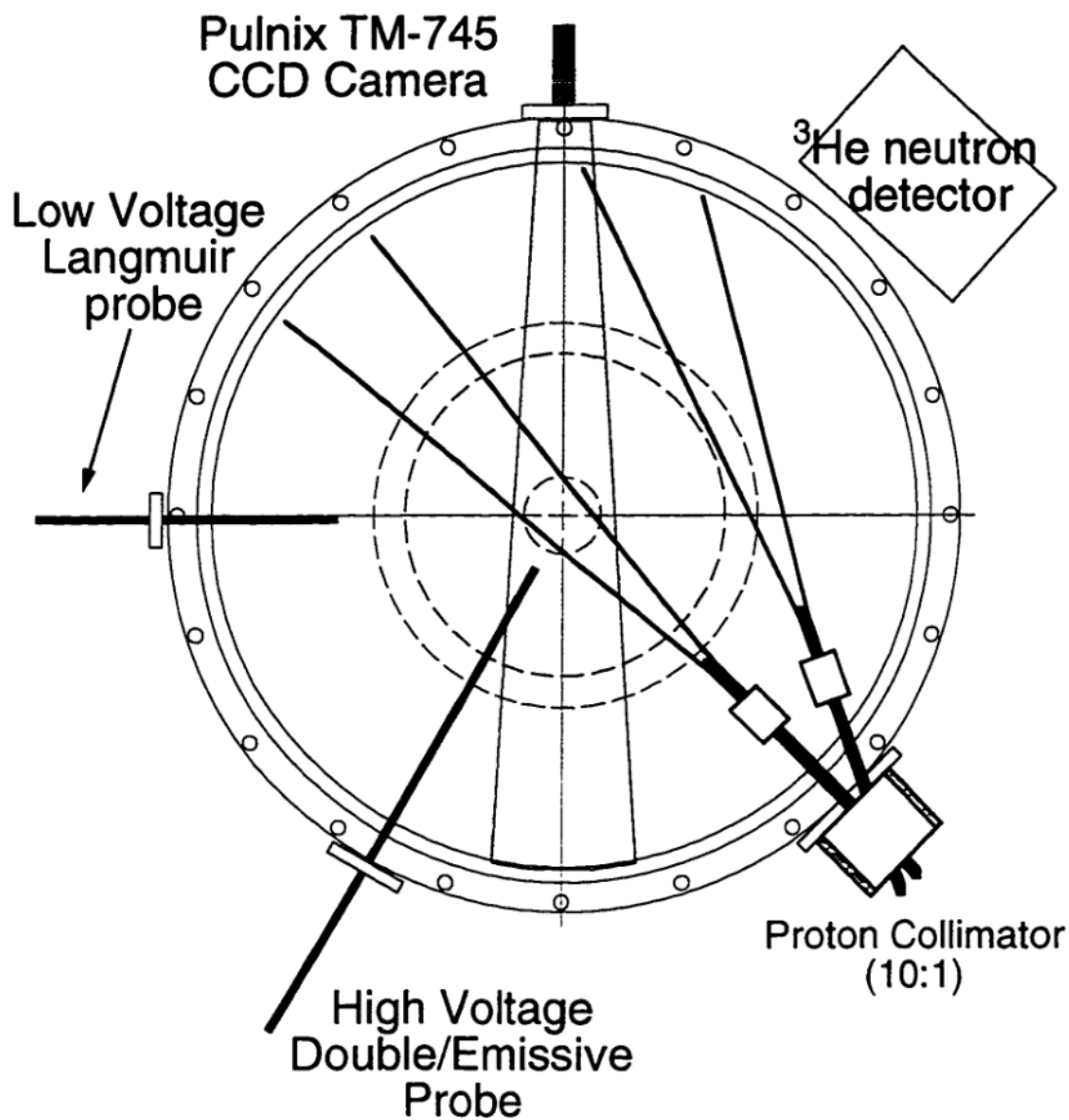


Figure 4-4. Diagnostic layout of the WISCIF device (top view) including sightlines for the camera and proton collimator.

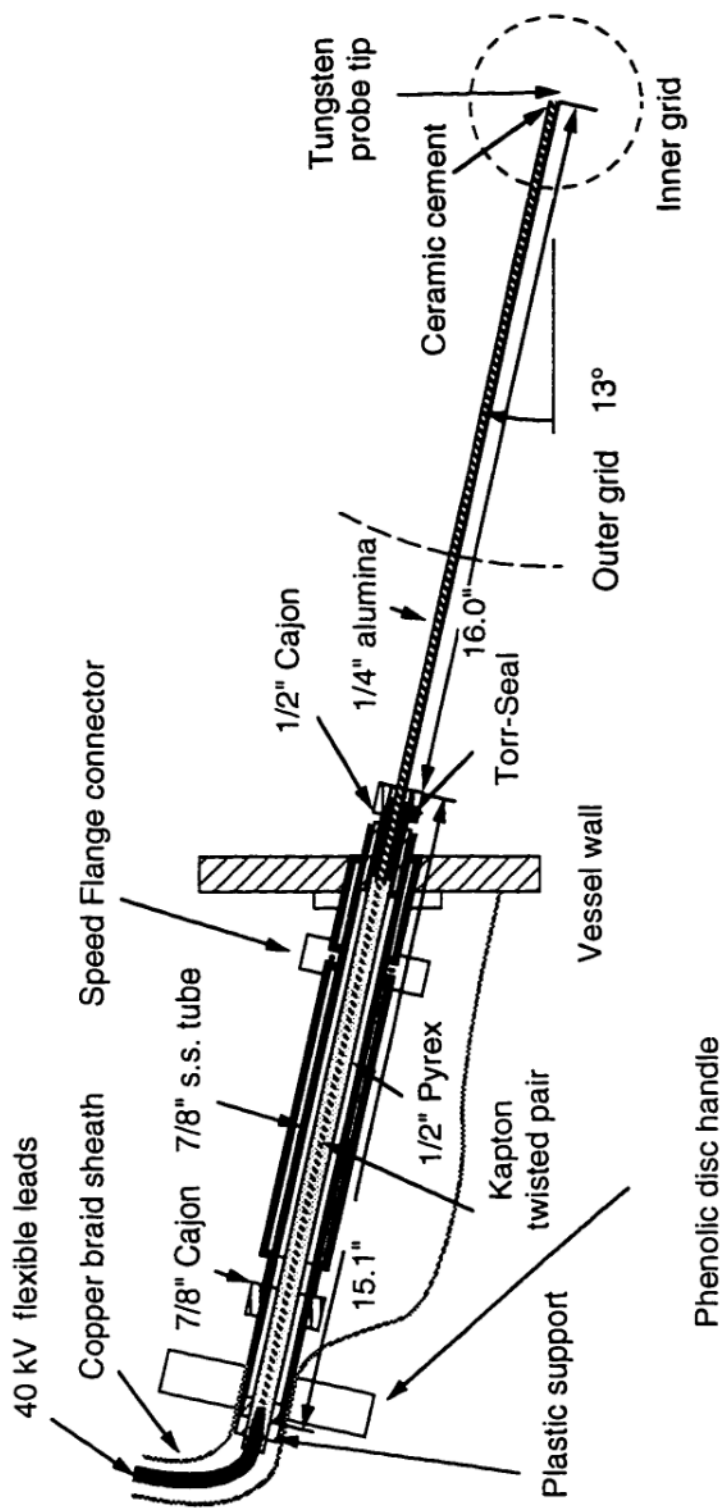


Figure 4-5. Probe schematic for the high-voltage double or emissive probes

by floating a power supply with an isolation transformer, and further details of the biasing circuit is included in Fig. 4-6(a). By measuring the I-V characteristics of the double probe [See Fig. 4-7(a)], ion density and velocity distribution information in the core region is obtained (See Appendix 2).

Shadowing of the recirculating ion flow by the radial alumina probe shaft leads to an underestimation of the ion density, and the measured saturation current, i_{sat} , is therefore corrected by the recirculation factor, ξ [from Eq. (2.13)], to account for the shadowing effect and provide an upper limit for the ion density from these measurements. Assuming the total ion current ($I_i = en_i v_i A_p$) equals the saturation current, the ion density is then given by:

$$n_i = \frac{\xi i_{sat}}{eA_p} \sqrt{\frac{M}{2q\Phi_p}} \quad (4.1)$$

where A_p is the probe area ($= 5.9 \times 10^{-6} \text{ m}^2$).

For the emissive probe, a similar stand-off design is used, but the probe tips are set off the body to better measure the recycling part of the ion flow. The tip consists of a 0.3 mm tungsten wire that is spot-welded to stainless steel plugs, which are connected to the copper leads in the stand-off. The heating current for the tungsten wire is provided directly off the isolation transformer and manually controlled with a variac. The filament bias is computer controlled with a 5.0 kV programmable power supply, and the emission current signal is measured through an optically isolated amplifier [See Fig. 4-6(b)].

By measuring the emission current versus the probe bias, the floating and plasma potentials are directly observed as shown in Fig. 4-7(b). The radial profile of the plasma potential is obtained by moving the probe through the 7/8" Cajon fitting, and the potential asymmetries of the potential well are also characterized by rotating the cathode grid in front of the fixed probe.

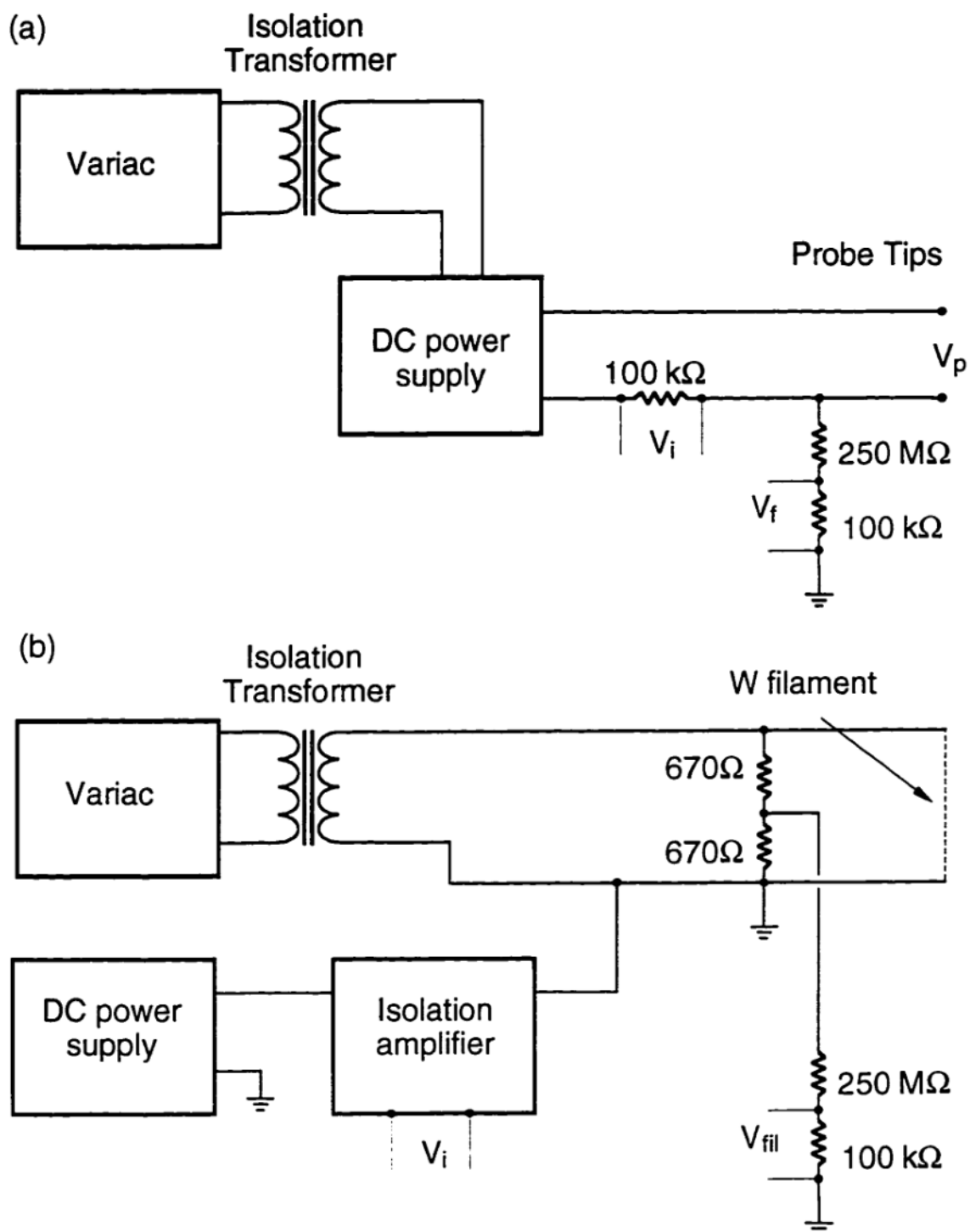


Figure 4-6. Probe bias circuit diagrams for (a) the double probe and (b) the emissive probe.

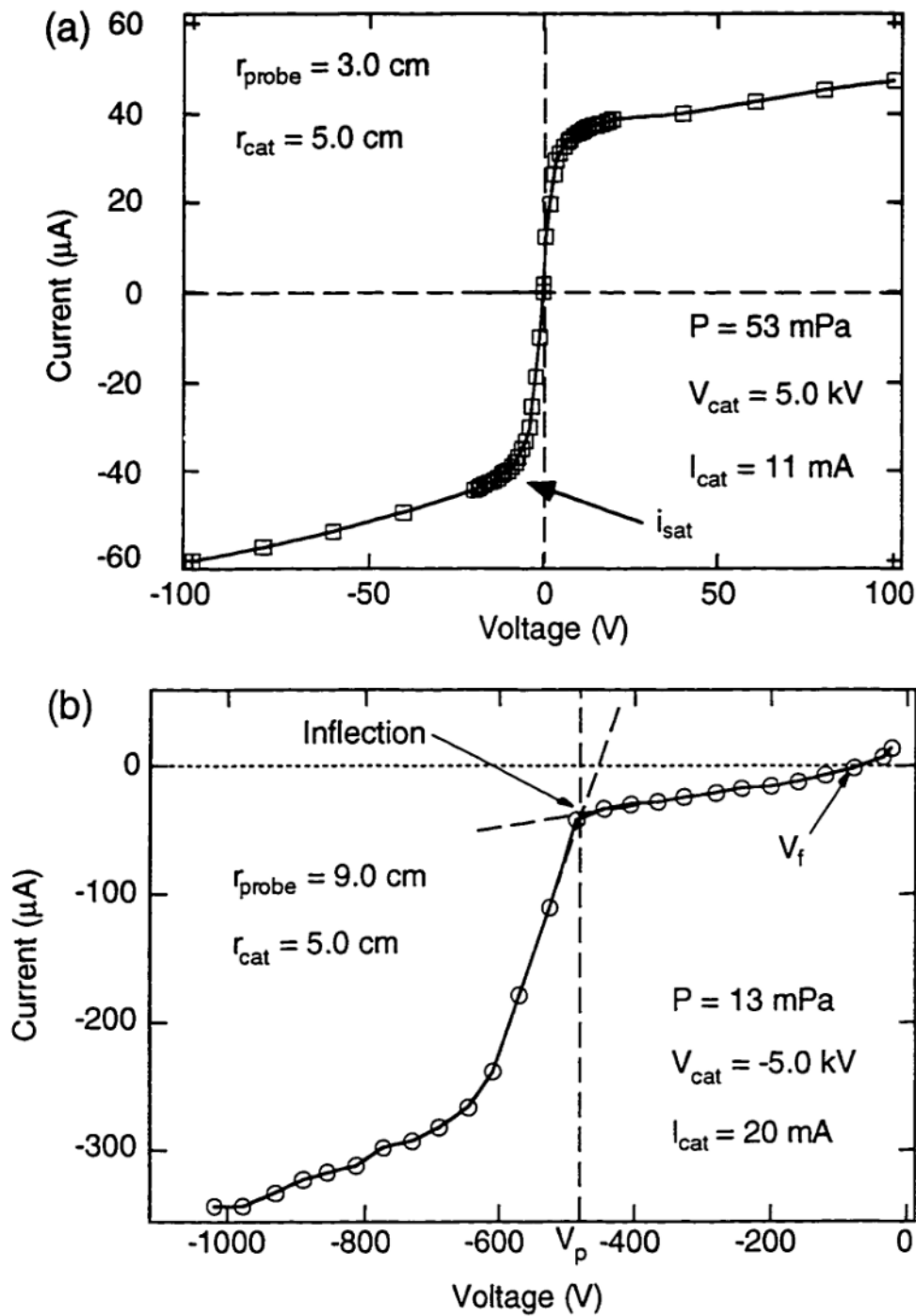


Figure 4-7. Sample IV characteristics of (a) the double probe and (b) the emissive probe. The ion saturation current (i_{sat}) is indicated in (a), and the floating (V_f) and plasma (V_p) potentials (from the inflection method⁵) are indicated in (b).

These probe designs work well as long as some restrictions on the operation of the device are followed. For cathode voltages of 10 kV or more ($I_{cat} \geq 40$ mA), the probe glows white-hot when placed in the center due to the power deposited on the probe from ion bombardment. Therefore, to avoid thermal destruction of the probe, operational conditions were limited to cathode potentials of 10 kV or less. Also, the lifetime of the probe is limited by the amount of cathode material which sputters onto the probe. The embedded stainless steel provides a short circuit directly between the double probe tips, and it also drastically reduces the probe's voltage stand-off capability. The emissive probe measurements are further limited to 5 kV by the biasing power supply capability, and ion flows only up to 40 mA could be studied without destroying the thin filament.

The perturbation of the ion flow by the probe is a concern using this invasive diagnostic technique, but no appreciable change in the discharge characteristics (*i.e.* cathode voltage, current, or visible core size) was observed during the measurements. In order to minimize the disturbance of the ion flow, the probe tips intercept $\leq 10\%$ of the ion core surface area.

4.5.2 CCD camera

A tightly focused, converged-core is readily evident near the origin of the high-voltage cathode (See Fig. 4-8). The size and brightness of this high-energy core vary considerably with experimental parameters (*i.e.* cathode voltage, current, and neutral pressure), but its existence is generally robust in that it is readily attained and persists stably.

Images of this visible emission are acquired with a Pulnix TM-745 CCD camera. The standard TV signals (RS-170) are then digitized using a Dipix P360F 4MB frame

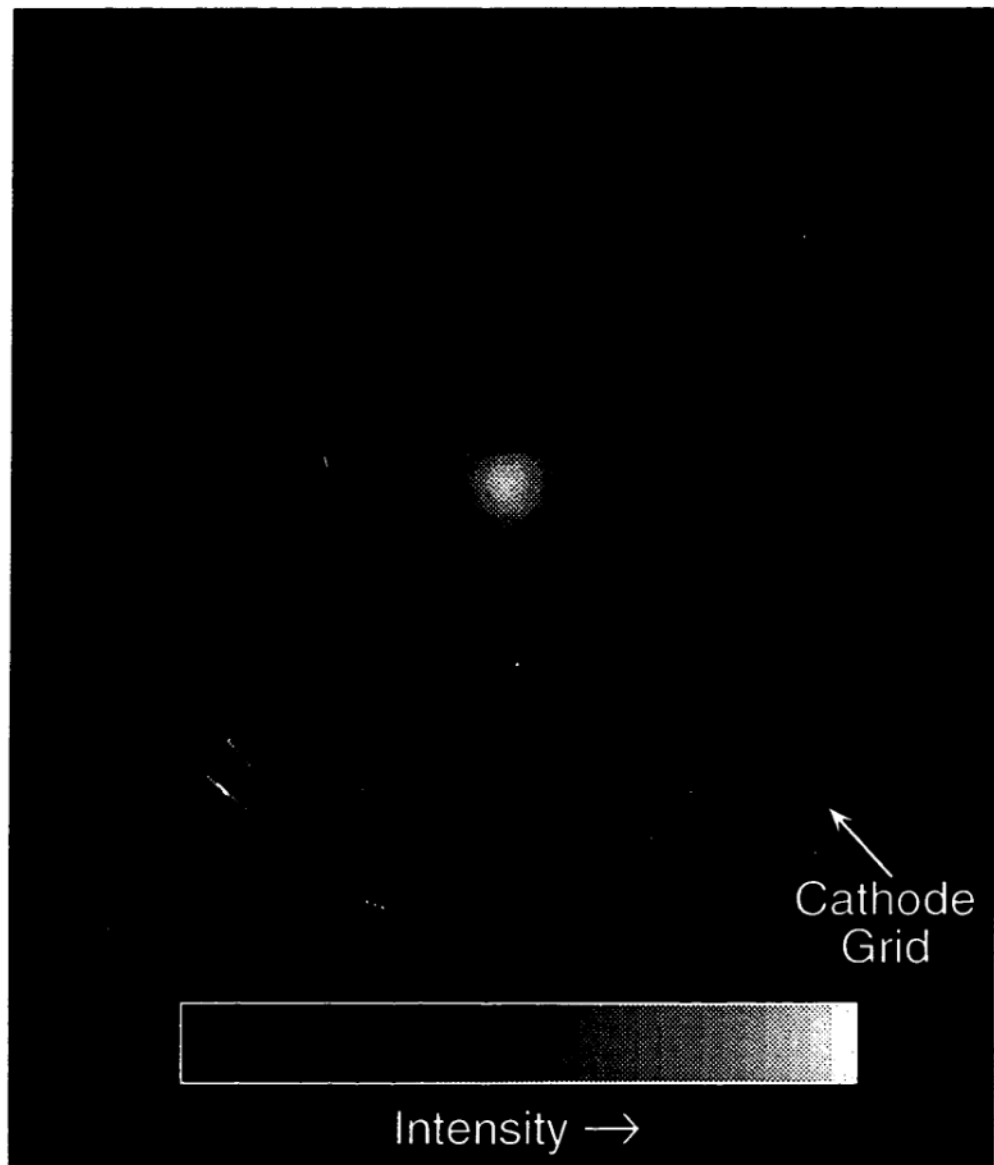


Figure 4-8. A CCD camera image of the H_{α} emission for a 17 kV, 80 mA “converged core” mode showing a 0.6 cm radius core. The grid shown is a 5.0 cm radius cathode grid with a 15° poloidal grid spacing.

grabber card (PC) or a Scion LG-3 board (Macintosh) installed on a local computer. The camera employs a 25 mm lens which is focused on the center of the inner globe, and in order to improve contrast, spectral filters for H_{α} ($\lambda = 656.3$ nm) emission are utilized. Background light from the source plasma filaments and from the cathode grid itself are also present in the video of the plasma, and contrast is further improved by subtracting frames of this background from the plasma data.

The core size estimates are derived from the half-width at half-maximum (HWHM) of the intensity distribution recorded by the CCD camera system. To derive the real core size, an Abel inversion of the measured intensity profile is required to obtain the ion spatial distribution⁶:

$$A(r) = \frac{1}{\pi} \int_r^R \frac{dI}{dx} \frac{dx}{\sqrt{x^2 - r^2}} \quad (4.2)$$

where $A(r)$ is the inferred radial density distribution for a particular chordally-integrated intensity profile, $I(x)$, and x is the chordal height from the origin.

To estimate the difference between the HWHM of $I(x)$ and the core size given by $A(r)$, sample $A(r)$ profiles and the inverse of Eq. (4.2) can be used to get the resulting $I(x)$ profile. The HWHM of $I(x)$ can then be compared to the predetermined core size from the sample $A(r)$ profile.

Assuming that the intensity is directly proportional to the local ion density, estimates of the $A(r)$ profile is given by the simple ion density distribution models discussed in Section 2.2 [See Eqs. (2.3) and (2.11)]. The intensity profile is then calculated from the inverse of Eq. (4.2) or:

$$I(x) = 2 \int_x^R \frac{A(r)r dr}{\sqrt{r^2 - x^2}} \quad (4.3)$$

The resulting $I(x)$ profiles from the simple models are shown in Fig. 4-9, and the HWHM values agree with the model core size ($r_c = 1.5 r_o$) within 7%. Hence, the HWHM of the measured intensity distributions can be used directly to approximate the real core size. Again, the intensity profiles shown in Fig. 4-9 are calculated assuming that the light emission profile is solely dependent on the ion radial distribution, and although the emission is likely dominated by the electron-impact excitation of the background gas, the HWHM observations presumably reflect the behavior of the real ion core to lowest order.

4.5.3 Neutron detectors

Neutron count rate measurements characterized the fusion neutron production performance of the WISCIF device. The neutron detector consists of a long counter, similar in design to the one described by East and Walton^{7,8}. A polyethylene cylinder, used to thermalize the fusion product neutrons ($E_{n,DD} \approx 2.5$ MeV), houses a set of LND 253 ^3He proportional counters (2" diameter, 11.6" long). The detector is biased using a Tennelec TC-952 high-voltage power supply, and a Tennelec TC-175 preamplifier with a Tennelec TC-246 Amplifier/single-channel analyzer (SCA) amplifies the input signal. The pulse-height spectrum from the amplifier output signal is measured using a Northern TN-7200 multichannel analyzer (MCA), and a local Macintosh counts the SCA pulses. The MCA readings are taken simultaneously with the SCA pulse counting to characterize any extra noise in the system, for the pulse-height spectrum of the ^3He detectors is well-known⁸. A sample spectrum taken from the MCA is shown in Fig. 4-10.

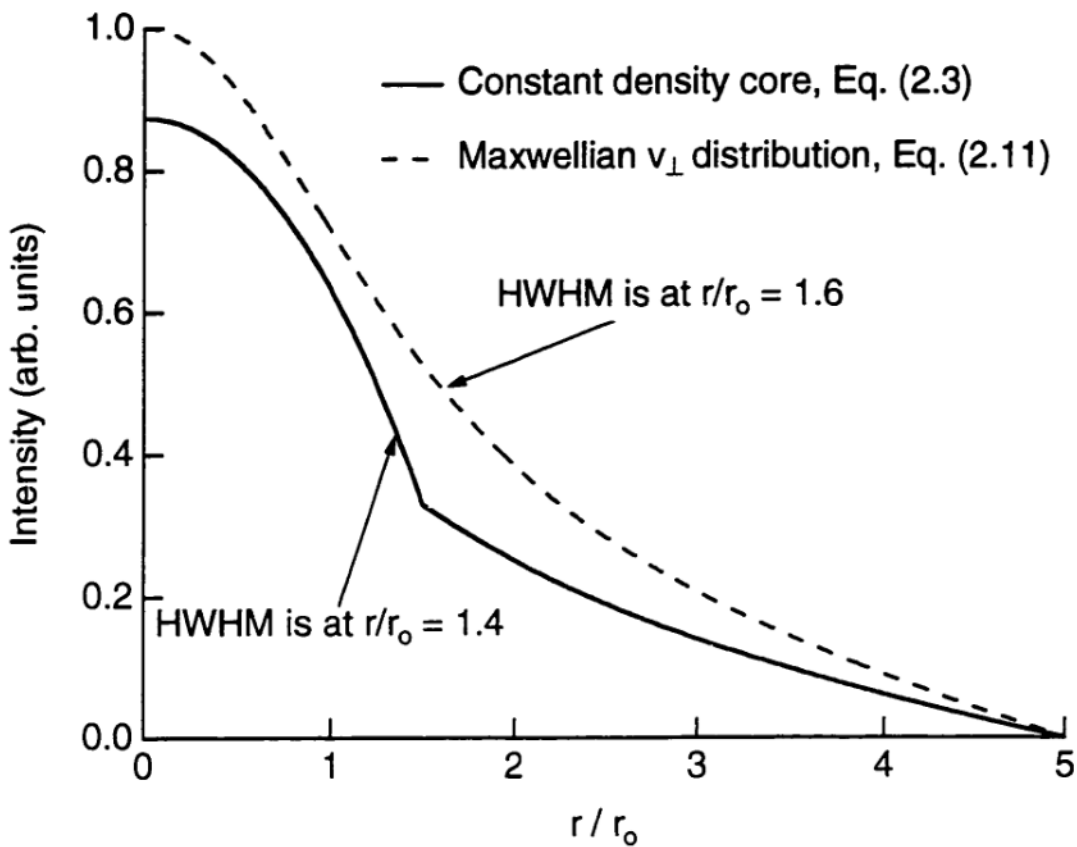


Figure 4-9. Intensity profiles [using Eq. (4.3)] and the resulting HWHM derived from the density distributions described from Chapter 2 ($r_c = 1.5 r_o$).

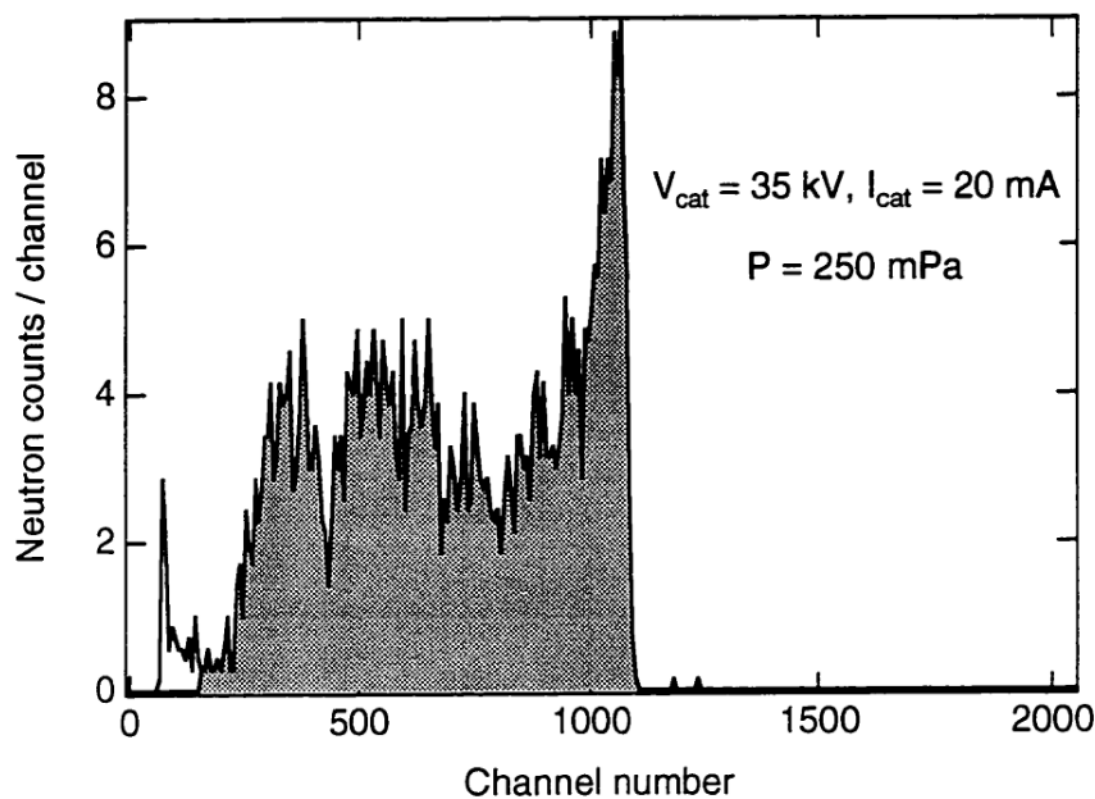


Figure 4-10. Typical pulse height spectrum of the neutron counts from the ${}^3\text{He}$ detector. The shaded region indicates the region-of-interest for the recorded counts, and the integration time for this spectrum was 20 seconds.

The detector efficiency is insensitive to the neutron energy^{7,8}, and therefore *in-situ* calibration is possible using a Pu-Be source (source strength of 2.18×10^6 n/s, $E_n = 4.3$ MeV) obtained from the Nuclear Reactor Laboratory. The detector is located 77.5 ± 0.5 cm away from the center of the device (See Fig. 4-4), and Fig. 4-11 shows the calibration curve taken for this configuration. The detected count rate is very linear with time, and Fig. 4-11 indicates a slope of 387 counts/s. Therefore, a measured rate of 1000 counts/s corresponds to a neutron source strength of 5.6×10^6 n/s. The observed count rates are sufficient such that short integration times can be used during the experimental runs, and six consecutive 20 second integrations were recorded for each condition tested.

A BF₃ "Snoopy"-type detector is also used to monitor the neutron dose rate for the laboratory. It is located approximately 3 m from the center of the device, and the integrated dose rate logged by the detector is recorded after each run for radiation safety concerns. In addition, neutron sensitive film badges are worn by the operators of the experiment, and the University Safety department records the resulting doses monthly.

4.5.4 Fast proton collimator

Spatial localization measurements of the fusion production rate within the device are taken using a collimated (solid angle = 0.79 ster) Canberra model SPD-150-19-100-AM surface barrier diode (depletion region is 150 μm thick). A design, similar to that described by Nadler, *et al.*⁹, is employed, and the detector attaches to a flexible bellow assembly, allowing the viewing angle to be varied during the experiment (Refer to Fig. 4-4 for the viewing geometry). The diode rests in a isolated mount, and it is biased using a Tennelec TC-953 high voltage supply. An EG&G 147 preamplifier and a Tennelec TC-246 amplifier pass the output signal to the Northern TN-7200 MCA.

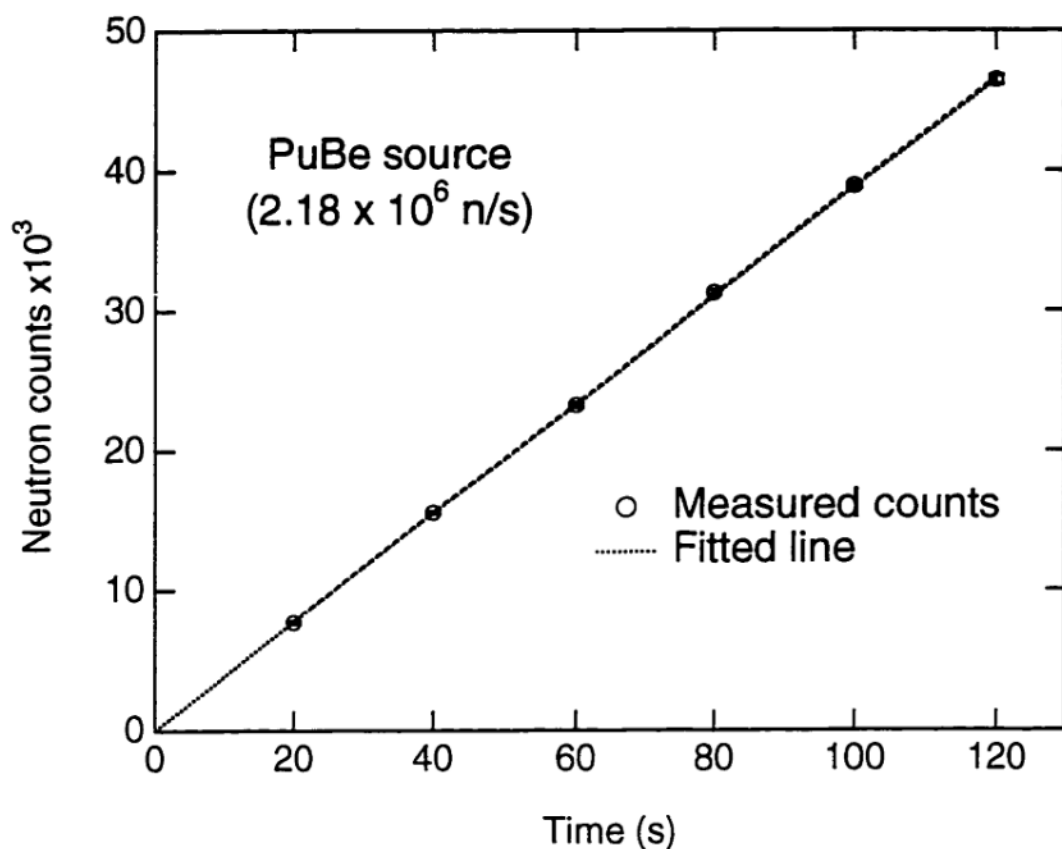


Figure 4-11. Neutron counts from ${}^3\text{He}$ detector using calibrated PuBe source. The fitted line indicates an average detected count rate of 387 counts/s.

The collimator is a 10.0 cm long stainless steel tube that is 1.0 cm in diameter. To protect the diode from the plasma and reduce the noise in the detector, a 18 μm film of aluminum is placed over the end of the collimator. In addition, a 25 μm film of lead is used to attenuate the soft X-rays generated in the system. These films are thin enough to still allow the 3 MeV fusion protons to reach the detector¹⁰, and a sample pulse-height spectrum of the proton signal is shown in Fig. 4-12.

Also included in Fig. 4-12 is the spectrum for the same experimental conditions using hydrogen instead of deuterium. The lack of signal observed in hydrogen for channel numbers greater than 600 confirm that the pulses seen in deuterium are from the fusion protons. Neutron measurements taken simultaneously with the proton measurements found 1.0×10^4 n/s for the hydrogen run (due to the residual deuterium in the system) compared to the 1.0×10^6 n/s observed in the deuterium run. This is consistent with the number of counts seen above channel 600 for the hydrogen case ($\approx 1\%$ of the deuterium signal).

Only very stable discharges with reasonably high count rates can be studied with this diode detection system due to noise considerations. Higher power discharges cause small arcs near the base of the cathode support, which generate false counts in the detection circuit. The integration time is also limited to 30 minutes in order to measure a number of spatial locations in one experimental run period (avoiding day-to-day systematic variations). This period is limited to 4 hours, for the noise floor of the detection circuit would creep into the proton signal as the diode temperature rose. The spatial resolution of the collimator is chosen such that a significant number of counts could be recorded during the 30 minute integration. While higher spatial resolution is always desirable, the present system provides adequate insight into the fusion reactivity radial distribution to support the conclusions presented in Chapter 6.

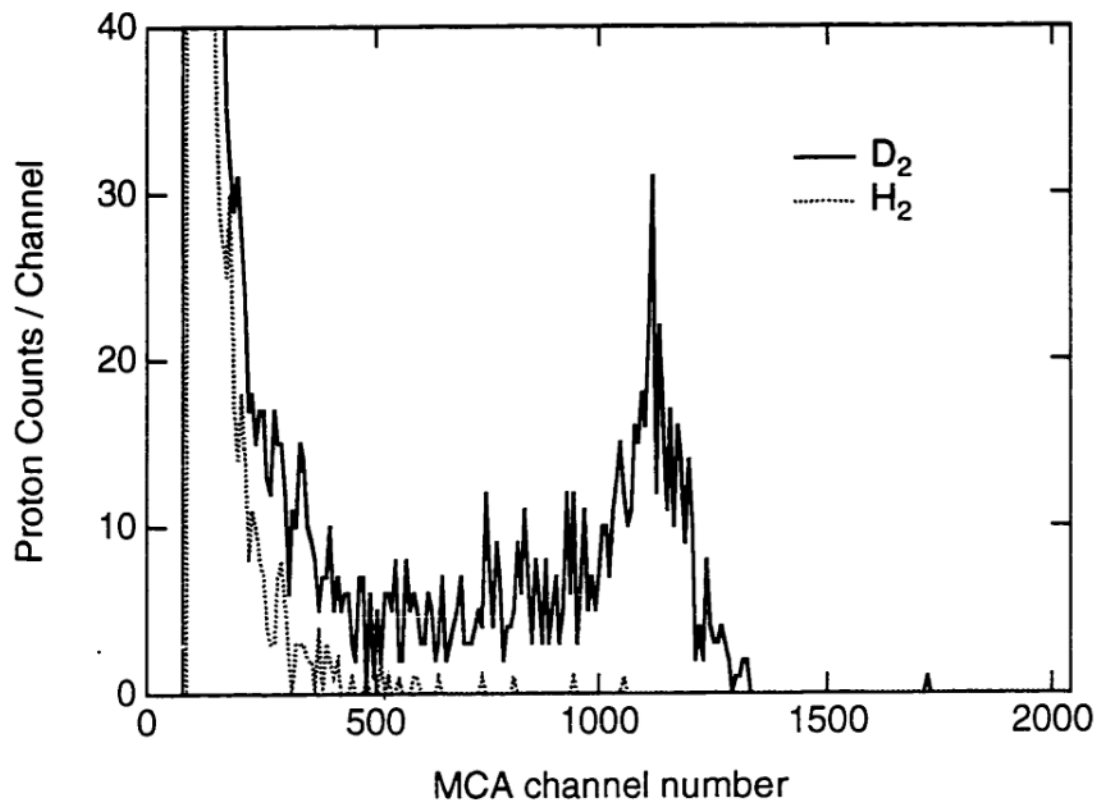


Figure 4-12. Sample MCA output of the fast proton pulse height spectrum (30 minute integration).

4.6 REFERENCES

- ¹R. Hirsch, *J. Appl. Phys.* **38**, 4522 (1967).
- ²W. M. Black and J. W. Robinson, *J. Appl. Phys.* **45**, 2497 (1974).
- ³J. T. Verdeyen, B. E. Cherrington, D. A. Swanson, and D. J. Meeker, *Ann. NY Acad. Sci.* **251**, 126 (1975).
- ⁴G. H. Miley, J. Nadler, T. Hochberg, Y. Gu, O. Barnouin, J. Lovberg, *Fusion Technol.* **19**, 840 (1991).
- ⁵N. Hershkowitz, in *Plasma Diagnostics*, edited by O. Auciello and D. L. Flamm (Academic Press, Boston, 1989), p. 176.
- ⁶K. Miyamoto, *Plasma Physics for Nuclear Fusion* (M.I.T. Press, Cambridge, 1987), p. 507.
- ⁷L. V. East and R. B. Walton, *Nuc. Instrum. and Methods* **72**, 161 (1969).
- ⁸G. F. Knoll, *Radiation Detection and Measurement* (Wiley, New York, 1989), p. 514.
- ⁹J. H. Nadler, Y. Gu, and G. H. Miley, *Rev. Sci. Instrum.* **63**, 4810 (1992).
- ¹⁰E. B. Saloman and J. H. Hubbel, U. S. Department of Commerce Report #NBSIR 86-3431 (1986).

Chapter 5: Ion Flow Characterization

Better models of system behavior can be developed by determining the effects of neutral pressure, asymmetries, injected current and applied voltage on the ion velocity and density distributions in a SCIF device. As noted earlier, most past work on SCIF systems concentrated on neutron production rate measurements, and very little experimental data has been obtained concerning the characteristics of the ion flow and the structure of the potential well.

Initially, the WISCIF experiments discussed here concentrated on convergence scaling and measurements of the potential distribution throughout the ion flow and the core ion density. This work centered on relatively low density, lower energy ($n \sim 10^{16} \text{ m}^{-3}$, $E_i \approx 5\text{-}20 \text{ keV}$) SCIF operation, where previous experiments indicated significant fusion production rates¹⁻³. Lower neutral pressure ($\leq 53 \text{ mPa H}_2$), “converged-core” ion flows were studied in order to minimize the effects of neutral collisions on the flow convergence, and the resulting discharge characteristics are different than the glow discharge modes studied previously. The first direct measurements of the central ion density, radial electrostatic potential profile, and accelerating potential asymmetries were also provided using high-voltage electrostatic probes.

This chapter first describes the effects of pressure on the general discharge characteristics, measurements of the electrostatic radial potential distributions, observations

of the flow convergence dependencies with cathode voltage, current, neutral pressure, and potential well symmetry, and determinations of the core ion density from a variety of measurements and estimates. A discussion follows linking the observed flow convergence to an orbit model accounting for defocusing due to potential asymmetries. The measured core ion density is then also compared to the classical ion flow models discussed in Chapter 2.

5.1 GENERAL DISCHARGE CHARACTERISTICS

These experiments found three distinct modes of operation that were consistent with regimes described by Miley, *et al.* in similar regimes of applied voltage, current, and pressure². The highest pressures ($P > 2000$ mPa) produced a collisional glow-discharge known as the “halo” mode. The plasma showed a broad structure that was highly symmetric with one or two electron beams that exit the core region [See Figure 5-1(a)]. Other investigators have studied the neutron performance of this discharge, but the plasma dynamics in this regime have yet to be fully investigated^{2,4}.

The lack of focusing observed in the halo mode is likely due to plasma-neutral interactions. The ion-neutral mean free path in the accelerating region ($\lambda_{in} = 1/n_o\sigma_{in}$, where σ_{in} is the total ion-neutral collision cross-section) at these pressures was ≤ 1.0 cm for 5 - 10 keV ions in hydrogen⁵⁻⁷. Hence, ions cannot properly converge with scattering due to these frequent interactions, and volume ionization was quite probable throughout the region inside the cathode. Enough ionization events were supplied throughout the chamber to maintain the discharge, relaxing the need for an external ion source to sustain the discharge.

At lower pressures (10 mPa $< P < 2000$ mPa), the beams of electrons disappeared, and the spherical glow concentrated into a central bright spot with filament-like structures directed outward from the openings of the inner globe [See Fig. 5-1(b)]. The experiments performed by Miley, *et al.* have concentrated on this “star” mode of operation². Neutral

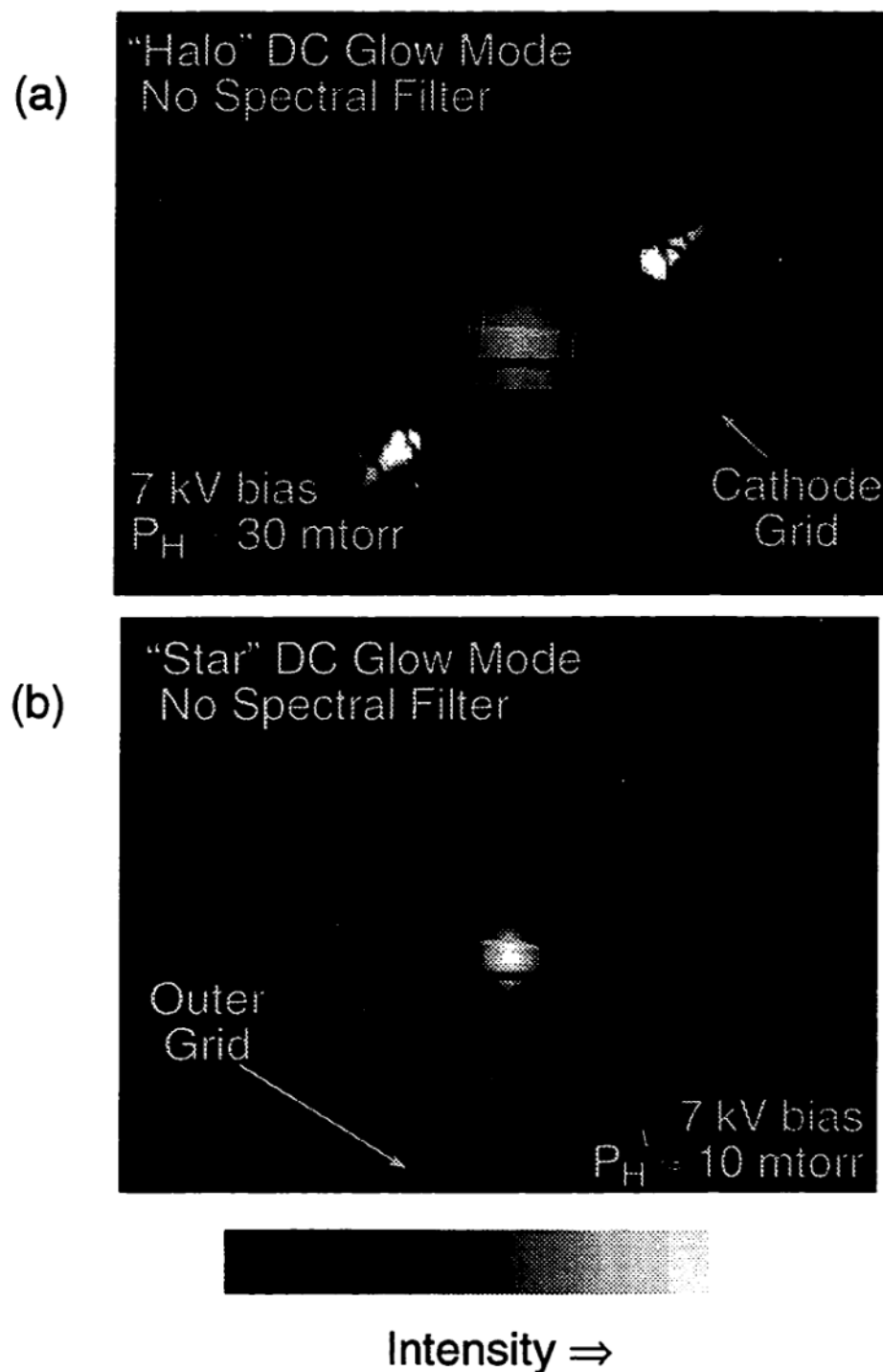


Figure 5-1. Images of the (a) halo and (b) star modes of operation. The cathode grid shown here has a 5.0 cm radius with a 30° poloidal wire spacing.

collisions were significant ($\lambda_{in} \leq 10$ cm)⁵⁻⁷, as this discharge was also self-sustaining. The beam-background interactions appeared to dominate the fusion rate ($R_{fus} \propto I^{2.3}$, consistent with the simple flow reactivity analysis discussed in Section 2.4 (e.g. $n_o \gg n_i$).

Neutral collisions must be reduced further in order to achieve the more power efficient beam-beam scaling ($R_{fus} \propto I^2$). For pressures below 100 mPa, the “converged-core” (CC) mode was generated (See Fig. 4-8). The main operational differences between this and the star mode were that an external source of ions is necessary to maintain the plasma, the center bright spot appears slightly less-focused, and the filament-like structure is no longer evident.

All of the proposed high fusion rate concepts based on the SCIF concept rely on I^2 scaling of the fusion power output, implying operation in the CC mode. Therefore, the WISCIF ion flow experiments concentrated on the CC mode because of the reduction of the neutral interactions that tend to give linear current scaling and presumably hinder the convergence of the flow.

5.2 POTENTIAL DISTRIBUTION MEASUREMENTS

As discussed in Chapter 2, the ion velocity distribution, and therefore the electrostatic potential distribution, is needed to accurately estimate the fusion reactivity of a SCIF device. In addition, the amount of current that can be injected into the system may also be influenced by this potential distribution.

For example, if the ion flow is sufficiently collisionless, then a space-charge-limited flow into the high-voltage cathode would be expected. Indeed, measurements of the cathode current versus voltage (shown in Fig. 5-2) show a $V^{3/2}$ scaling for voltages above 3 kV in a variety of low-pressure cases consistent with Eq. (2.17). The increase observed in I_{cat} with

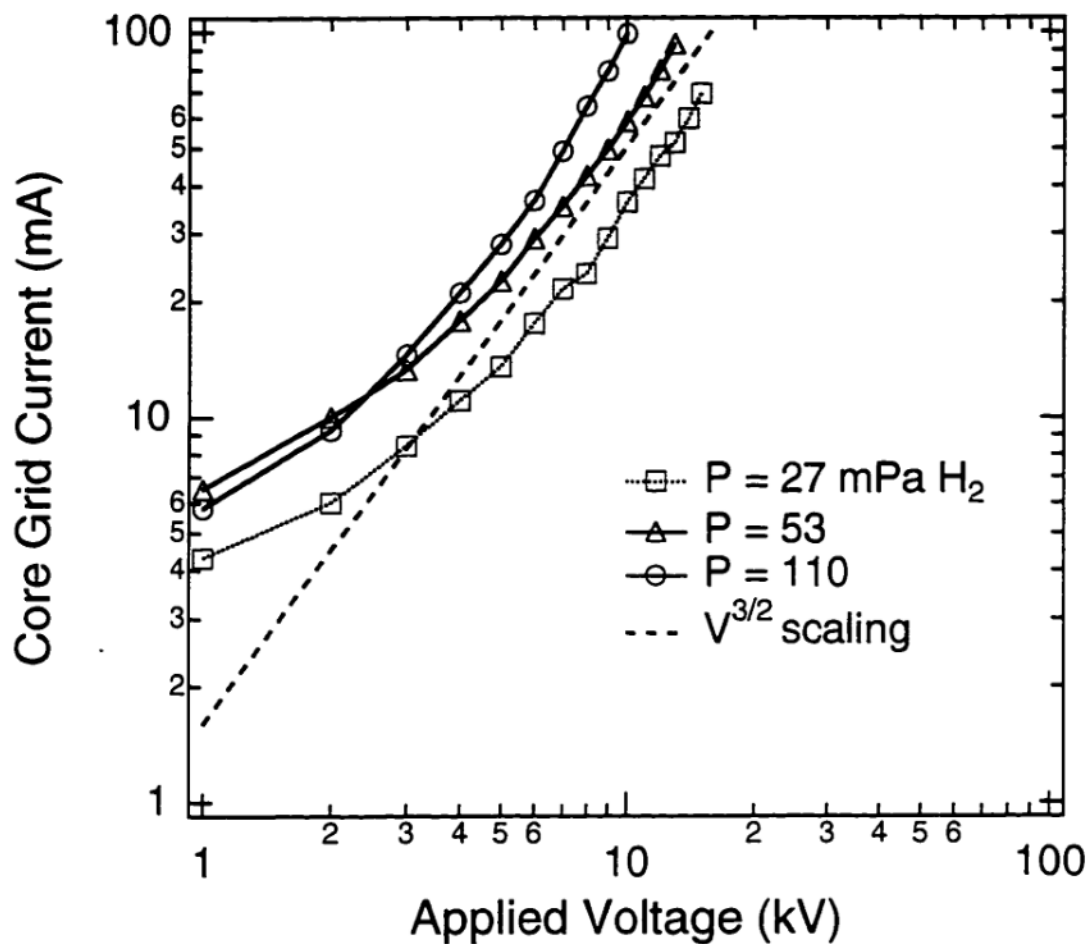


Figure 5-2. Cathode current versus applied voltage for different converged-core discharges showing a $V^{3/2}$ dependence above 3 kV for each pressure range.

higher pressures is indicative of the increased edge plasma density with pressure (plasma source biases were held constant).

Figure 5-3 shows plots of the plasma potential, measured via an emissive probe using the inflection method [See Fig. 4-7(b)]⁸, and the probe floating potential as a function of radius for a typical low-pressure case ($P = 13 \text{ mPa H}_2$, $V_{cat} = 5.0 \text{ kV}$, $I_{cat} = 40 \text{ mA}$). For these probe scans, ion flows with energies up to 5.0 kV in either 13 or 27 mPa of hydrogen fill pressure were studied, and the collected cathode currents at these conditions were either 20 or 40 mA. The measured radial plasma potential distributions show detailed agreement with the space-charge potential model in the mantle region [Eq. (2.19)] plus a variety of phenomena inside the central cathode grid.

A fit of Eq. (2.19), which is normalized to the observed voltage at $r = 5.0 \text{ cm}$ and uses an anode radius of 9.0 cm, indicates good agreement with the measured plasma potential profile, as seen in Fig. 5-3. The theoretical current limit for the included best-fit graph in Fig. 5-3 is 150 mA, which is 7.5 times greater than the collected ion current of 20 mA (assuming $\delta_e \approx 1$)⁹. This roughly agrees with the geometrical recirculation factor of 8.6 calculated from Eq. (2.13) for the globe used ($\eta = 0.94$).

Figure 5-4 shows comparisons of the radial potential profile for different currents and pressures; the space-charge-limited model fits the measured data well in the mantle region. The amount of recirculating current determined as above also remains fairly constant for the three different cases studied (see Table 5-1). The effective source radius and the voltage at $r = 5.0 \text{ cm}$ appear to self-consistently adjust to provide the required space-charge-limited current density.

The observed potential at 5.0 cm is not equal to the applied 5.0 kV due to Debye shielding of the grid wires (λ_D is measured $\sim 0.05 \text{ cm}$ typically) and to asymmetries in the

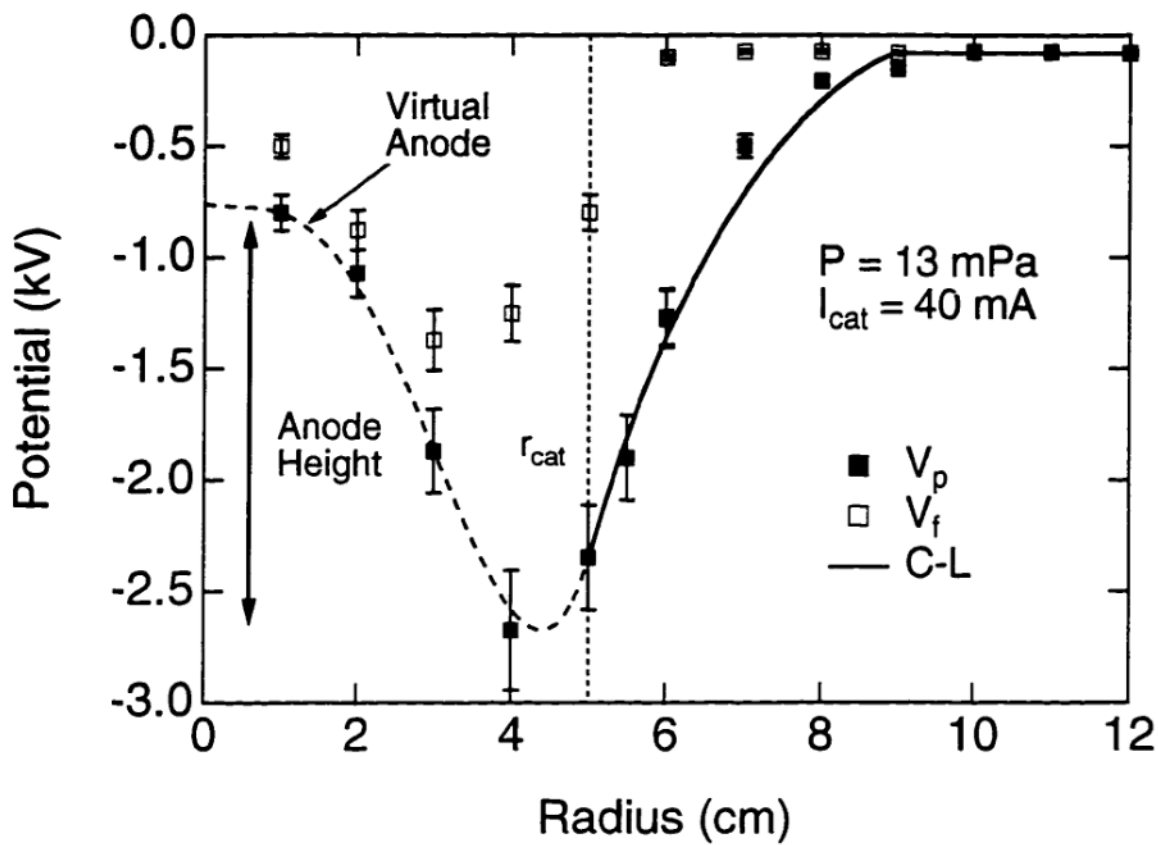


Figure 5-3. Radial profile of the floating (V_f) and plasma (V_p) potentials for a 13 mPa, 5.0 kV, 40 mA case. Also included (solid line) is a normalized fit of the Child-Langmuir (C-L) potential distribution as expected from Eq. (2.19) (for $r < r_{cat}$).

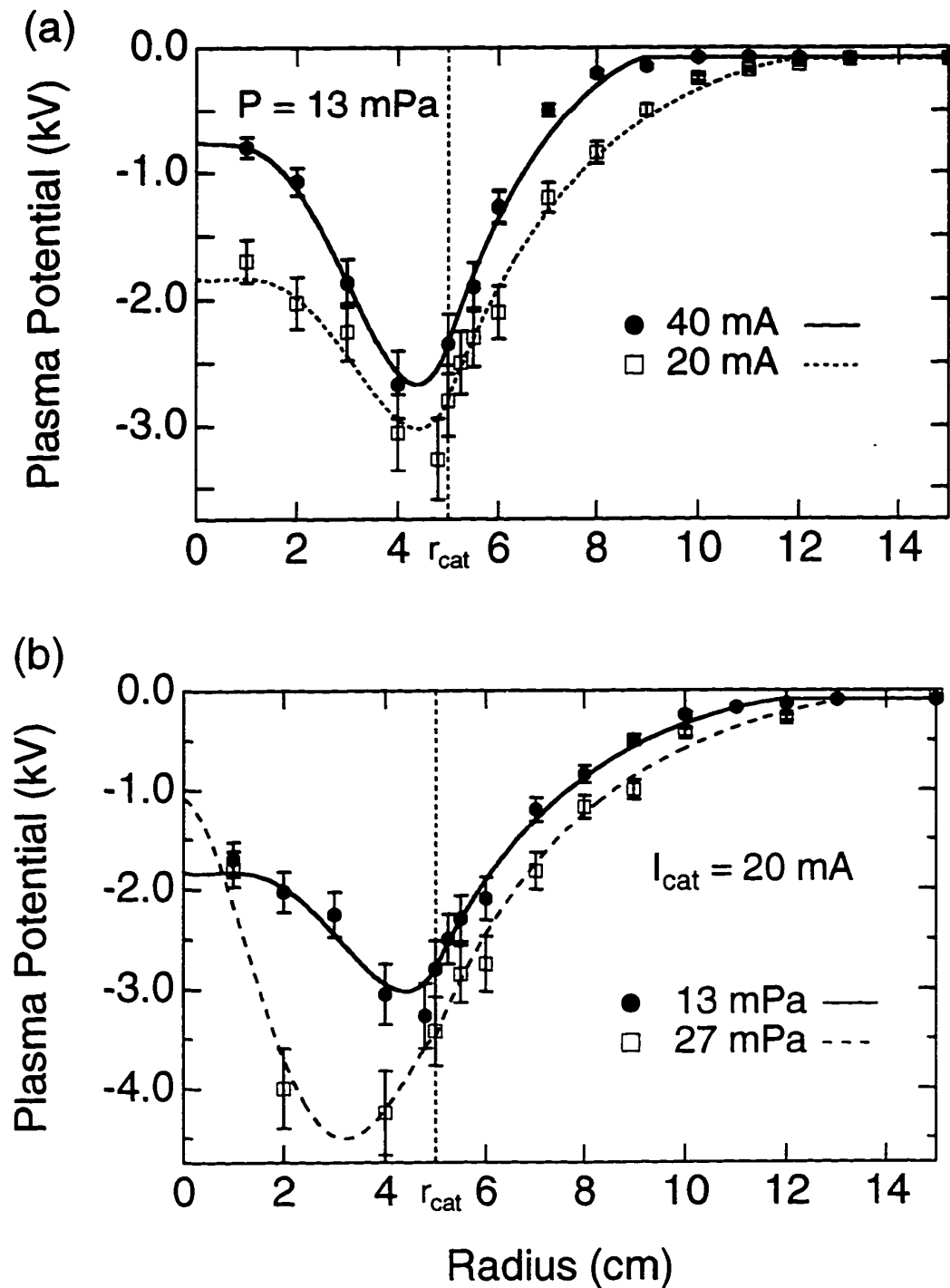


Figure 5-4. Plasma potential measurements for different (a) cathode currents and (b) neutral background pressures. Included is the normalized Child-Langmuir potential distributions for $r \geq r_{cat}$ and spline fits through the data for $r < r_{cat}$.

potential because of the finite wire spacing. The measurements shown in Figs. 5-3 and 5-4 are from between cathode wires, where the plasma potential is weakest. As much as a factor of two difference between the applied cathode voltage and the observed potential between grid wires was observed. The effects of asymmetries on the potential distribution are discussed in more detail in the next section.

For neutral Maxwellian plasmas, the floating potential (V_f) of a probe is normally biased negative with respect to the plasma potential due to the higher mobility of electrons to reach the probe surface ($I_i = I_e$ at V_f). A comparison of the measured floating and plasma (V_p) potentials in the mantle and plateau regions of a low-pressure SCIF (See Fig. 5-3) indicate the probe biases itself positive at the floating potential ($V_f > V_p$) to reflect the direct ion flow and collect the local electron saturation current. This signifies a deficiency of electron current in the ion flow, and hence $I_i > I_e$ for these low-pressure conditions. The difference between V_f and V_p is not as pronounced in the central core region, especially for higher pressure cases, which suggests a higher electron density or temperature in the core.

Pressure (mPa)	Cathode Grid Current (mA)	Eff. Source Radius (cm)	Eff. Cathode Voltage (V)	Theoretical Current (mA)	Estimated Recirculation Factor
13	20	12.0	-2700	71	7.1
13	40	9.0	-2300	150	7.5
27	20	13.5	-3400	71	7.1

Table 5-1. Theoretical currents [from Eq. (2.17)] and the estimated recirculation factor for the three cases shown in Fig. 5-4 (applied cathode voltage = -5000 V).

Figures 5-3 and 5-4 also show a virtual anode (i.e. potential hill) in the converged core region where the ion charge density increases due to radial convergence. Under all conditions studied, the core virtual anode was a simple monotonically decreasing potential hill as r increases from 0 to r_{cat} .

5.3 CORE FLOW CONVERGENCE MEASUREMENTS

Flow convergence is an important figure-of-merit for SCIF devices, as the fusion production rate of a beam-beam dominated system is inversely proportional to the convergence radius of the ion flow¹⁰. Convergence here is defined as the ratio of the cathode to core radii [$C = r_{cat}/r_c$], and the core ion density is then expected to scale as C^2 .

It is critical to understand and characterize any system parameters (i.e. accelerating well symmetry, applied voltage, injected current, neutral pressure) that may limit the flow convergence for the beam-beam dominated systems. For example, beam-beam fusion reactivity is expected to scale with the injected current squared, but if the core size also gets larger with current, the reaction rate will then not increase quadratically.

The simple purely-radial flow model breaks down near the origin as the impact of perpendicular velocities becomes significant, and the ion velocity distribution approaches a spherical shell in velocity space in the core region [as shown in Fig. 2-2(d)]. This effect was seen experimentally with double-probe I-V characteristics from the plateau and core regions. Since $I_i > I_e$ in the ion flow, the double-probe actually reflects the energetic ion beam distribution instead of the electron distribution as in normal, non-flowing Maxwellian plasmas. The slope of the I-V trace near $V = 0$ is then related to the spread of the ion energy distribution, where a beam-like distribution leads to a large slope at $V = 0$ (See Appendix 2).

Figure 5-5 shows three I-V characteristics taken in the plateau and core regions, and the slope of the I-V traces decreased as the probe entered the core region. The sharp slope

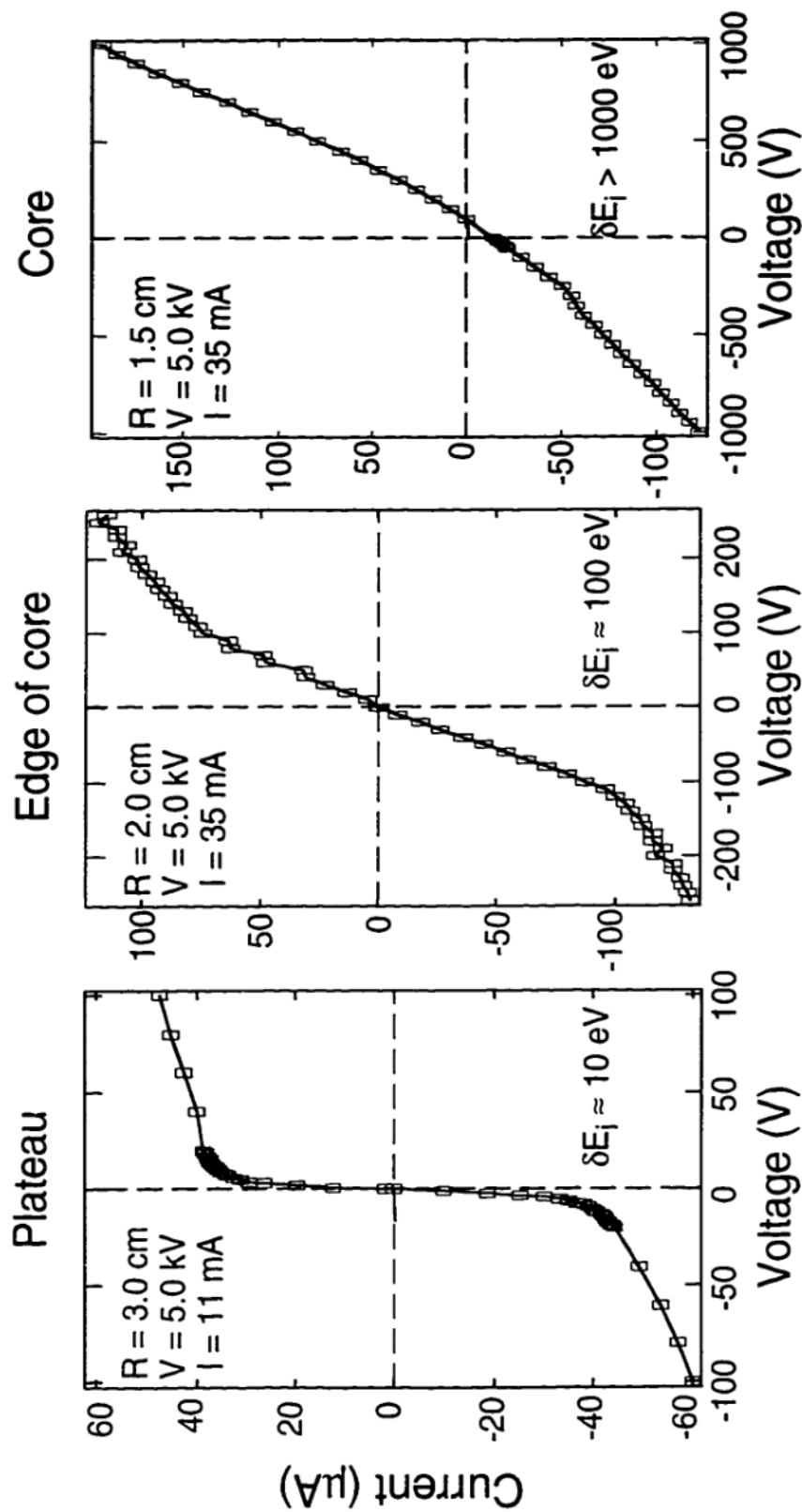


Figure 5-5. Double probe IV characteristics for different radii near and inside the converged core region.

seen in the plateau region is indicative of a low-temperature or beam-like distribution, which is similar to the ideal distribution expected in that region [see Fig. 2-2(c)]. Similarly, the broader slope in the core region is consistent with a broad energy or isotropic distribution, which resembles the ideal spherical-shell distribution expected in the core region and shown in Fig. 2-2(d). The detailed structure of the ion energy distribution in the core region cannot be well-determined using this measurement technique, but an obvious change in the character of the ion distribution is seen between the plateau and core regions.

Several measurements indicate that the converged ion core size reduces, and hence the flow convergence improves, with increasing neutral pressure, decreasing overall current, or increasing accelerating voltage. These results are seen in Figs. 5-4 and 5-6, which show the potential structures in the core region (Fig. 5-4) and the half-width-at-half-maximum (HWHM) radius of the core intensity profiles from the CCD images (Fig. 5-6). Fig. 5-4(a) indicates the core anode height increasing with I_{cat} while 5-6(a) shows an increase in HWHM with I_{cat} . Figs. 5-4(b) and 5-6(b) indicate a strong decrease of the core size with neutral gas pressure (P), and Fig. 5-6(b) also indicates a decrease of the core size with applied voltage (V_{cat}).

For comparison, the ideal geometric limit given by Eq. (2.2) is also included in Figure 5-6:

$$r_c = \frac{3}{2} R_a \frac{\langle v_\perp \rangle}{v_c} \approx \frac{3}{2} R_a \sqrt{\frac{kT_{edge}}{q\Phi_c}} \quad (2.2)$$

In all cases, the observed core size is larger than the ideal limit, but the tightest cores of 0.6 cm radius are within a factor of 4 - 5 of the limit for those conditions ($V_{cat} = 10$ kV, $\Phi_c \sim 5$ kV, $T_{edge} \sim 0.1$ eV, $R = 20$ cm)¹¹.

The decrease observed in r_c with V_{cat} is much faster than the inverse-square-root scaling expected from Eq. (2.2), and the most likely cause of this non-ideal convergence

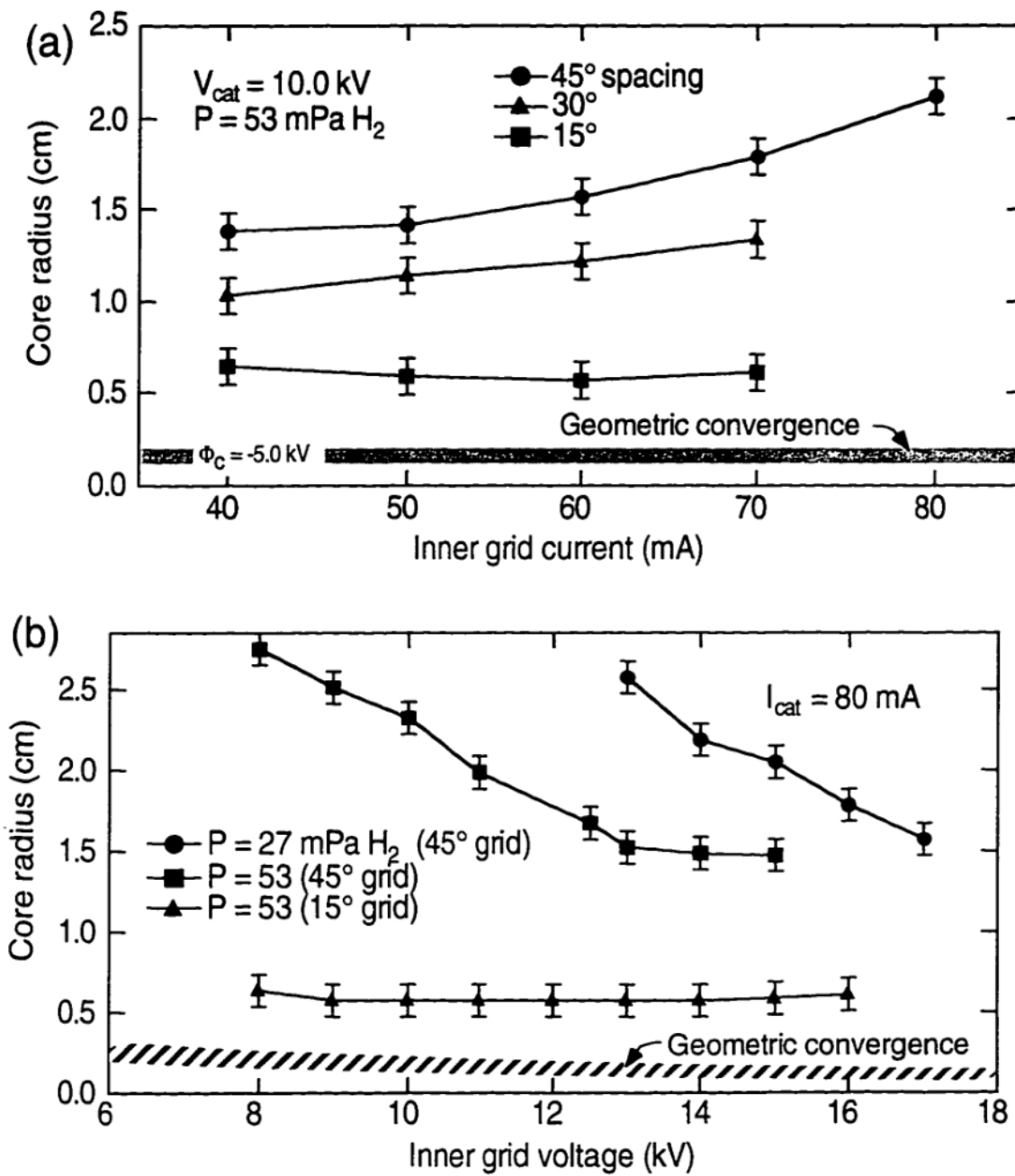


Figure 5-6. Core size measurements for 45, 30, and 15° poloidal spacing grids as derived from the HWHM of the visible (H_α) core emission for variations of (a) cathode current and (b) cathode voltage. Included is the estimated geometric convergence from Eq. (2.2).

behavior is asymmetries in the electrostatic potential from the finite grid wires of the cathode. The potential near the cathode grid wires is more negative than its value between grid wires (as mentioned above in Section 5.2), and this results in a significant perpendicular force on the ions toward the wires. In addition, the region of highest acceleration for the flow is at radii nearest the cathode, where these large irregularities in the potential are also found. The magnitude of these potential variations decreases as the grid wire spacing decreases, and therefore finely-spaced grids (e.g. 15° poloidal spacing) would be expected to yield smaller core sizes than more coarsely-spaced (45° spacing) grids.

Indeed, the observed core sizes decrease with decreasing grid spacing, and Figure 5-6 shows comparisons of the core size scalings for differently spaced grids to demonstrate this point. Intensity profiles through the core region for the 45° and 15° poloidal spacing grids are shown in Fig. 5-7, which perhaps most dramatically shows the dependence of core size on potential well asymmetries. Here, a factor of 2.5 reduction in core size resulted from tripling the density of grid wires on the cathode while holding all other parameters fixed. Note that by increasing the grid wire density, the grid transparency, and hence the amount of recirculating current, decreases. The measured HWHM also decreases with decreasing current [See Fig. 5-6(a)], but this effect is not strong enough to account for the factor of 2.5 observed. Therefore, the observed enhancement of convergence is mainly due to the improved symmetry of the accelerating potential well.

To investigate the magnitude of the asymmetries, the poloidal variations in the plasma potential were measured by rotating the cathode globe past a fixed emissive probe. Figure 5-8 shows the angular variation of the plasma potential for data measured at $r = 5.0, 5.5$ and 8.0 cm for the 53 mPa, $I_{meas} = 20$ mA case. For comparison, the expected vacuum-field variations due to the longitudinal grid loops are calculated using superposition of the potential distribution of a single loop, given by¹²:

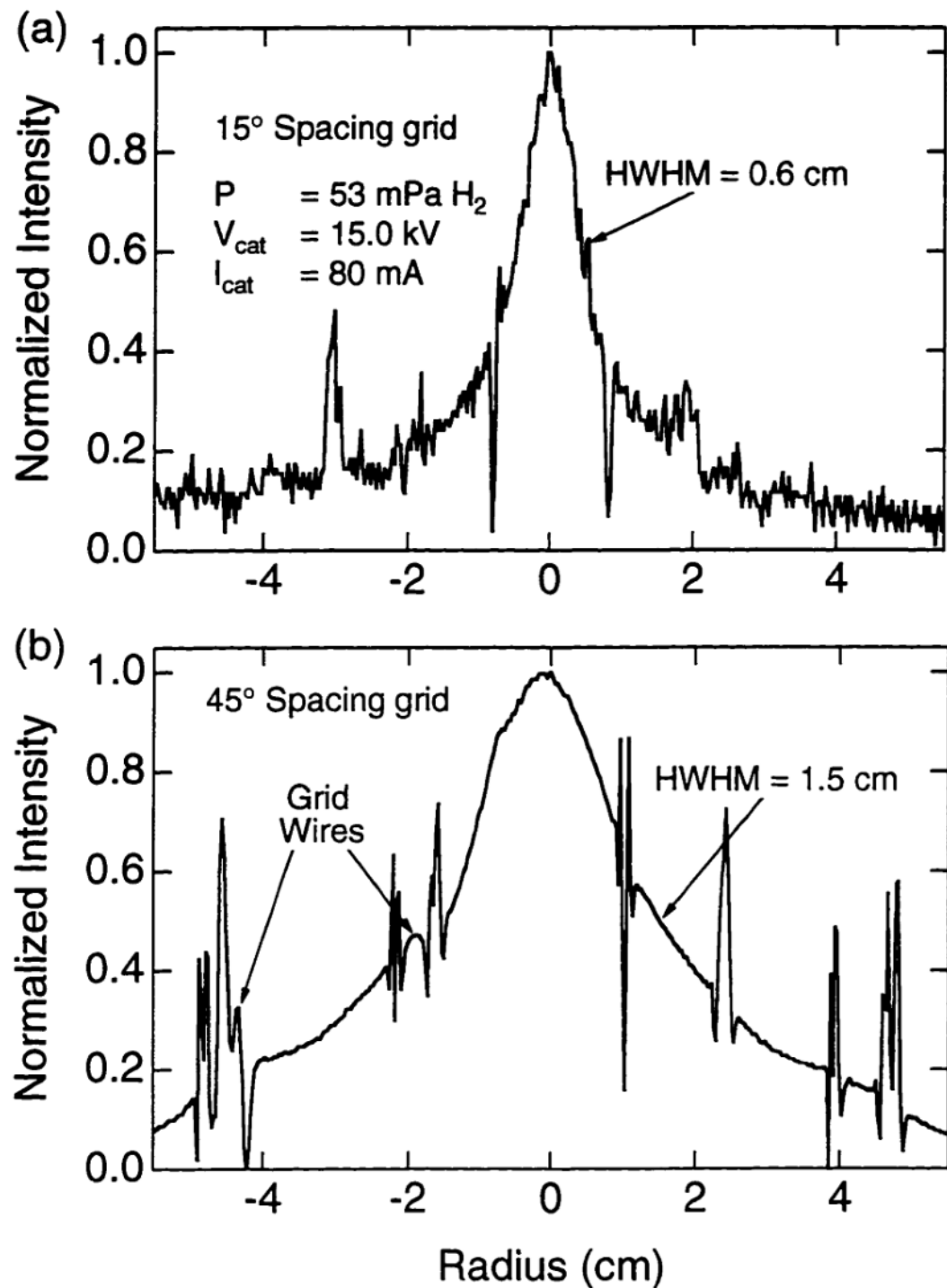


Figure 5-7. Visible emission intensity profiles for the (a) 45° and (b) 15° poloidal spacing grids.

$$\Phi(r,\theta) = q \sum_{l=0}^{\infty} \left(\frac{r_-^l}{r_+^{l+1}} \right) P_l(0) P_l(\cos \theta) \quad (5.1)$$

where P_l is a Legendre polynomial, and r_- and r_+ are the lesser/greater of the field and loop radii. The corresponding vacuum potential calculations from Eq. (5.1) are also indicated in Fig. 5-8 using the value of q that best fit the data for each of the three different radii. These normalized vacuum and measured plasma potentials match very well for the conditions shown in Fig. 5-8, which is generally true for all cases investigated.

The normalized vacuum potential fit through the $r = 5.0$ cm data is not equal to the applied cathode voltage of 5.0 kV at the grid wire locations (0 and 30°). This discrepancy is likely due to local Debye shielding ($\lambda_D \leq 0.5$ cm as estimated from floating potential measurements very near the grid wires), and the data in Fig 5-8 indicate a shielding of ≈ 400 V. The amount of shielding also appears to increase with increasing the grid current and decreasing background neutral density. This is shown in Table 5-1 through the dependence of the effective cathode voltage (V_{eff}) on pressure and current (less negative V_{eff} represents larger shielding). Qualitatively, a larger amount of shielding near the wires results in poorer flow convergence, for ions will have less energy entering the core region and the larger potential gradients near the wires will scatter the ions further. This effect therefore contributes to and may account for the observed core size scalings with pressure and current.

5.4 CORE DENSITY MEASUREMENTS

To further characterize the ion flow, the ion density in the core region was measured and compared against the simple flow estimates given in Eqs. (2.4) and (2.16). Direct measurements are given by the floating double probe diagnostic, and for the core I-V characteristic in Fig. 5-5, where $i_{sat} \geq 150 \mu\text{A}$ and $\Phi_p = 2500$ V, the ion density calculated from Eq. (4.1) is $\geq 1.3 \times 10^{15} \text{ m}^{-3}$ for the 5 kV, 35 mA ion flow.

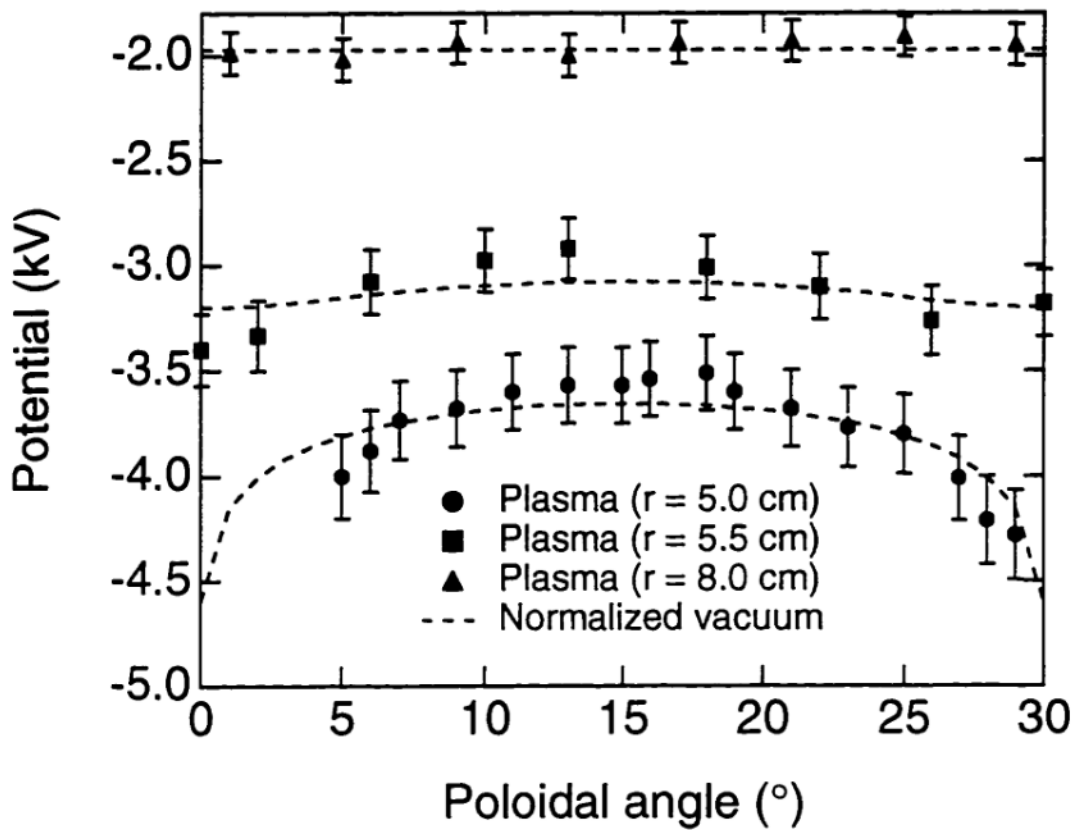


Figure 5-8. Plasma potential measurements versus poloidal angle for a 5.0 kV, 20 mA, 53 mPa ion flow at radii of 5.0, 5.5, and 8.0 cm. Grid wires are spaced at 0 and 30° for this cathode.

The edge density ($r = 20$ cm) for these conditions, measured with a standard Langmuir probe, was $2.2 \times 10^{14} \text{ m}^{-3}$. In order to compare the double probe measurements with the collisionless estimate given by Eq. (2.4), the value of $E_{||}$ at 20 cm is needed:

$$n_{ic} = 4n_i(R) \left(\frac{R}{r_c}\right)^2 \frac{v(R)}{v_c} = 4n_i(R) \left(\frac{R}{r_c}\right)^2 \sqrt{\frac{E_{||}(R)}{q\Phi_c}} \quad (2.4)$$

If the edge plasma behaves as a uniform plasma, then the ions will fall into the accelerating potential boundary at the local Bohm velocity [or $E_{||}(R) = 0.5T_e \approx 5 \text{ eV}$]. However, non-uniformities in the edge plasma potential would give the ions a distribution of parallel energies (depending on their birth positions between $r = 20 - 45$ cm). A minimal estimate is given by the ion thermal velocity (or $E_{||}(R) \sim 0.1 \text{ eV}$). Therefore the predicted core density from Eq. (2.4) is $6.1 \times 10^{15} \text{ m}^{-3}$ if $E_{||}(R) = 5 \text{ eV}$ or $0.9 \times 10^{15} \text{ m}^{-3}$ if $E_{||}(R) = 0.1 \text{ eV}$ (using $r_c = 1.6 \text{ cm}$, $\Phi_c \approx 2500 \text{ V}$).

The measured cathode current also gives an estimate of the core density from Eq. (2.16):

$$n_{ic} = \frac{\eta I_{meas}}{(1-\eta^2)(1+\delta_e)} \left(\frac{1}{ev_c \pi r_c^2} \right) \quad (2.16)$$

Again assuming $\delta_e \approx 1$ and $\Phi_c \approx 2500 \text{ V}$ for these conditions ($\eta = 0.91$, and $r_c = 1.6 \text{ cm}$ for this 5 kV, 35 mA discharge), Eq. (2.16) gives a core density of $1.0 \times 10^{15} \text{ m}^{-3}$.

Another estimate of the core density was provided by pyrometric measurements of a single alumina probe tip inserted into a higher energy core. The tip temperature reached over 2200°C for a 10 kV, 80 mA discharge, and assuming that the power deposited was solely radiated away, then the ion density can be calculated from a power balance on the probe tip:

$$n_i \approx \frac{P_{rad}}{v_i E_i} = \frac{\epsilon \sigma T_{probe}^4}{\sqrt{2M} (q\Phi_c)^{3/2}} \quad (5.2)$$

where ϵ is the emissivity of the alumina (≈ 0.7)¹³, σ is the Stefan-Boltzmann constant, and

T_{probe} is the surface temperature of the probe. For the 10 kV case, where $q\Phi_c \approx 5000$ eV and $T_{probe} \approx 2500$ K, n_{ic} is approximately $1.9 \times 10^{15} \text{ m}^{-3}$. For these conditions, Eq. (2.16) also predicts a core ion density of $1.5 \times 10^{15} \text{ m}^{-3}$ ($r_c \approx 2.1$ cm for 10 kV, 80 mA; 45° spacing grid, $\eta = 0.94$), which is in good agreement with the pyrometric estimate.

These varied core density measurements and calculations are shown in Table 5-2, with the pyrometric estimate scaled to the conditions of the double-probe measurements using Eq. (2.16). These values of the core ion density indicate an overall increase in density by a factor of 5-10 compared to the edge plasma.

No double probe data is available between the edge and core due to the large difference between the floating and plasma potentials in this intermediate region (see Fig. 5-3). Since the double probe is a floating diagnostic, a measure of ion current for Eq. (4.1) is only possible if $V_f \approx V_p$. Figure 5-3 indicates that $V_f > V_p$ in the plateau and mantle regions, and no visible knee in the I-V characteristics was observed for the double probe at these radii.

Double Probe Measurement Eq. (4.1)	Cathode Current Estimate Eq. (2.16)	Pyrometric Estimate Eq. (5.2)	Simple Flow Model Estimate Eq. (2.4)
1.3×10^{15}	1.0×10^{15}	1.5×10^{15}	0.9×10^{15}

Table 5-2. Core ion density measurements and calculations (m^{-3}) for a 5 kV, 35 mA ion flow at 53 mPa. The edge ion density for these conditions is $2.2 \times 10^{14} \text{ m}^{-3}$.

In general, the increase in core density, compared to the cold edge density, is in relatively good agreement with the simple estimate given by Eq. (2.4), and hence the ion density appears to follow classical expectations at the conditions studied.

5.5 DISCUSSION AND CONCLUSIONS

The plasma potential measurements for the low-pressure ion flows discussed above are consistent with a collisionless, space-charge-limited flow model in the mantle region. In addition, both the effective source radius (R_{eff}) and cathode voltage (V_{eff}) adjust accordingly to provide the required current density for the edge conditions. Table 5-1 shows that, as expected from the space-charge model, R_{eff} decreases (through α) as I_{cat} increases (at constant V_{cat} and P), but note that V_{eff} also decreases. This is attributed to enhanced shielding of the cathode grid wires by the increased local plasma density at higher currents. The increase in V_{eff} and R_{eff} for increased pressure (at constant V_{cat} and I_{cat}) is also consistent with the space-charge model, for R_{eff} increases to offset the increased plasma density and V_{eff} observed at higher pressure.

The symmetry and depth of the accelerating potential well (resulting in improved ion flow convergence) increase with increasing cathode voltage and pressure and with decreasing current and grid wire spacing (cf. Figs. 5-6 and 5-7). The decrease in core size with voltage is much more rapid than the inverse-square-root expectation from Eq. (2.2). In addition, the data shown in Figure 5-6(b) suggest that the converged core size may saturate at a level still 4-5 times higher than the geometric convergence expectation from Eq. (2.2). Hence, Equation (2.2) does not adequately predict the ion flow convergence due to the large asymmetries in the accelerating potential well, and the expected core density scaling from Eq. (2.5) would be invalid as well.

To better estimate the expected core size in the presence of the observed potential variations, a Monte-Carlo simulation of single ion orbits in an asymmetric potential well was developed. For these calculations, a two-dimensional model of the plasma potential is generated using a space-charge-limited distribution in the mantle region and a Gaussian-

shaped virtual anode inside the cathode grid. The magnitude of the asymmetries in the model is determined using the variations in the vacuum fields given by superposition of the fields generated by the longitudinal loops of the cathode grid [as described in Section 5.3, Eq. (5.1)]. The model potential also accounts for Debye shielding of the cathode near the grid wires.

The average radius of closest approach, $\langle r_i \rangle$, of 2500 test particles determines the converged core size and is defined for each transit i of the ions through the core region. The resulting average core size, $\langle r_c \rangle$, is then obtained by averaging over all transits weighted by the fraction of particles making the particular transit (N_i):

$$\langle r_c \rangle = \frac{\sum_i N_i \langle r_i \rangle}{\sum_i N_i} \quad (5.3)$$

where i is the transit number index. The results of such calculations for the 27 mPa, 5.0 kV, 20 mA case studied in Ch. 5.3 are shown in Fig 5-9. The values of $\langle r_i \rangle$ for the test ion population is plotted as a function of the number of transits through the core, and for comparison, the ideal geometric core size, the measured core radius, and $\langle r_c \rangle$ are also included in Fig. 5-9.

As expected, the average core size increases with the number of transits, confirming that the grid asymmetries rapidly defocus the ion trajectories. The convergence also rapidly degrades from the ideal convergence expectation as the number of passes through the system increases. In addition, $\langle r_i \rangle$ approaches the measured core size as the number of transits through the core region approaches the experimental recirculation factor ($\xi = 8.6$). In all cases studied, the simulation predicts either a smaller or equivalent core size compared to experiment, and therefore this single particle orbit estimate is consistent with the measured

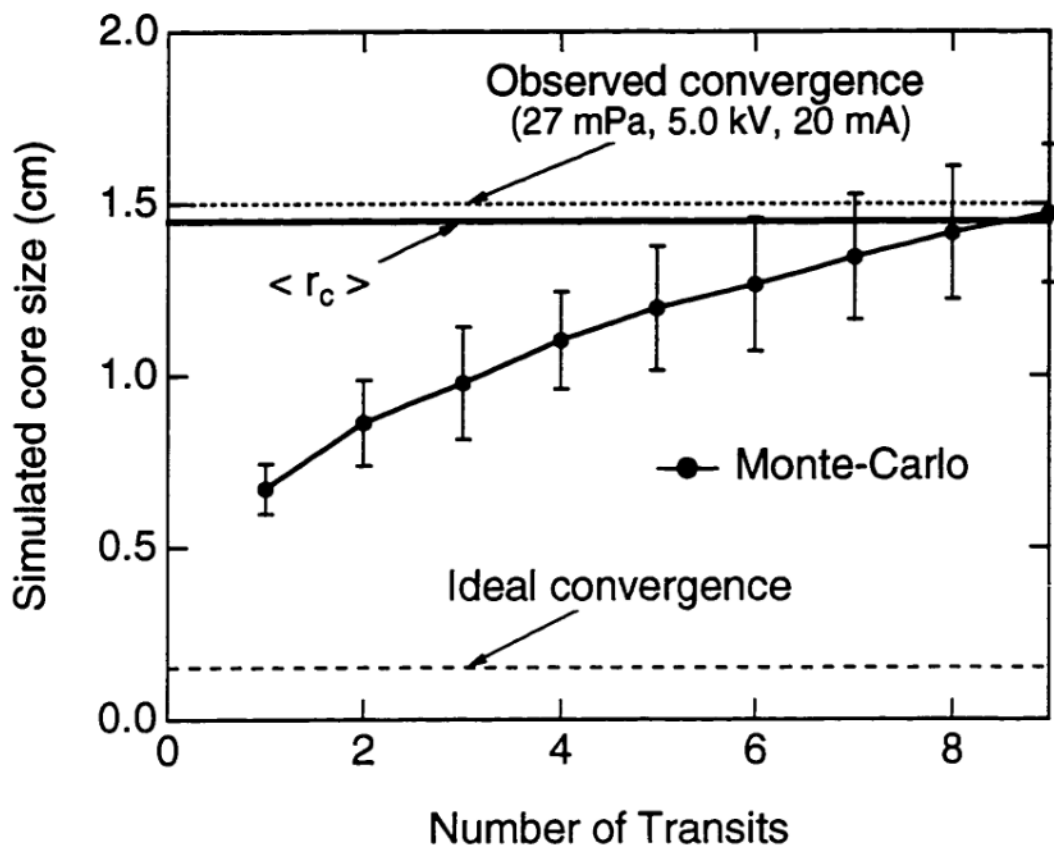


Figure 5-9. Core size estimates versus the number of transits through the core region derived from Monte-Carlo simulations of ion trajectories in a two-dimensional asymmetric well. Included are the ideal convergence estimate and the observed core size for the 27 mPa, 5.0 kV, 20 mA ion flow.

core size, given the observed equilibrium potential structure in the core region and the asymmetries in the accelerating potential well.

To further confirm the effect of the accelerating potential well symmetry on convergence, the results of Monte-Carlo simulations for three different cathode grid wire spacings are shown in Fig. 5-10. The simulations predict smaller core sizes with reduced grid spacing, which was also observed experimentally [c.f. Fig. 5-6(a)].

However, the experiments using the 15, 30, and 45° grid spacings did not keep the grid transparency constant ($\eta = 0.85, 0.91$, and 0.94 respectively), and the resulting change in the recirculation factor also influences the flow convergence by changing the average number of transits an ion makes through the asymmetric fields. The simulation then predicts that $\langle r_c \rangle = 0.6, 1.0$, and 1.4 cm for the 15, 30, and 45° spacing grids respectively (see Fig. 5-10), which is consistent with the variations seen experimentally [c.f. Fig. 5-6(a)].

The simulation results in Fig. 5-10 suggest that each of these effects contributes equally to the predicted core size variations. Therefore, it is the combination of the improved well symmetry with decreasing grid spacing and the reduced recirculation factor from the decreased grid transparency that accounts for the observed dependence of the flow convergence with the cathode geometry.

This collisionless model neglects the effects from neutral interactions, but a significant decrease in core radius is observed with increasing neutral pressure [c.f. Fig. 5-6(b)]. Indeed, experiments performed by Miley, *et al.* reported that the tighter ion focuses were qualitatively observed in the higher-pressure “star” mode of operation^{2,3}.

This is also true for the WISCIF device, and emissive probe measurements made in a star mode indicate quite a different radial potential distribution than the converged-core modes discussed above (See Fig 5-11). The floating and plasma potentials are basically equal

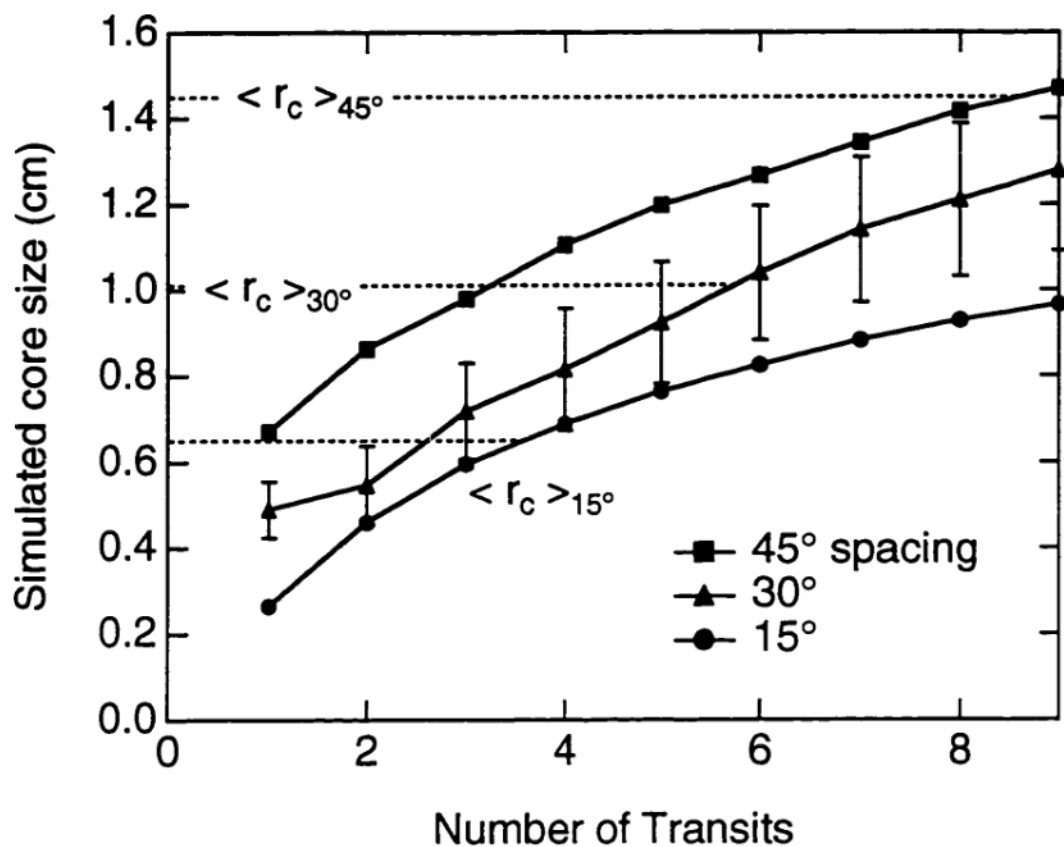


Figure 5-10. Core sizes calculated from the Monte-Carlo ion trajectory simulations for 15, 30, and 45° cathode grid spacings. Included are the estimates of $\langle r_c \rangle$ calculated from Eq. (5.3) using the experimental cathode transparencies for determining N_i .

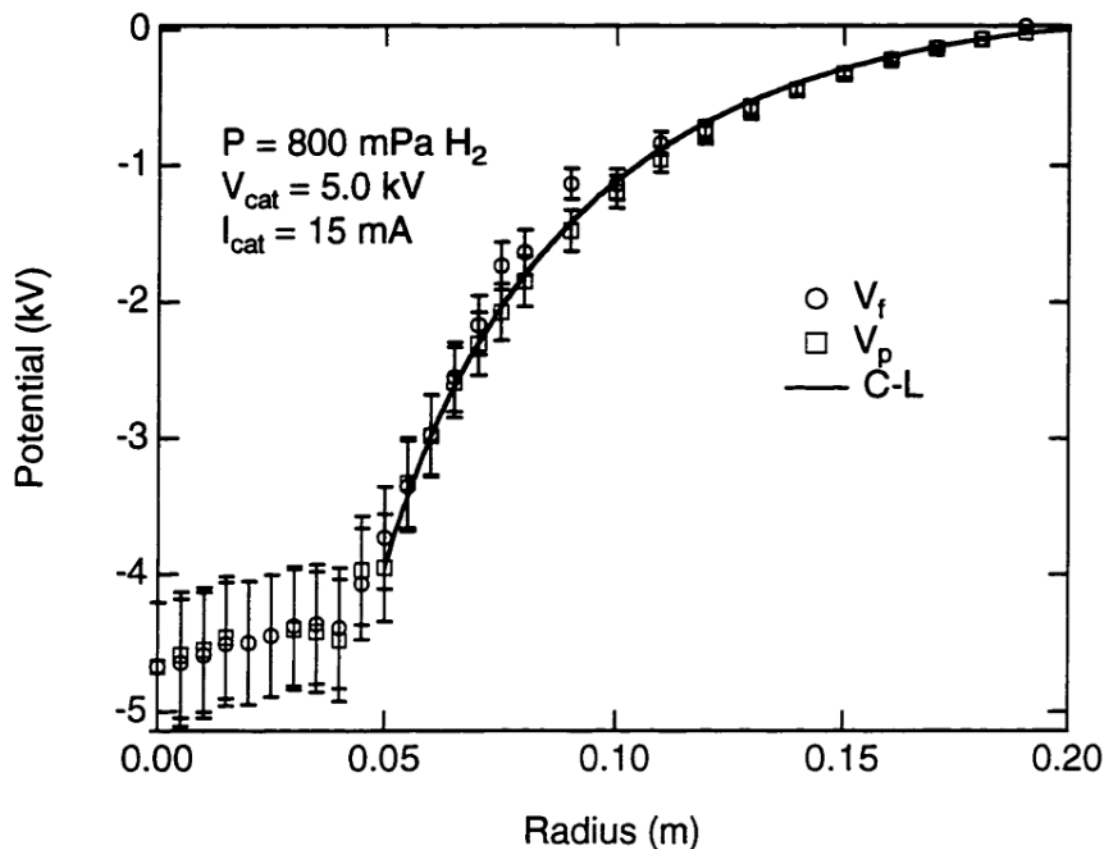


Figure 5-11. Radial electrostatic potential distribution of a star mode.

throughout the profile, which indicates a higher electron density. The depth of the well is also deeper, and there is no evidence of a virtual anode formation in the core region. This alone may account for the observed improvement in convergence, but ion-neutral collisions may also affect the overall convergence.

For example, if ion-neutral collisions remove a fraction of the recirculating ions from the system (*e.g.* via charge-exchange), then the effective number of transits through the asymmetric fields would be reduced, and the Monte-Carlo simulations suggest that a smaller core size would then be expected (See Fig. 5-9).

The effective system transparency against charge-exchange collisions, defined as the percentage of the ion flow that does not charge-exchange on its transit to the core, ranges from 0.97 - 0.95 for the experimental conditions studied in the converged core mode (13 - 27 mPa)⁶. The estimated recirculation factor stays relatively constant between the 13 and 27 mPa, 20 mA cases (See Table 5-1), which confirms that charge-exchange does not reduce the overall system transparency for these low pressure conditions.

The star mode is different, for charge-exchange collisions dominate the ion-cathode grid losses. This would significantly reduce the amount of recirculating ion current, resulting in smaller converged-core sizes. Indeed, the recirculation factor estimated for the potential profile shown in Fig. 5-11 (as calculated before in Section 5.2) is only 4.7, which is much lower than the values given by the lower pressure cases (≈ 7.5). The observed convergence (from CCD measurements, $r_c = 0.7$ cm for a 30° spacing grid) is also consistent with the estimates from the Monte-Carlo simulations if only 3-4 passes through the cathode are allowed.

It is also possible that after gaining significant angular momentum from the asymmetries in the accelerating well, ions may then collide with neutrals at the edge radial

turning points. This would help thermalize the ion distribution there, and the resultant reduction of the ion angular momentum allows each transit of the ion through the core to appear as an undisturbed first transit. The experimental edge collisional mean-free-paths are consistent with this argument for the pressure ranges studied ($\lambda = 25 - 50 \text{ cm}$)⁶. However, further experimental evidence (*e.g.* measurements of the perpendicular ion temperature versus pressure) is needed to confirm the relevance of this effect.

In present gridded systems, convergence is not important since beam-background fusion reactions dominate the reactivity of these devices, as evidenced by the linear scaling of neutron production rate with the cathode current¹⁻³. In fact, convergence may reduce the reactivity by forming a virtual anode that reduces the energy, hence decreasing the probability for fusion, of the ions at the center. However, good convergence is required to achieve optimal beam-beam reactivity scaling for the applications that require higher fusion reaction rates, and the importance of symmetry in determining convergence places a constraint on any SCIF device planned for these applications. The observed loss of convergence with decreasing pressure and increasing current makes achieving significant beam-beam scaling far less accessible.

A single virtual anode was measured by the emissive probe in the core region, but no evidence of multiple well structures was observed in the WISCIF experiments under the ion-dominated, low-pressure conditions discussed here. As mentioned earlier, some computer simulations, performed by other investigators, show multiple-well formation, but these models assumed perfectly symmetric accelerating potentials^{1,14}. However, the experiments indicate that any detailed potential structure near $r = 0$ would be washed out due to the angular momentum of the ions gained from the asymmetries in the accelerating region.

Presumably, the virtual anode near $r = 0$ can act as an efficient trap for warm electrons, and it may allow the trapped electrons to be heated to temperatures on the order of the anode height (shown in Fig. 5-3 as the difference between the potential at $r = 0$ and the most negative potential inside the cathode) via electron-ion collisions. However, the measured probe floating potentials were more positive than the plasma potential, which signifies that the local ion current to the probe is larger than the electron current at the plasma potential. Any hot electron population must be of much lower density than the local ion density for I_e to remain less than I_i at the plasma potential.

While these experiments were carried out at lower voltages and densities than needed for applications, it is at low voltage (high-perveance) where the ion space-charge effects would be most prevalent. These results at low pressure indicate that the generic ion flow behavior is essentially collisionless and classical at the conditions studied.

5.6 REFERENCES

- ¹R. Hirsch, J. Appl. Phys. **38**, 4522 (1967).
- ²G. H. Miley, J. Nadler, T. Hochberg, Y. Gu, O. Barnouin, J. Lovberg, Fusion Technol. **19**, 840 (1991).
- ³J. H. Nadler, G. H. Miley, Y. Gu, and T. Hochberg, Fusion Technol. **21**, 4140 (1992).
- ⁴T. J. Dolan, Plasma Phys. Controlled Fusion **36**, 1539 (1994).
- ⁵R. L. Freeman and E. M. Jones, Culham Laboratory Report #CLM-R137 (1974).
- ⁶R. K. Janev, W. D. Langer, K. Evans, Jr., and D. E. Post, Jr., *Elementary processes in Hydrogen - Helium Plasmas*. Springer-Verlag, Berlin (1987).
- ⁷S. C. Brown, *Basic Data of Plasma Physics*, (M.I.T. Press, Cambridge, 1967).
- ⁸N. Hershkowitz, in *Plasma Diagnostics*, edited by O. Auciello and D. L. Flamm (Academic Press, Boston, 1989), p. 176.
- ⁹The secondary electron emission coefficient, δ , is estimated by comparing the values of δ_e for a variety of metals listed in E. W. Thomas, ed. Oak Ridge National Laboratory Report #ORNL-6088 (1985).
- ¹⁰N. A. Krall, Fusion Technol. **22**, 42 (1992).
- ¹¹The edge perpendicular temperature is estimated to be 0.1eV for these calculations, which is a typical ion temperature for this type of glow discharge. B. Chapman, *Glow Discharge Processes* (John Wiley & Sons, New York, 1980), p. 52.
- ¹²J. D. Jackson, *Classical Electrodynamics* (John Wiley & Sons, New York, 1978), p. 93.
- ¹³Emissivity of alumina is estimated using the value for fire brick from the *Handbook of Chemistry and Physics*, 71st ed., edited by D. R. Lide, (CRC Press, Boston, 1990), p. 10-282.
- ¹⁴B. E. Cherrington, J. T. Verheyen, and D. A. Swanson, Ann. NY Acad. Sci. **251**, 139 (1975).

Chapter 6: Fusion Reactivity Experiments

Measurements of the fusion production rates in past SCIF-type experiments have not produced a clear understanding of the underlying mechanisms that determine the system reactivity, as inconsistent performance and scalings were observed between experiments¹⁻⁶. Different (and conflicting) hypotheses were developed to explain the various observations (See Chapter 3), but the basic sources of fusion reactivity observed in low-power experiments to date remain experimentally unexplored and hence unexplained. Therefore, it has been difficult to accurately extrapolate the reactivity of SCIF-type devices to determine their viability for applications.

To resolve some of these issues, we report here results of new and extensive experiments aimed at determining the source of the D-D fusion reactivity for a gridded SCIF device. Again, the sources of reactivity considered include beam-beam, beam-background, beam-cathode, and fast-neutral-background collisions, where beam indicates the primary fast ions accelerated by the spherical potential well, background indicates the cold neutral fill gas atoms or molecules, cathode indicates the trapped fuel density at the cathode surface, and fast-neutral indicates energetic neutral atoms produced by charge-exchange reactions between the beam ions and the background gas.

Experiments designed to distinguish the different sources were performed using deuterium for cathode voltages up to 60 kV, cathode currents up to 250 mA, and with a steady-state cathode power up to 6 kW. The systematic dependencies of the fusion neutron production rate with cathode voltage, current, neutral pressure, and cathode geometry

(transparency, symmetry, and size) were obtained by neutron count rate measurements, and the spatial distribution of the fusion reactions was determined using a collimated fast-proton detector. A fluid-flow model, with charge-exchange production of energetic neutrals, was also developed to provide a reasonably quantitative accounting of the measured neutron production.

This chapter first reviews the results from the reactivity measurements, and a detailed description of the charge-exchange flow model then follows. A comparison of the experimental reactivity measurements to this model and the various hypotheses discussed in Chapter 3 are then discussed.

6.1 REACTIVITY MEASUREMENTS

6.1.1 Cathode power and neutral pressure scalings

To evaluate the suitability of these devices for applications, the dependence of the fusion reactivity on input power must be well understood. Observations of the systematic dependencies of the fusion reaction rate also provide insight into which sources of reactivity are dominant. For example, beam-beam reactions would scale as I_{cat}^2 and with a different voltage and pressure dependence than beam-cathode or beam-background, which increase linearly with I_{cat} [See. Eqs. (2.1) and (2.20)].

Figure 6-1(a) shows a representative cathode voltage scan, where the measured steady-state system neutron production rate (*NPR*) scales simply with the energy dependence of the D-D fusion cross section [i.e. $NPR \propto \sigma_{fus,DD}(E_i)$] between 20 and 60 kV. This observed scaling is consistent with past gridded-cathode experiments performed in this voltage range at lower densities and power¹⁻⁴.

In Figure 6-1(b), the *NPR* shows a linear dependence on cathode current up to the maximum 250 mA for a variety of pressure ranges. The higher pressure discharges ($P > 100$

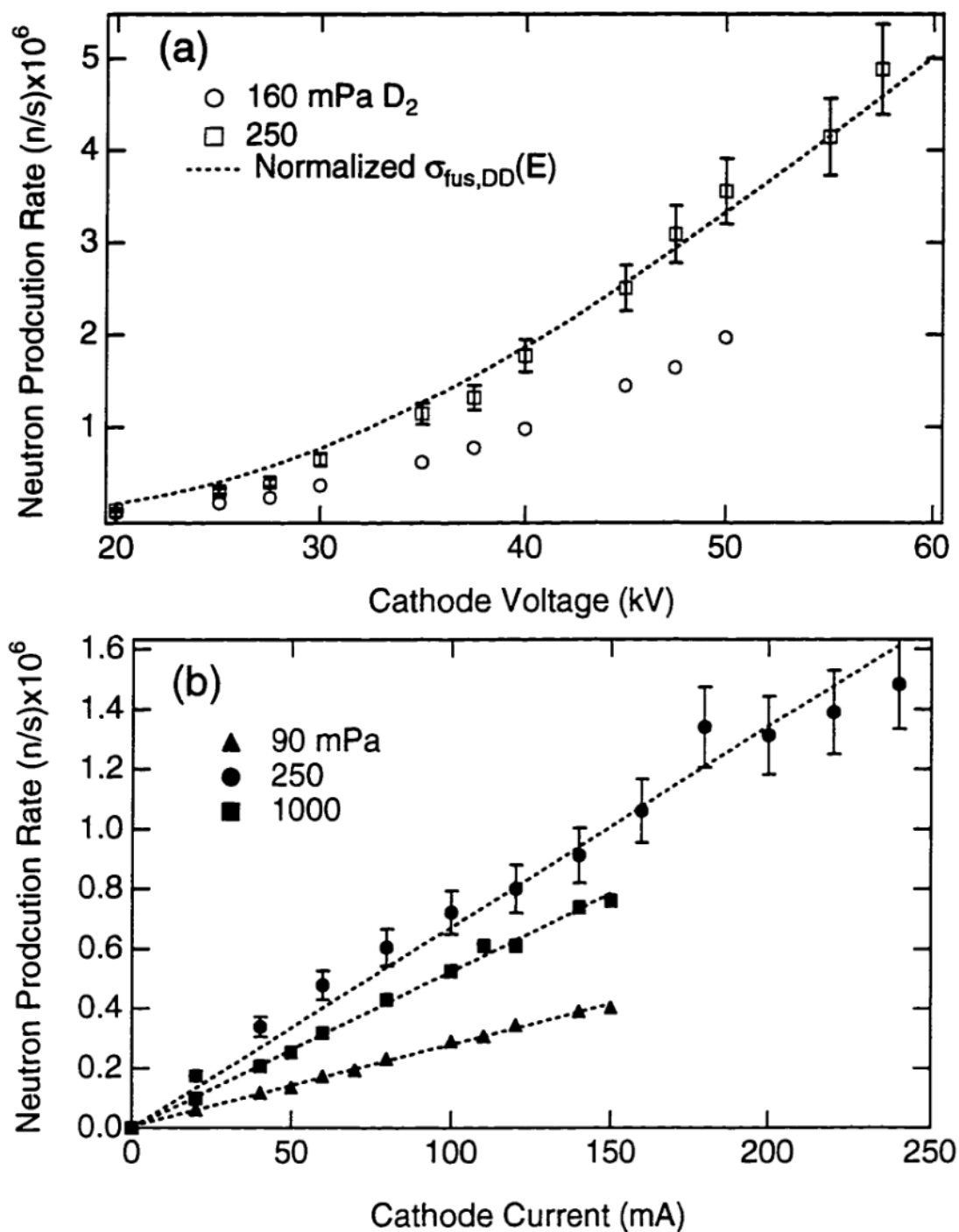


Figure 6-1. Total neutron production rate variations with (a) V_{cat} and (b) I_{cat} for the deuterium neutral pressures listed. In (a), $r_{cat} = 0.05$ m, $I_{cat} = 20$ mA, and for (b), $r_{cat} = 0.10$ m, $V_{cat} = 20$ kV.

mPa) are similar to the “star” modes studied at lower density by Miley, *et al.*, where a self-sustaining, normal glow discharge persists¹⁻⁴. To operate at pressures below 100 mPa, the edge plasma source is required to sustain the ion flow, and a “converged–core” mode persists (See Section 5.1). While the discharge characteristics are different, the *NPR* is also found to scale linearly with current in this regime.

These cathode current and voltage scalings are consistent with the energetic particles fusing mainly with a background neutral density, as opposed to the counter-streaming beams fusing with each other. This is not unexpected considering that the typical neutral densities (~ 10^{19} m^{-3}) are much greater than the expected energetic ion densities (~ 10^{15} m^{-3}).

Given these scalings, one might anticipate that as the neutral background density increases, the fusion rate would also increase proportionally [See Eq. (2.20)]. However, this is not seen experimentally, as shown in Fig. 6-1(b), where the 250 mPa case indicated a higher *NPR* than the 1000 mPa case. Figure 6-2 shows a composite pressure scan, where many *NPRs* from different operating cathode voltages and currents are compared by normalizing out their known dependencies on the fusion cross section and supply current. An increase in the normalized *NPR* is observed up until about 300 mPa, while a rapid decline is indicated for higher pressures. This is qualitatively similar to the pressure scaling observed previously by Miley, *et al.* in a smaller gridded device³. In contrast, Hirsch’s experiment, which utilized ion guns instead of a distributed plasma source, found an monotonic increase in neutron production for decreasing pressure over a similar pressure range (10 - 1000 mPa)⁵.

For comparison, estimates of the reactivity expected from the simple collisionless model [See Section 2.4, Eq. (2.20)] are indicated by the dashed line in Fig. 6-2. At the lower pressures studied, the measured reactivity is a factor of ~ 5 greater than this ideal (and overly

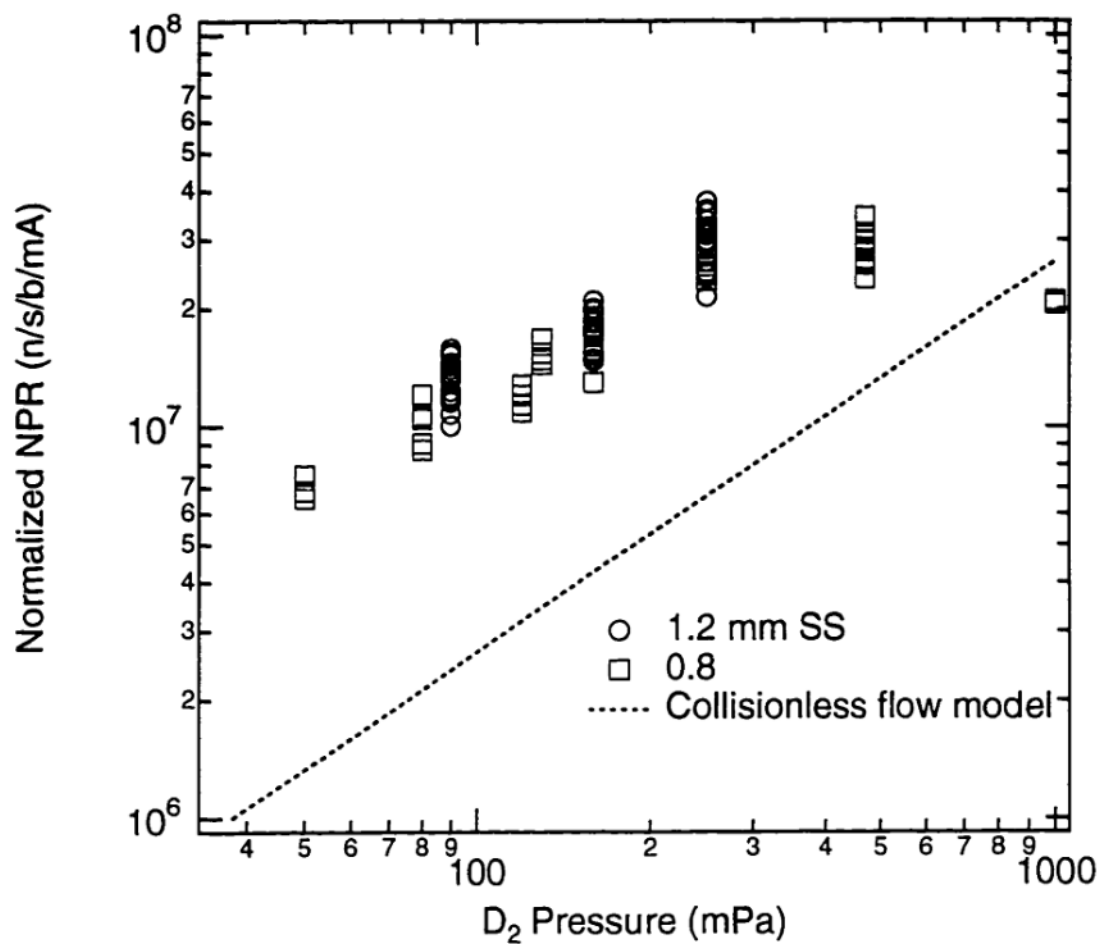


Figure 6-2. Normalized NPR ($= \text{NPR}/\sigma_{fus,DD}/I_{cat}$) scaling with pressure for two 5 cm radius cathodes with 22.5° wire spacing and different wire thicknesses (and hence different transparencies). Also included is the collisionless flow model estimate assuming $\delta = 1$, $\eta = 0.91$.

optimistic) estimate. The collisionless estimate also does not reflect the observed pressure dependence.

6.1.2 Spatial Distribution of Fusion Reactivity

The spatial distribution of the fusion reactivity provides distinction between the various possible sources of reactivity. For example, if ions dominate the reactivity, a highly localized source near the origin would be expected. In contrast, a fast-neutral-background dominated system would have a peaked, but far more diffuse spatial distribution.

The various hypotheses discussed in Chapter 3 (*i.e.* multiple-well, charge-exchange, beam-cathode) also suggest radically different spatial distributions. The multiple-well hypothesis predicts a highly localized source of reactivity near the origin of the system, the charge-exchange model predicts a peaked but rather broad reactivity distribution, and the beam-cathode contribution is localized at the cathode surface. In addition, the beam-cathode and charge-exchange reactivity should be rather insensitive to the cathode grid spacing and transparency. In contrast, the multiple-well model is very sensitive to the degree of focusing and the amount of recirculating current, and hence should depend strongly on cathode spacing and transparency.

Measurements of the fusion production spatial distribution are provided by the collimated proton detector, and the fusion proton signal versus chordal height from the origin for a 35 kV, 20 mA discharge in 250 mPa of deuterium is shown in Fig. 6-3(a). While the proton signal intensity is peaked near the center, it is important to note the detectable, non-zero signal observed outside the chordal height of 0.05 m, which is the cathode radius. This signal originating outside the cathode gives rise to the majority of the total fusion production due to the larger volumes at large radii.

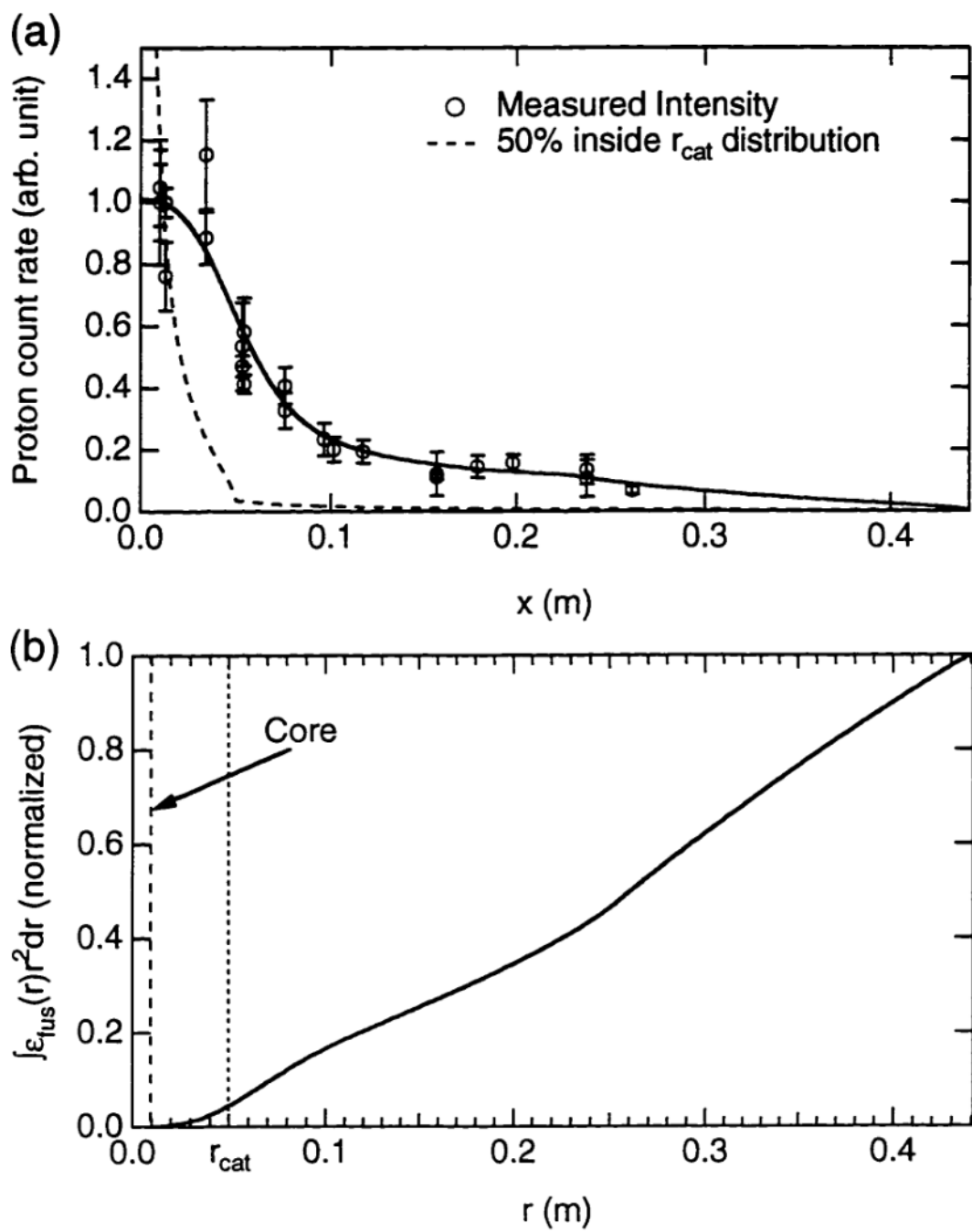


Figure 6-3. (a) Proton collimation measurements and (b) the integral of the resulting Abel-inverted radial reactivity profile, $\epsilon_{fus}(r)$. Included in (a) is the expected proton intensity distribution if 50% of the total system fusion production were generated inside the cathode ($r_{cat} = 0.05$ m).

This is seen in Fig. 6-3(b), which shows the local reactivity, $\epsilon_{\text{fus}}(r)$, volume-integrated to a given radius r as a function of r , to give the total reaction rate occurring inside r . It is apparent from Fig. 6-3(b) that > 90% of the total reaction rate originates outside the cathode radius of 5 cm. Hence, almost all of the fusion reactions are not occurring in the converged ion core region, but outside of it, suggesting an extended, non-local source. To emphasize this point, Fig. 6-3(a) includes the shape of the curve expected from the proton collimation scan if only 50% of the integrated system reactivity is originating inside the cathode radius, much less inside the condensed ion core region ($r_{\text{core}} \sim 1 \text{ cm} < r_{\text{cat}}$). The data clearly indicates a much broader radial distribution of the reactivity.

The local reactivity [$\epsilon_{\text{fus}}(r)$] is derived from an Abel inversion⁷ of the spline-fitted data in Fig. 6-3(a), assuming that the chordally integrated reactivity decreases as $1/r^2$ outside the outermost grid ($r = 0.2 \text{ m}$). This is equivalent to assuming that no source of fast ions or neutrals exists outside the outermost grid. While the exact form of $\epsilon_{\text{fus}}(r)$ from the Abel inversion is fairly sensitive to the edge conditions assumed, the integrated system reactivity [shown in Fig. 6-3(b)] is not, especially inside the cathode region. Therefore, the proton collimation data is consistent with a diffuse source of reactivity.

6.1.3 Cathode grid geometry scalings

In order to study the influence of flow convergence and the cathode geometry on the system fusion production, the cathode transparency, mesh spacing, and size is varied. An increased mesh spacing leads to a more defocused flow, as the asymmetries in the accelerating potential are larger (See Section 5.3). This is expected to have little effect in beam–background dominated systems, unless the ion–confinement time is somehow related to the flow convergence, as predicted in the multiple–well model. Decreasing the transparency of the cathode limits the ion lifetime of the system (assuming collisionless ion

flow and losses only to the grid) and would be expected to significantly reduce the efficiency and fusion production of the system. By increasing the cathode size, the path length of the high-energy region increases, and therefore an enhancement to the system fusion reaction rate may then be expected as well.

The effects of the cathode grid spacing on the *NPR* are shown in Fig. 6-4(a), where comparisons of cathodes of similar transparency but different wire spacings are shown. No variation of the *NPR* is observed between cathodes of 22.5° and 45° grid spacings for pressures down to 50 mPa. Studies with 85% transparent grids similarly find no significant differences between cathodes of 15° and 22.5° spacings. However, the flow convergence, discussed in Section 5.3, did depend strongly on the cathode wire spacing (See Fig. 5-6). Therefore, it appears that the cathode geometry (or degree of flow convergence) has little effect on the overall system *NPR*.

By keeping the grid spacing (i.e. the total number of grid wires) constant, the transparency of the grid is varied by changing the diameter of the grid wires used. In Fig. 6-2, two different cathode wire thicknesses are compared, and between 50 and 250 mPa, no significant difference is observed in the *NPR* for these two different cathodes. Figure 6-4(b) includes a similar comparison at 250 mPa for a 45° spacing cathode. No significant variation in the *NPR* is observed for changes in the grid transparency between 85 and 96%, where Eq. (2.20) predicts almost a factor of three difference in R_{fus} .

Variations in the cathode size did produce a observable variation; Figure 6-5 includes a voltage scan at 250 mPa (20 mA cathode current), where grids of 2.5, 5, and 10 cm radius are compared ($\eta = 0.91\text{--}0.92$). Little change was observed between the 2.5 and 5.0 cm cathodes, but a factor of ≈ 1.5 increase was measured between the 5 and 10 cm radius cathodes.

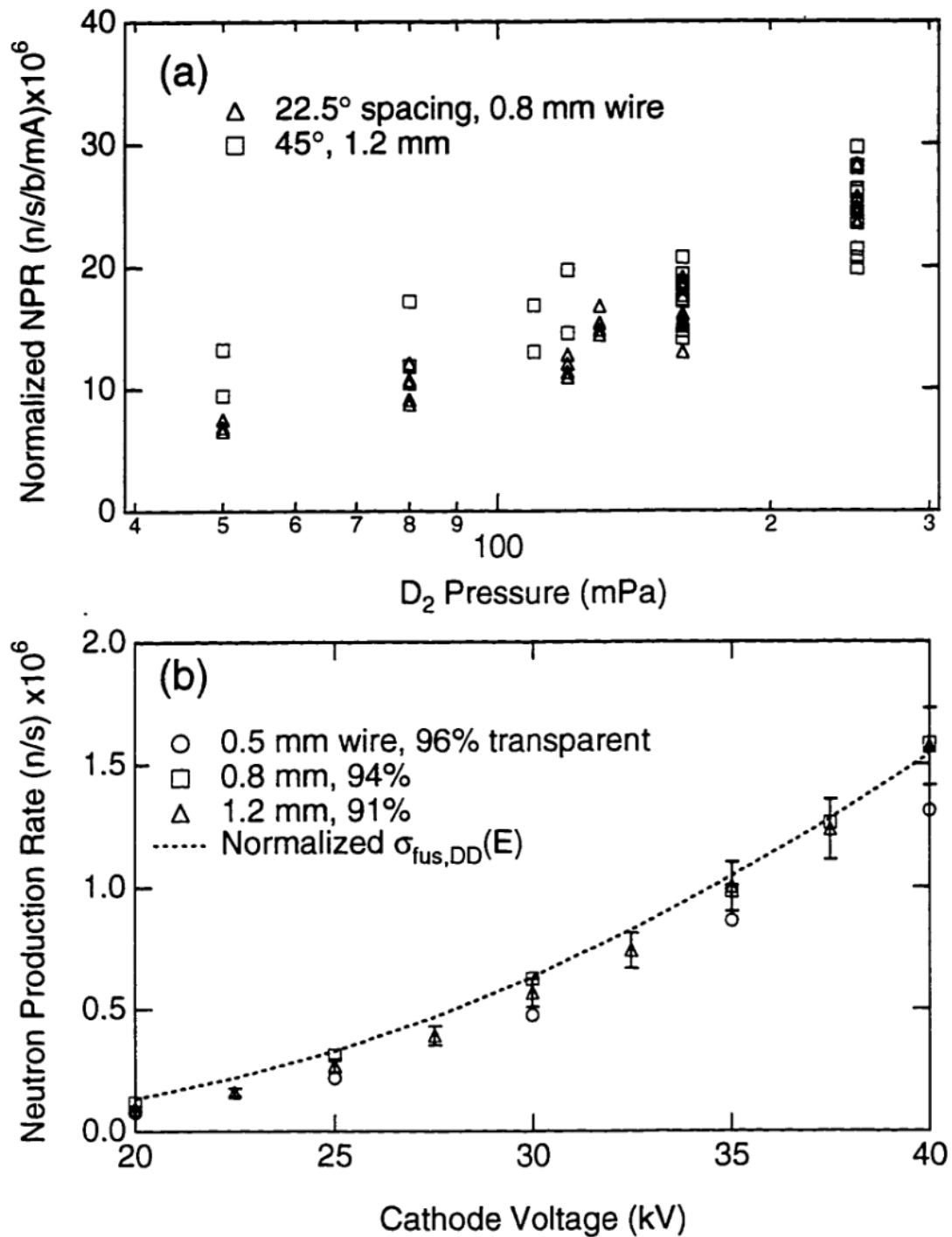


Figure 6-4. The measured *NPR* for cathodes with (a) 91% transparency using 22.5° and 45° grid wire spacing and (b) varying cathode wire thicknesses and hence transparencies at 20 mA and 250 mPa for a 45° spacing grid.

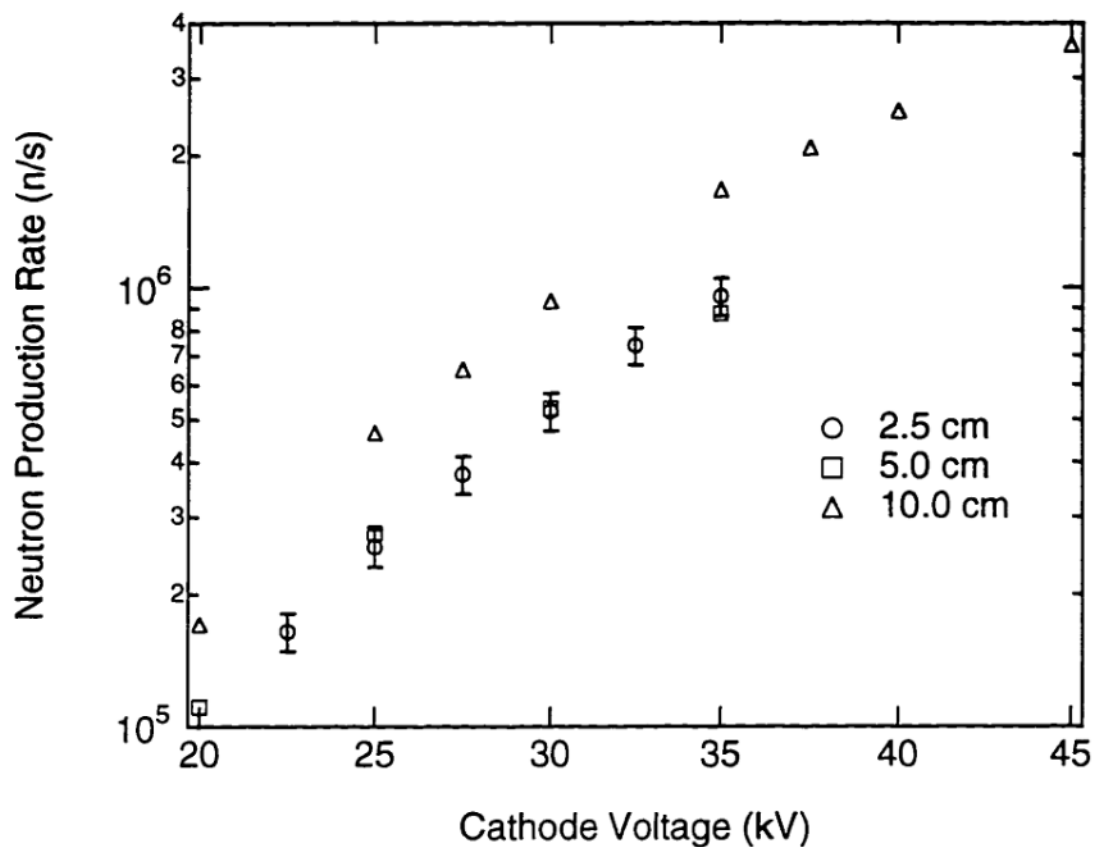


Figure 6-5. Neutron production rate versus cathode voltage for cathode radii of 2.5, 5.0, and 10.0 cm at $I_{cat} = 20$ mA and $P = 250$ mPa.

6.1.4 Cathode contribution to the system fusion production

The cathode grid itself, due to the constant bombardment of energetic ions onto the wire surface with its trapped fuel density, is potentially a significant source of fusion production. To examine this possible source, a solid, 2.5 cm radius sphere and grids of different materials were installed as the high-voltage cathode.

The solid cathode produces gradually increasing reactivity for decreasing pressure, as the NPR increased by at most a factor of 2 as P ranged from 1000 mPa down to 50 mPa. This is presumably due to the collisional degradation of the ion distribution from ion–neutral collisions. At the higher pressures, the solid target reactivity is ≤ 0.1 of the total measured with the gridded system, indicating that beam-grid collisions constitute a relatively small fraction of the NPR there. However, at the lowest pressure, the beam-sphere contribution is ~ 0.6 of the total measured in the gridded system, and it can even surpass the values expected from the ideal, collisionless flow model.

Different cathode materials are also of interest, and the resultant $NPRs$ of cathodes constructed of W, Ti, and stainless steel are included in Fig. 6-6. Each material has much different trapping properties and hence different values of K_r at lower temperatures. However, for the conditions studied, typical grid wire temperatures of ~ 2000 K are expected (See Section 6.2 below), where all three materials have similar K_r properties⁸. Indeed, the data in Fig. 6-6 show little difference in the NPR between the various materials.

6.2 ANALYSIS AND DISCUSSION

Neutron count rate measurements versus the neutral gas fill pressure indicate that ion–neutral collisions play a significant role in determining the system reactivity, and the dominant collisional process for the energy ranges considered is charge–exchange. This is shown in Table 6-1, which compares the various relevant collision rates for different spatial

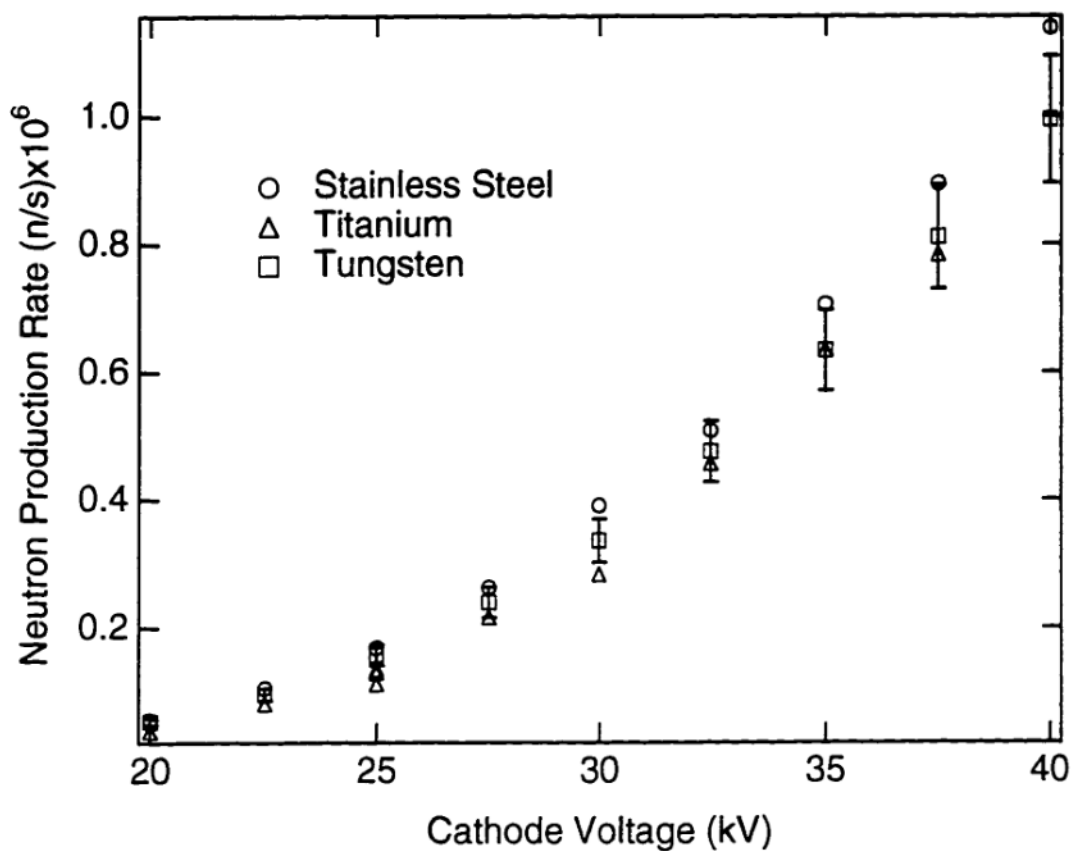


Figure 6-6. Neutron production rate for cathodes of differing materials at 20 mA and 250 mPa. The 5.0 cm radius cathodes had a 45° spacing using 0.5 mm diameter wire.

regions in the ion flow for a typical WISCIF discharge^{9,10}. Charge-exchange is the dominant process in the high energy regions and even dominates over ion-cathode collisions at all but the lowest pressures.

Collision Type	Edge ($r > r_{\text{anode}}$)	Acceleration ($r_{\text{anode}} > r > r_{\text{cat}}$)	Core/Plateau ($r_{\text{cat}} > r$)
Charge- Exchange	7×10^3	3×10^6	4×10^6
Neutral Elastic Scattering	2×10^5	10^5	10^5
Ionization	~ 0	$\sim 10^{-2}$	20
Ion-Ion Scattering	2	7×10^{-6}	4×10^{-4}

Table 6-1. Comparison of various collision rates (all values listed are proportional to pressure and have units of s^{-1}) in different regions of the ion flow for typical operating parameters (35 kV, 20 mA, $P = 130$ mPa)^{9,10}. The effective ion cathode collision rate is $\sim 2 \times 10^6$ /s.

The proton collimation measurements suggest the importance of the fast neutrals since a significant amount of the fusion reactions are generated outside the cathode region. For a charge-exchange dominated system, the cathode transparency or grid spacing would not be expected to affect the system fusion production rate. since the resultant *NPR* is relatively unrelated to the condensed core plasma properties. Indeed, experimental measurements of the *NPR* for various materials, grid spacings, and transparencies find no significant changes in the system fusion production rate.

Therefore, a fusion reactivity model for SCIF-type devices would need to account for the fast-neutral-background contribution. To estimate this contribution for the WISCIF

device, a classical fluid-flow model calculation was developed that included charge-exchange collisions. The number of fast ions removed from the ion flow via charge-exchange as it evolves through the mantle, plateau, and core regions is calculated from the ion fluid continuity equation (assuming steady-state flow):

$$\nabla \cdot \frac{d\Gamma_i(r,E)}{dE} = \frac{1}{r^2} \frac{d}{dr} \left[r^2 \frac{d\Gamma_i(r,E)}{dE} \right] = - n_o \sigma_{cx}(E) \frac{d\Gamma_i(r,E)}{dE} \quad (6.1)$$

where n_o is the neutral background gas density, $d\Gamma_i(r,E)/dE$ is the differential radial ion flux as a function of radius and energy, and $\sigma_{cx}(E)$ is the energy-dependent charge-exchange cross section. Here, only radial fluxes are considered, and only fusion, charge-exchange, and ion-impact ionization collisions are included in the calculation. The fusion collision rate is small compared to charge-exchange (See Table 6-1), and hence it is ignored in Eq. (6.1). Ion-impact-ionization is assumed to not remove energy from the fast ion flow, and therefore it is also left out of Eq. (6.1).

The fast neutral flux (Γ_n) is calculated similarly as:

$$\frac{1}{r^2} \frac{d}{dr} \left[r^2 \Gamma_n(r,E) \right] = n_o \sigma_{cx}(E) \Gamma_i(r,E) \quad (6.2)$$

and the source for thermal ions is given by:

$$\frac{1}{r^2} \frac{d}{dr} \left[r^2 \Gamma_{ii}(r) \right] = \int_0^{E_{max}} dE n_o (\sigma_{cx}(E) + \sigma_{ii}(E)) \frac{d\Gamma_i(r,E)}{dE} \quad (6.3)$$

where E_{max} is the maximum energy of the ions at the particular radial location [i.e. $E_{max} \approx -\Phi(r)$] and $\sigma_{ii}(E)$ is the ion-impact-ionization cross section.

The electrostatic potential distribution for this model calculation is taken from the spherically symmetric, space-charge-limited model [Eq. (2.19)] between the anode and the cathode, and a flat potential equal to the cathode bias is assumed inside the cathode radius to

provide a best-case estimate. A monoenergetic distribution of ion current is then injected at the edge of the potential well [0.2 m radius for the WISCIF device, i.e. $d\Gamma_i(0.2, E)/dE = \Gamma_{io}\delta(E - E_t)$], where the incident ion flux, Γ_{io} , is related to the measured ion current in the experiment by:

$$\Gamma_{io} = \frac{I_{meas}}{e(1 + \delta_e)(0.2)^2} \quad (6.4)$$

The calculation follows the ion flow through the system by evaluating Eqs. (6.1) - (6.3) for each energy group at every radial mesh location. These locations are chosen outside the cathode to correspond to equal energy steps (*e.g.* $\Delta E = 1.0$ kV), and they are spaced equally inside the cathode ($\Delta r = 0.01$ mm).

The ion population is calculated for many transits through the system, and the fast neutrals from charge-exchange are assumed to travel straight through to the vacuum chamber wall (0.45 m radius assumed). The fusion rate is then calculated from Eq. (2.1) using the resulting ion and fast neutral distributions.

Figure 6-7 shows the radial electrostatic potential distribution for the model (as described above) and the resulting uncollided fraction of ion current [$= n_i(r)v_i r^2$] after a single pass through the system for a 35 kV discharge at 250 mPa (for reference, the radial electrostatic potential distribution for the model is also included in Fig. 6-7). The discontinuities in the ion current at $r = \pm 0.05$ m signify the losses to the cathode grid (*i.e.* the ion and fast neutral densities are multiplied by the geometric cathode transparency, $\eta = 0.91$ for this case). Charge-exchange collisions clearly dominate at these conditions, for over 75% of the original ion distribution is converted to fast-neutrals in a single pass. The model also estimates that the ratio of fast-neutral to fast-ion induced fusion is approximately 2:1 at 250 mPa. Therefore, the fast neutrals are expected to contribute at least twice as much reactivity

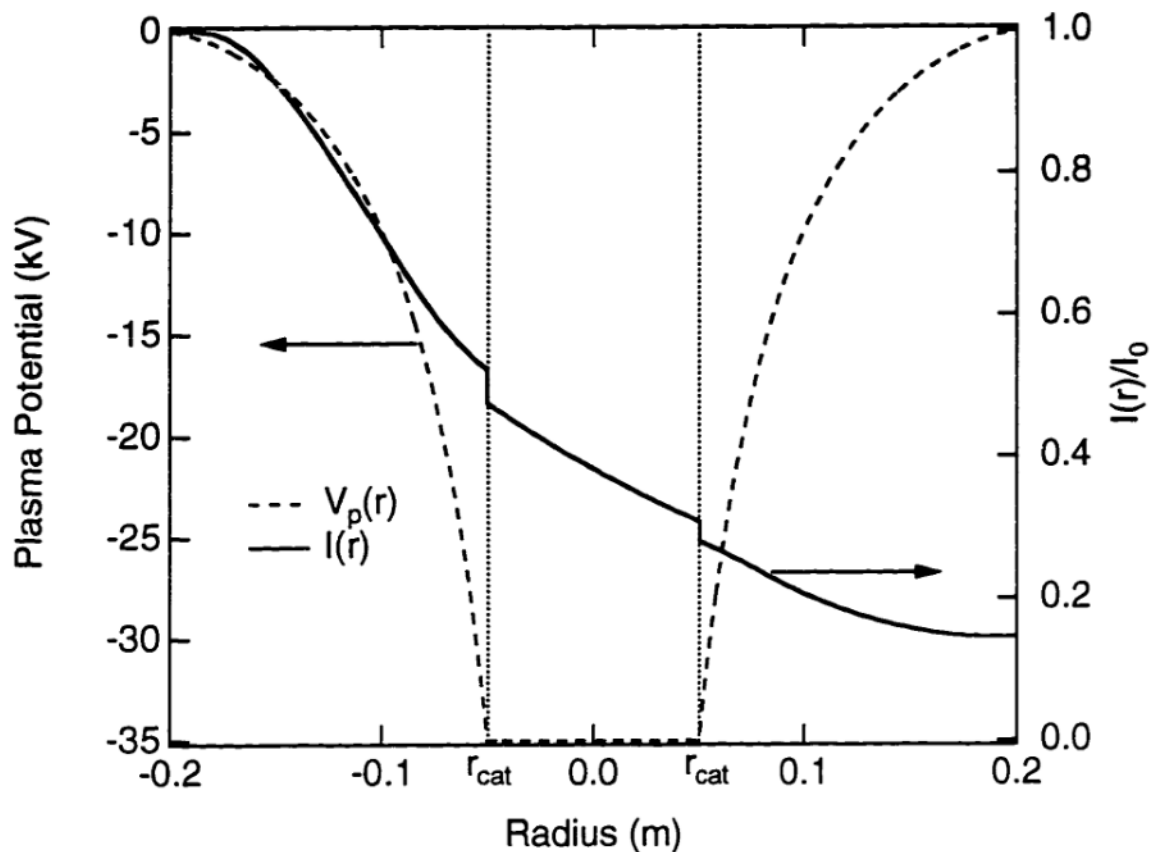


Figure 6-7. The radial electrostatic potential distribution and the resulting uncollided fraction of ion current for a 35 kV discharge at 250 mPa of deuterium. The cathode transparency is 0.91.

as the ions at this pressure. The Abel inversion of the proton signal suggests that even more fusion reactions are generated outside the cathode [See Fig. 6-3(b)].

The pressure scaling of the *NPR* predicted by this charge–exchange model is shown in Fig. 6-8 and is compared to the normalized measurements from a representative gridded cathode experiment. This plot also includes the data from the solid spherical target experiment for comparison (from Section 6.1.4). Also for comparison, the values expected by the collisionless flow model are indicated by the dashed line. A second model plot, where this solid cathode contribution is added to the charge–exchange model reaction rates, is included in Fig. 6-8 (thick line) to provide an upper limit to the expected total *NPR*. This model accurately predicts the peak pressure, and the absolute value of the model *NPR* is consistent with the observed values. The discrepancy at the lowest pressures ($P < 100$ mPa) may be due to a virtual anode formation in the converged core region (See Fig. 5-4). The most significant contribution to the observed *NPR* at these pressures are the fast-ion-background collisions (at 50 mPa, the charge–exchange model predicts the ion contribution to be about 75%), and a virtual anode formation in the core would reduce this contribution by lowering the energy of the ions in the core region.

It is likely that the trapped density of deuterium that is implanted into the cathode is also contributing at those lowest pressure conditions. Equation (2.21) indicates that this trapped density is strongly dependent on the cathode temperature through the dependence on K_r (See Section 2.4.2). The temperature (T) of the cathode ball can be estimated assuming a purely radiative transfer of the input power (700 W) by:

$$P = \frac{I_{\text{cat}} V_{\text{cat}}}{A_{\text{cat}}} = \varepsilon \sigma T^4 \quad (6.5)$$

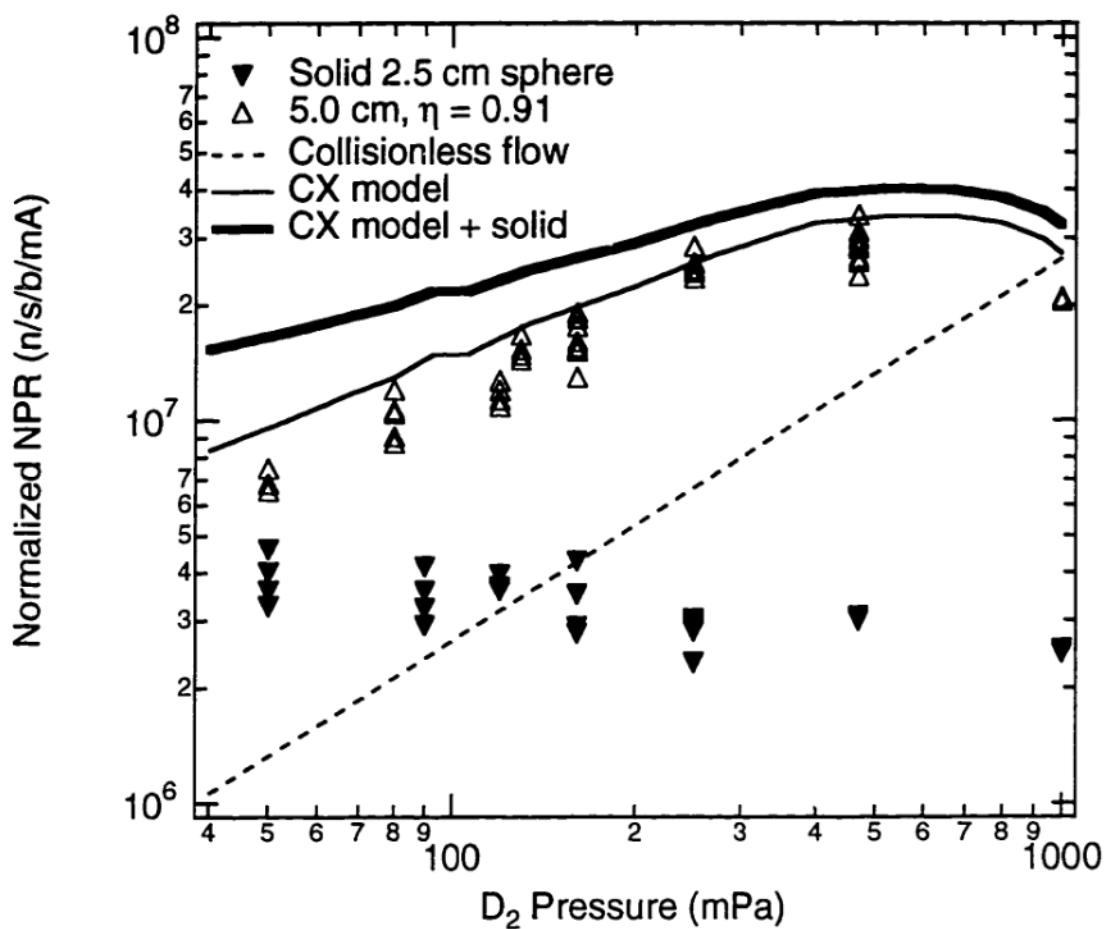


Figure 6-8. Normalized NPR from the charge-exchange fluid model versus pressure compared to gridded cathode measurements. Also included is the measurements from the solid cathode (2.5 cm radius) and the estimate from the collisionless flow model.

where ϵ is the emissivity of the stainless ball, σ is the Stefan–Boltzmann constant. Taking $\epsilon = 0.35$, the estimated cathode temperature is ≈ 1000 K, and experimental measurements of K_r at 1000 K range between 2×10^{-31} and $2 \times 10^{-27} \text{ m}^4/\text{s}$ ^{8,11}. By taking the lowest value of K_r , an upper limit to the trapped cathode density is given, and by Eq. (2.21), this trapped density for the solid cathode studied is $6 \times 10^{24} \text{ m}^{-3}$ (if $\delta = 1$, then $I_f = 10 \text{ mA}$). Assuming λ is $\sim 1 \mu\text{m}$ and the fast particle current into the cathode is monoenergetic (in this case at 35 kV), the beam–cathode contribution estimated from Eq. (2.22) is $\approx 10^5 \text{ /s}$, which is equal to the measured value with the solid sphere.

Since the beam–cathode fusion production rate is a function of fast particle current (and not current density), the contribution for the semi-transparent grids should be similar. However, the cathode area is different, and therefore the gridded cathodes operate at higher temperatures than the solid sphere (for like conditions). The resulting K_r constant would be higher⁸, and therefore, the solid sphere estimate should provide an *upper limit* to the possible cathode contribution.

The observed cathode-size scaling of the *NPR* is also consistent with the charge-exchange model, for while the fast-neutral (produced by charge-exchange) contribution would remain approximately constant for the three different cathode sizes studied (See Fig. 6-5), the fast ion contribution is directly related to the cathode size. If the ratio of fast-neutral to fast-ion fusion is 2:1 for a 5 cm radius cathode at 250 mPa, then 33% of the system *NPR* is due to ions. By this analysis, a 33% improvement is expected for the 10 cm cathode ($\sim 50\%$ is indicated), and only a 16% decrease is expected for the 2.5 cm radius cathode, where no noticeable difference is measured. While this does not completely explain the observed cathode size scaling, it is not entirely unexpected given the experimental uncertainties, that the calculated distributions from the flow model are only approximate, and that the effective fast neutral path length is not exactly constant for the three cathodes.

These results are in complete contradiction to the multiple-well model, which predicts that the reactivity is localized within the cathode region. Flow convergence is also important in setting up the tight potential structures near the core, and the ion recirculation should have a linear effect on the system fusion production rate. However, these effects are not observed, and one may thus argue that the presence of multiple-well structures in a gridded system would be extremely unlikely.

While this classical, charge-exchange flow model successfully describes the *NPR* observed in a gridded SCIF device, it does not completely account for the even higher *NPR* reported originally by Hirsch⁵ from the ion gun experiment. However, subsequent ion gun experiments did not achieve the same performance as Hirsch⁶, and the measured *NPRs* from these later experiments are in better agreement with the charge-exchange dominated flow model predictions described here. Hirsch's results initiated much of the interest in SCIF-type devices, and a repeat of the ion gun experiments may be required to resolve the discrepancy between the different experiments.

6.3 REFERENCES

- ¹J. H. Nadler, G. H. Miley, Y. Gu, and T. Hochberg, *Fusion Technol.* **21**, 1639 (1992).
- ²G. H. Miley, J. Javendani, Y. Yamamoto, R. Nebel, J. Nadler, Y. Gu, A. Satsangi, and P. Heck, *Third International Conference on Dense Z-Pinches*, eds. M. Haines and A. Knight, *AIP Conference Proceedings* 299, AIP Press, 675 (1994).
- ³G. H. Miley, J. Nadler, T. Hochberg, Y. Gu, O. Barnouin, J. Lovberg, *Fusion Technol.* **19**, 840 (1991).
- ⁴J. H. Nadler, G. H. Miley, Y. Gu, and T. Hochberg, *Fusion Technol.* **20**, 850 (1991).
- ⁵R. Hirsch, *J. Appl. Phys.* **38**, 4522 (1967).
- ⁶Gardner, A. L., D. M. Hatch, A. I. Y. Chan, and R. P. Evans, *Ann. NY Acad. Sci.* **251**, 179 (1975).
- ⁷K. Miyamoto, *Plasma Physics for Nuclear Fusion* (M.I.T. Press, Cambridge, 1987), p. 507.
- ⁸K.L.Wilson, in Data Compendium for Plasma Surface Interactions, (IAEA publications, 1984), p. 28.
- ⁹R. K. Janev, W. D. Langer, K. Evans, Jr., and D. E. Post, Jr., *Elementary processes in Hydrogen - Helium Plasmas*. (Springer-Verlag, Berlin, 1987).
- ¹⁰*NRL Plasma Formulary* , edited by J. D. Huba (rev. 1994), p. 31.
- ¹¹*Handbook of Chemistry and Physics* , 71st ed., edited by D. R. Lide, (CRC Press, Boston, 1990), p. 10-282.

Chapter 7: Summary

The Spherically Convergent Ion Focus (SCIF) has been proposed as an alternate concept of confining ions of thermonuclear interest, and past experiments and theoretical models of these systems produced a variety of different and conflicting results. Therefore, a reasonably complete physical model of their behavior had not been developed, and hence the viability of the SCIF concept for near-term applications has been difficult to determine.

The WISCIF experiments were conducted to resolve ambiguities of the past experiments by providing direct measurements of the critical system parameters needed to understand the physical processes that determine the fusion reactivity of these devices. Here we summarize our results and conclusions.

7.1 ION FLOW CHARACTERIZATION

The first detailed evaluation of the ion flow characteristics in the low-pressure, converged-core regime of a SCIF was performed in the WISCIF device. Measurements of the electrostatic potential distribution throughout the system show agreement with a recirculating space-charge-limited ion flow model and indicate the ions dominate the system at these low pressures (< 53 mPa). A virtual anode structure formed in the converged core, due to the enhanced ion density in that region, but no evidence of multiple potential well structures is seen for the conditions studied. Camera imaging and plasma potential measurements in the core region show that flow convergence improves with increasing

voltage, pressure, potential well symmetry, and decreasing current. The tightest observed core sizes ($r_c = 0.6$ cm) are within a factor of 4-5 of the ideal geometric limit given by Eq. (2.2) and are consistent with a collisionless multi-pass orbit model prediction given the degree of asymmetries measured in the accelerating potential well. Core density measurements show a factor of ~10 increase in ion density in the core region (compared to the edge), which agrees with a simple flow conservation model.

7.2 FUSION PRODUCTION RATE MEASUREMENTS

In order to resolve the conflicting models and expectations for SCIF devices, characterization of the various sources of reactivity and the influence of cathode power, ion-neutral collisions, and cathode design were investigated. The neutron production rate (*NPR*) scales linearly with current, with the D-D fusion cross section with voltage, and as expected with pressure considering the effects of charge-exchange on the fusible ion flow distribution. Proton collimation experiments verified that most of the fusion production originates well outside the central core region. The *NPR* did not depend strongly on the cathode material, wire spacing, or transparency, and the cathode grid itself may contribute 10% of the measured *NPR* at high pressure (~ 250 mPa) and potentially up to 60% at lower pressures (~ 50 mPa).

These results are completely inconsistent with the expectations from the multiple-well model. Although the measured *NPR*'s exceed the collisionless estimate at low pressure, the reactivity can be accounted for if the beam-cathode and fast-neutral-background contributions are considered. It appears that no anomalous trapping of ions is required to explain the observed *NPR* scalings for these systems.

7.3 COMMENTS AND FUTURE DIRECTIONS

A variety of other physics issues can be addressed in further studies of these devices. Many require, however, much higher density operation than has been conducted to date. For example, it has been predicted that ion-ion collisions will thermalize the flow and lead to a collapse of the convergence on time scales that will be prohibitive to achieve a $Q \sim 1$ power balance^{1,2}. These effects cannot be studied in present systems, as ion-neutral or ion-grid collisions dominate over the ion-ion collisions (See Table 6-1). Future virtual cathode systems like the Penning trap or the Polywell™ may be able to confine ions long enough so that ion-ion collisional effects can manifest themselves.

In addition, the stability of the ion flow is a question at higher injected currents due to the onset of a possible two-stream instability. Using a slab model as a first approximation, the instability criterion is³:

$$\frac{k_r v}{\omega_{pi}} > 1 \quad (7.1)$$

where v is the velocity of the ions, k_r is the wave number of a given oscillation, and ω_{pi} is the ion plasma frequency. Assuming wavelengths on the order of the diameter of the cathode ($k_r \sim \pi/2r_{cat}$), the necessary condition for studying the instability would then be that $n_i > 1.7 \times 10^{15} \text{ m}^{-3}$ on average inside a 10.0 cm diameter cathode for 5 keV ions. For comparison, this will require currents $> 300 \text{ mA}$ in the WISCIF device (assuming a linear scaling of density with current from the density measurements from Table 5-2).

Higher currents will also be needed to study more power-efficient regimes where beam-beam fusion reactions dominate the system reactivity ($R_{fus} \sim I^2$). If the neutral density is lowered to 1.3 mPa, the required average ion density inside the cathode to equal the neutral density is $3.3 \times 10^{17} \text{ m}^{-3}$. The WISCIF device (assuming again a 10.0 cm diameter cathode)

would require > 50 A of injected current to provide this ion density. An improved edge plasma source would also be required to supply the needed ion current from the edge.

These effects may be studied transiently in a small-scale device using a pulsed, high-current power supply. This also reduces the power handing requirements on a cathode grid (if used). Smaller systems can also further test the understanding of the system reactivity by using alternative fusion reactions. Experiments with ^3He or other advanced fuels may then investigate the viability of the concept as sources of fast alphas, protons, or other fusion products.

Some engineering issues have also been identified through the course of these experiments. The cathode power and stress loading requirements are the likely limiting factors for the eventual reactivity produced by a system design, for cathode powers of 6 kW is more than adequate to destroy some of the highly transparent cathodes (~ 2 MW/m 2 typically melted the stainless steel grids). Secondly, the cathode support design must withstand a very energetic and dense plasma environment for the more application relevant regimes, and the lifetime of this support is limited by the amount of cathode material that is sputtered onto it. High steady-state injected powers will also generate a significant temperature rise in the vacuum vessel, and higher reactivity systems may require special designs or cooling capabilities to dissipate this heat.

7.4 CONCLUSIONS

The objectives of this thesis work were satisfied as:

- (1) The WISCIF experimental facility was constructed, and it is capable of producing ion flows for pressures as low as 13 mPa in hydrogen, which is essentially collisionless with respect to neutrals. The present reactivity experiments have also studied higher

power (up to 6 kW) and higher density (up to 250 mA injected current) than previously studied at fusion relevant energies (> 20 keV).

- (2) The first direct measurements of the electrostatic potential, flow convergence, and core ion density were performed for the converged core discharges using high-voltage electrostatic probes and CCD camera imaging. The flow convergence is consistent with orbit calculations given the degree of asymmetries observed in the potential well. The core ion density also agrees with simple current conservation estimates, and the radial electrostatic potential distribution in the mantle region is consistent with a space-charge-limited flow model.
- (3) The fusion production rate was characterized with neutron count rate measurements, and a collimated proton detector measured the spatial distribution of the fusion production. The collimation measurements indicate that most of the fusion reactions are generated outside the cathode radius, and the measured neutron production rate agrees with a flow model estimate that includes the effects of charge-exchange on the ion flow.

These experiments found that the WISCIF device behaves rather classically in all operating regimes studied. Given these conclusions, gridded systems will not make adequate power amplifiers, due to the cathode power and stress handling requirements. Depending on need, such devices may hold promise for near-term particle source applications, but the optimization of such sources should be undertaken in the context of the physical model developed here.

7.5 REFERENCES

¹W. M. Nevins, Phys. Plasmas **2**, 3804 (1995).

²T. H. Rider, Phys. Plasmas **2**, 1853 (1995).

³T. H. Stix, *Waves in Plasmas*, (A.I.P., New York, 1992).

Appendix 1: Core reaction rate calculations for beam-beam interactions

Some investigators have suggested that a SCIF device may have enhanced reactivity due to a “monoenergetic” distribution function^{1,2}. This may be true in the accelerating and mantle regions of the device, where counter-flowing beam distributions are evident; the relative velocity between the two halves of the distribution functions is $2v_i$ (See. Fig. 2-2). However, the spherical shell distribution in the core region gives a spread in relative velocities in a very similar manner as a thermal Maxwellian.

The velocity distribution averaged fusion reaction rate is given by:

$$\langle \sigma v \rangle = \int d^3v_1 \int d^3v_2 f_1(v_1) f_2(v_2) |v_1 - v_2| \sigma(|v_1 - v_2|) \quad (\text{A1.1})$$

where f_1 and f_2 are the “beam” and “target” ion distribution functions in the core region, and σ is the relative-velocity dependent fusion cross section. The two distributions are spherical shells in velocity space, or:

$$f_i(v_i) = \frac{\delta(v_i - v_c)}{4\pi v_c^2} \quad (\text{A1.2})$$

and substituting this distribution into Eq. (A1.1) gives:

$$\langle \sigma v \rangle = \int d^3v_2 f_2(v_2) |v_2 - v_c \hat{r}| \sigma(|v_2 - v_c \hat{r}|) \quad (\text{A1.3})$$

$$\langle \sigma v \rangle = \int_0^{2\pi} dv_\phi \int_0^\pi \sin \theta dv_\theta \int_0^\pi v_r^2 dv_r \frac{\delta(v_c \hat{r})}{4\pi v_c^2} |v_2 - v_c \hat{r}| \sigma(|v_2 - v_c \hat{r}|) \quad (\text{A1.4})$$

By investigating the geometry, a scalar relationship can be found for the relative speed $|v| = |v_2 - v_c \hat{r}|$ (See Fig. A1-1). The two right triangles (A and B) share a common side, and therefore from the Pythagorean theorem:

$$|v|^2 - v_c^2(1 - \cos \theta)^2 = v_c^2 - v_c^2 \cos^2 \theta \quad (\text{A1.5})$$

which when solved for the relative speed, $|v|$ gives

$$|v| = \sqrt{2v_c^2(1 - \cos \theta)} \quad (\text{A1.6})$$

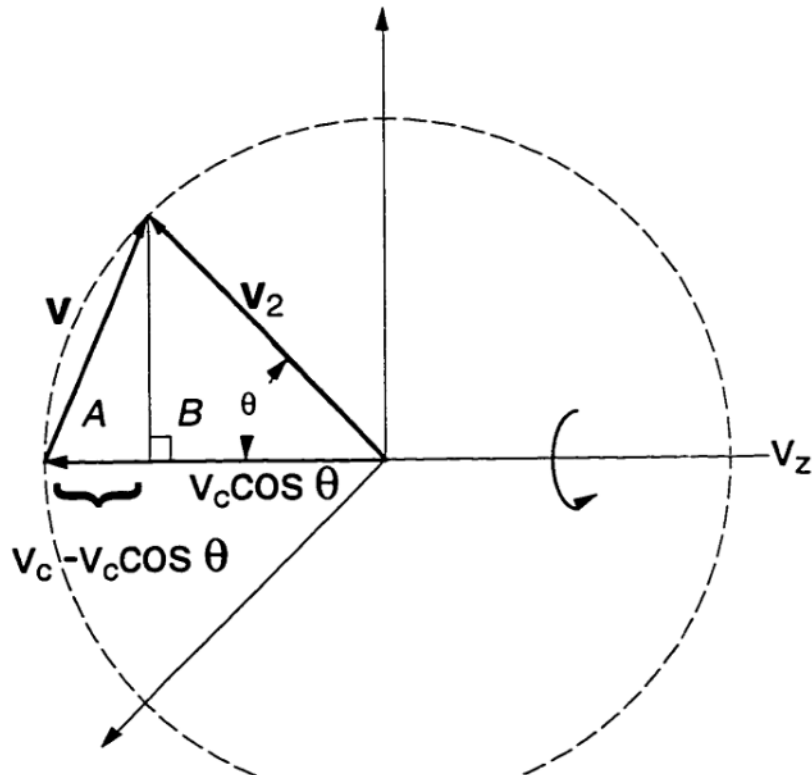


Figure A1-1. Geometry for the core reaction rate calculation

Substituting Eq. (A1.6) into the integral in Eq. (A1.4) then gives:

$$\langle \sigma v \rangle = \frac{1}{2} \int_0^{\pi} \sin \theta d\theta \sqrt{2v_{\text{c}}^2 (1 - \cos \theta)} \sigma(\sqrt{2v_{\text{c}}^2 (1 - \cos \theta)}) \quad (\text{A1.7})$$

Using an empirical fit for the fusion cross section function³, Eq. (A1.7) was evaluated numerically, and the results for D-D and D-T are compared with tabulated Maxwellian data in Fig. 2-4⁴. For ion flow energies above 30 keV, the reaction rates are practically equal ($\approx 10^{-21} \text{ m}^3/\text{s}$) for D-T between the spherical shell distribution and a Maxwellian of the same temperature. In the D-D case, the Maxwellian reaction rate is consistently greater than the spherical shell distribution. Therefore, the $\langle \sigma v \rangle$ for a spherical shell distribution can be well approximated by the more well-known Maxwellian reaction rates for most fusion-relevant applications ($E > 30 \text{ keV}$).

REFERENCES

- ¹G. H. Miley, J. B. Javedani, Y. B. Gu, A. J. Satsangi, P. F. Heck, I. D. Tzonev, M. J. Williams, S. G. DelMedico, R. A. Nebel, D. C. Barnes, L. Turner, J. H. Nadler, and J. Sved, Fusion Studies Laboratory Report # FSL-483 (1994).
- ²R. W. Bussard, *J. Propulsion and Power* **6**, 567 (1990).
- ³A. Anders, *A Formulary for Plasma Physics*, (Akademie-Verlag, Berlin, 1990).
- ⁴R. R. McNally Jr., K. E. Rothe, R. D. Sharp, Oak Ridge National Laboratory, Report #ORNL/TM-6914 (1979).

Appendix 2: Probe theory for ion-dominated flow

Measurements of the floating and plasma potentials (V_f and V_p) of the emissive probe show that $V_f > V_p$ for the core, plateau, and mantle regions (See Fig. 5-3). The amount of electron current drawn to the probe is then saturated and constant, and the probe biases itself positive to collect only enough ion current to equal this electron current at the floating potential ($I_i = I_e$ at V_f).

This is also the case for the floating double probe system, where the following relation must hold¹:

$$i_{1+} + i_{1-} = i_{2+} + i_{2-} \quad (\text{A2.1})$$

where “1” and “2” signify the first and second probe tip and “+” and “-” refer to ion and electron current. The current measured in the circuit is the difference between the ion and electron current in a particular probe tip¹:

$$I = i_{1+} - i_{1-} = i_{2+} - i_{2-} \quad (\text{A2.2})$$

The electron current collected by each of the double probe tips is the local electron saturation current ($i_{e,sat}$), and hence $i_{1-} = i_{2-} = i_{e,sat}$ if the area of each probe tip is equal (as is the case for the experiment). By applying a bias across the probe tips, one tip will collect more ion current, and because the probe as a whole remains floating [Eq. (A2.1)], the other probe tip must collect less the same amount of ion current. By sweeping the bias across the probe tips, the ion distribution can be sampled until one of the probe tips collects zero ion current (e.g. $i_{2+} = 0$). A knee is then seen in the I-V characteristic, and by Eq. (A2.2), the current measured in the circuit is equal to the electron saturation current.

In the core region, V_f and V_p are approximately equal, and for a lowest order estimate for the core ion density (n_{ic}), the ion saturation current ($i_{i,sat} = en_{ic}v_c A_p$, where v_c is the core ion velocity and A_p is the probe area) is assumed to be approximately equal to $i_{e,sat}$. This is

equivalent to assuming that $n_i \approx n_e$ if the ion flow velocity is given by the core potential, and the electron thermal velocity is on the order of a few eV.

REFERENCES

- ¹N. Hershkowitz, in *Plasma Diagnostics*, edited by O. Auciello and D. L. Flamm (Academic Press, Boston, 1989), p. 176.